Supporting Information for

Air-stable Four-Coordinate Cobalt(II) Single-Ion Magnets: Ab-Initio Ligand Field Analysis of Correlations Between Dihedral Angles and Magnetic Anisotropy

Sandeep K. Gupta,[a] Shashank V. Rao,[b] Serhiy Demeshko,[a] Sebastian Dechert,[a] Eckhard Bill,[c] Mihail Atanasov,*[b,d] Frank Neese,*[b] Franc Meyer*[a]

[a] Institut für Anorganische Chemie, Universität Göttingen, Tammannstrasse 4, 37077 Göttingen (Germany)

[b] Max-Planck-Institut für Kohlenforschung, Kaiser-Wilhelm-Platz 1, 45470 Mülheim an der Ruhr (Germany)

[c] Max Planck Institute for Chemical Energy Conversion, Stiftstrasse 34-36, 45470 Mülheim-an-der-Ruhr (Germany)

[d] Institute of General and Inorganic Chemistry, Bulgarian Academy of Sciences, Akad. Georgi Bontchev Street 11, 1113 Sofia (Bulgaria)
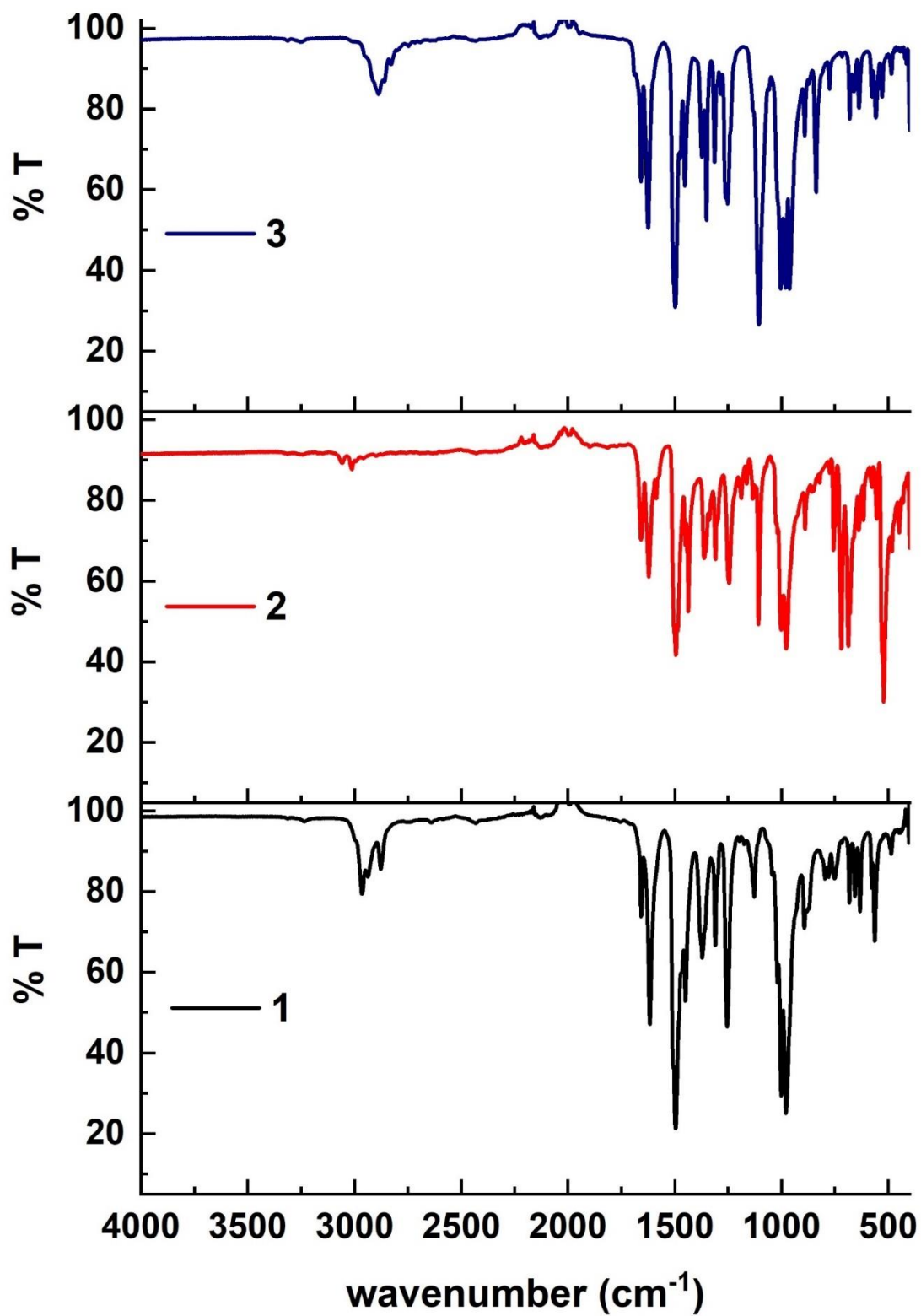
Contents

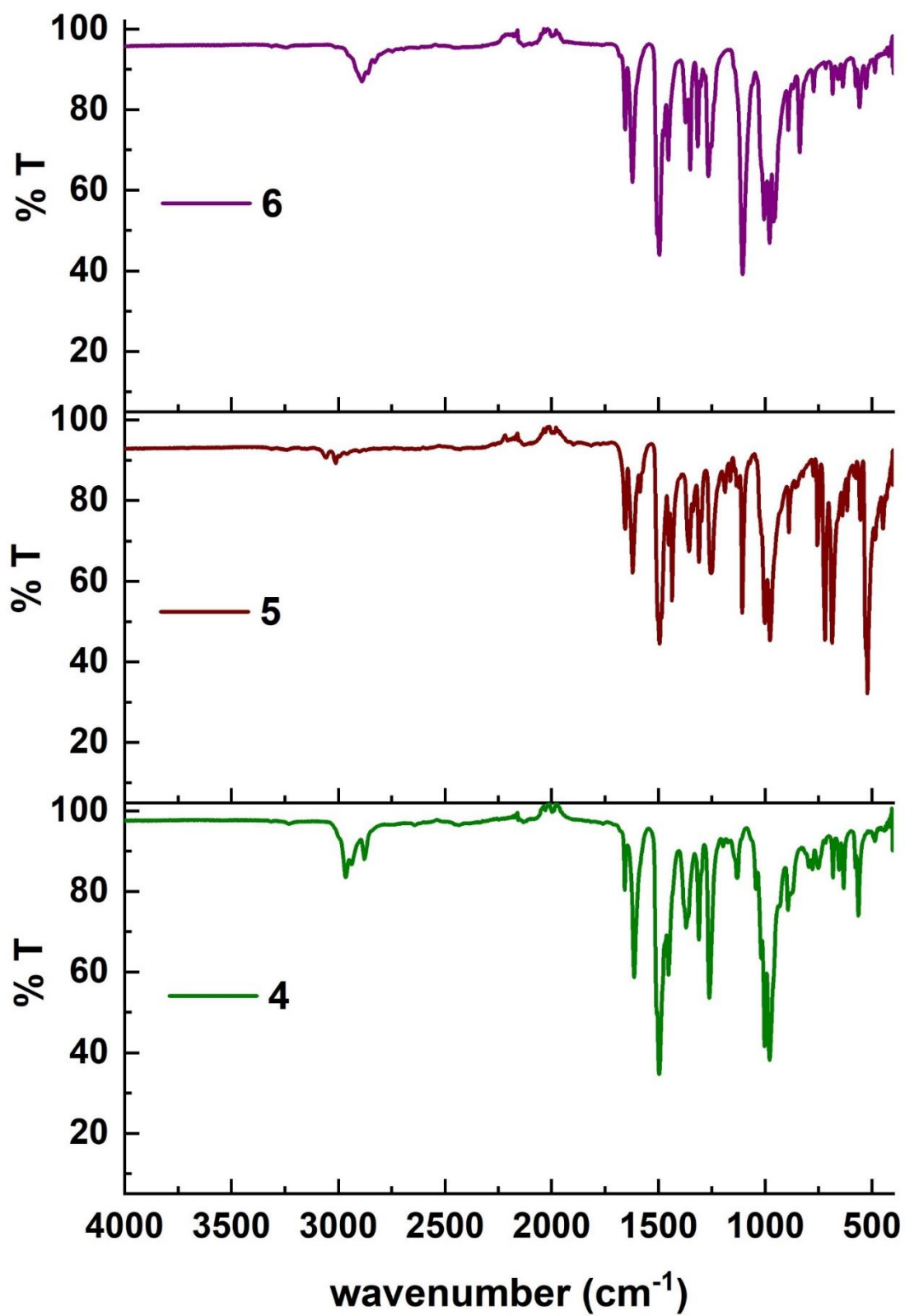# 1. Spectroscopic and Mass Spectrometric Characterization
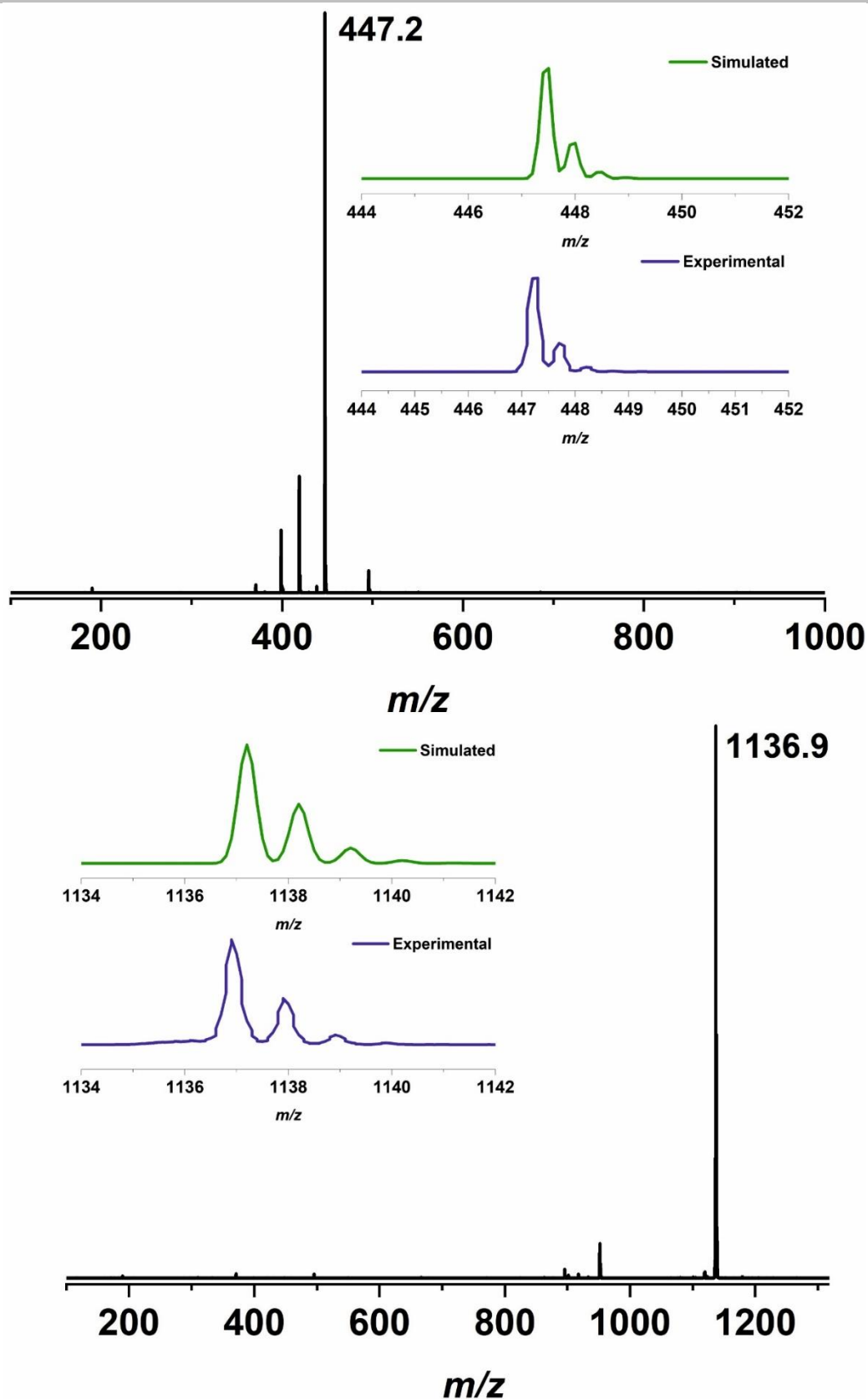

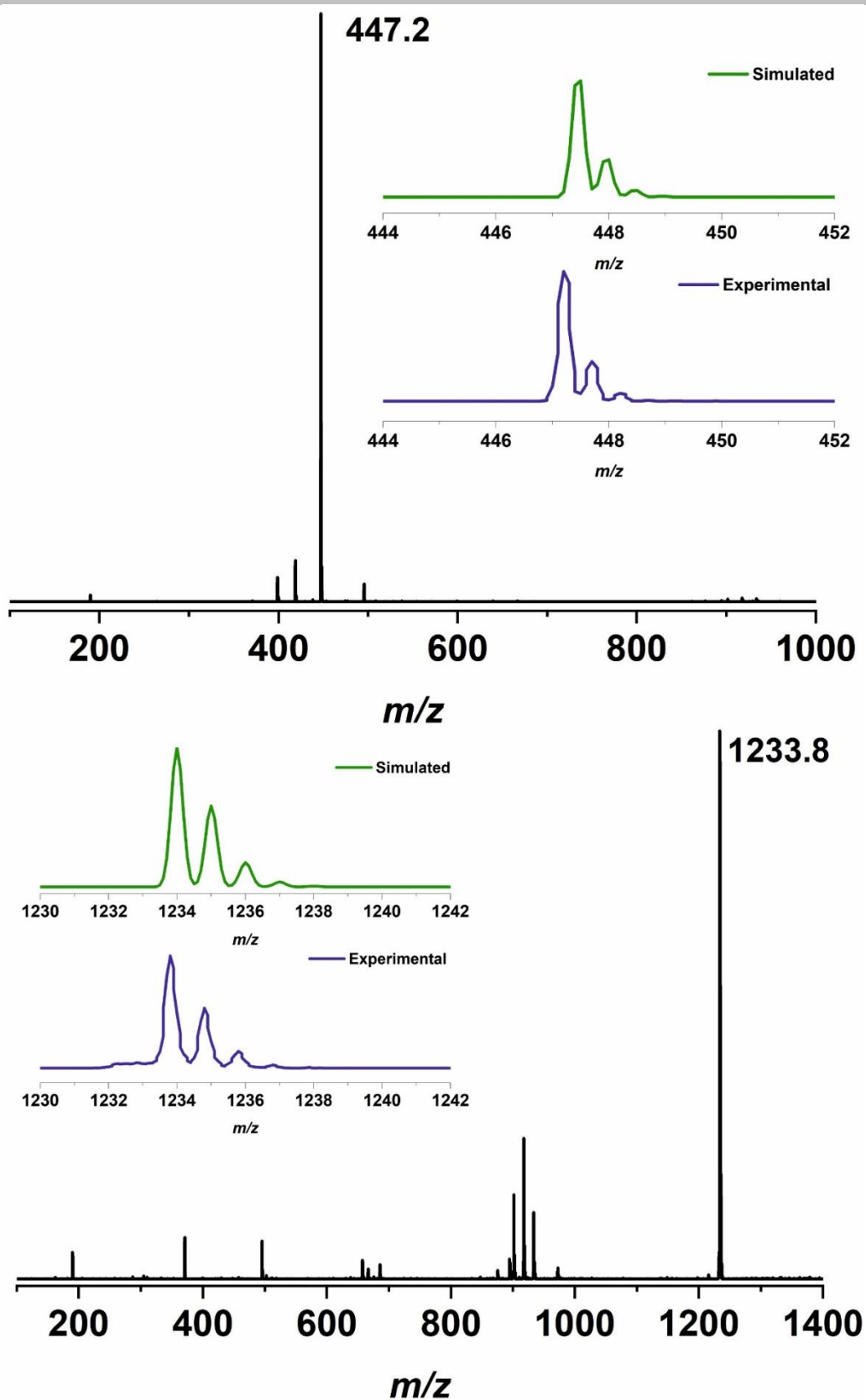**Figure S1.** FT-IR spectra of complexes **1**-**3**.

Figure S2. FT-IR spectra of complexes **4**-**6**.

Figure S3. Negative ion ESI-MS of complex **1** recorded in acetonitrile with the spectrometer tuned to the respective m/z range for the expected ions. The inset shows the experimental and simulated isotopic distribution pattern for the ion $[^{F}L_2Co]^{2-}$ (top) and $[^{F}L_2Co(TBA)]^{1-}$ (bottom).

Figure S4. Negative ion ESI-MS of complex **2** recorded in acetonitrile with the spectrometer tuned to the respective *m/z* range for the expected ions. The inset shows the experimental and simulated isotopic distribution pattern for the ion $[^FL_2Co]^{2-}$ (top) and $[^FL_2Co(PPh_4)]^{1-}$ (bottom).
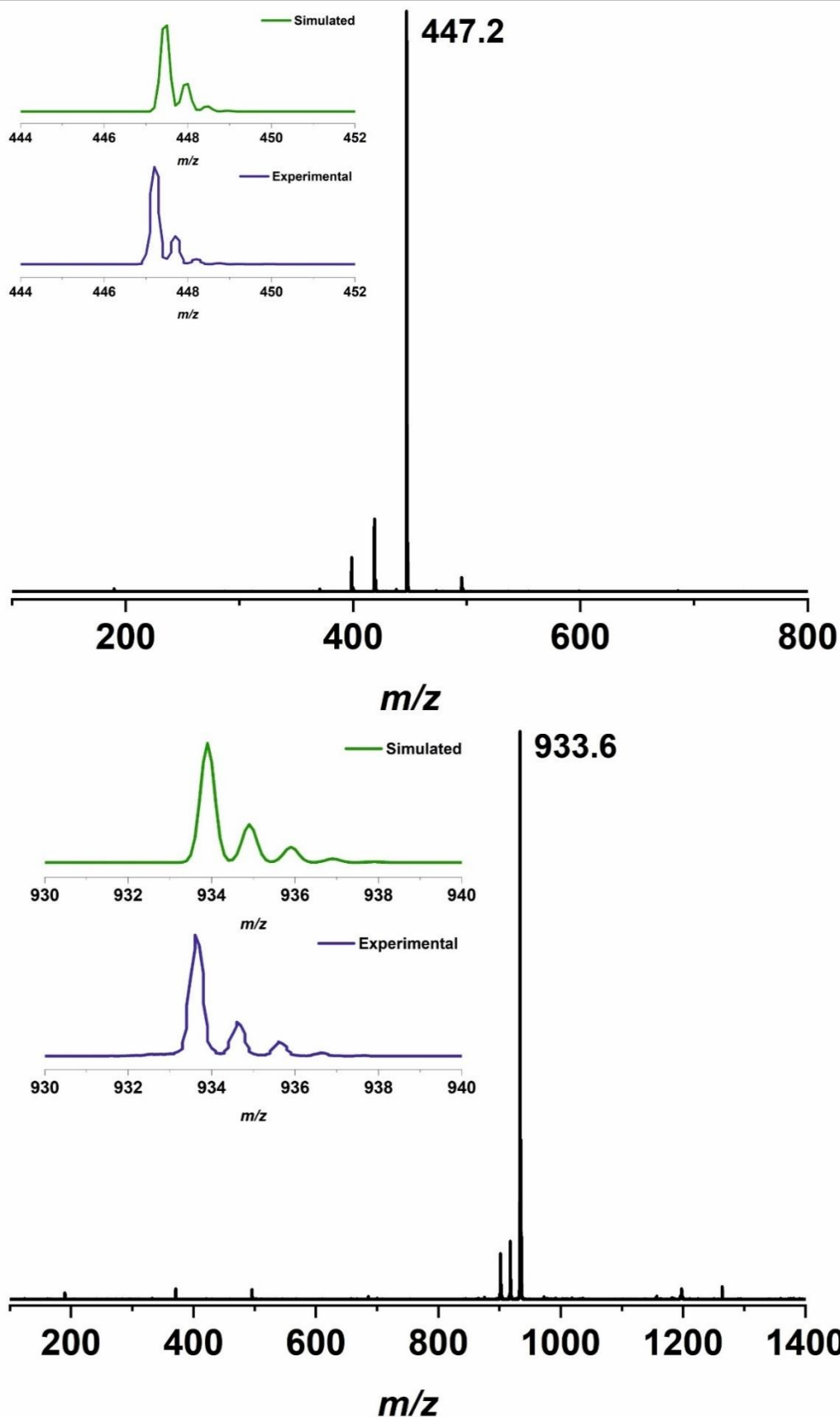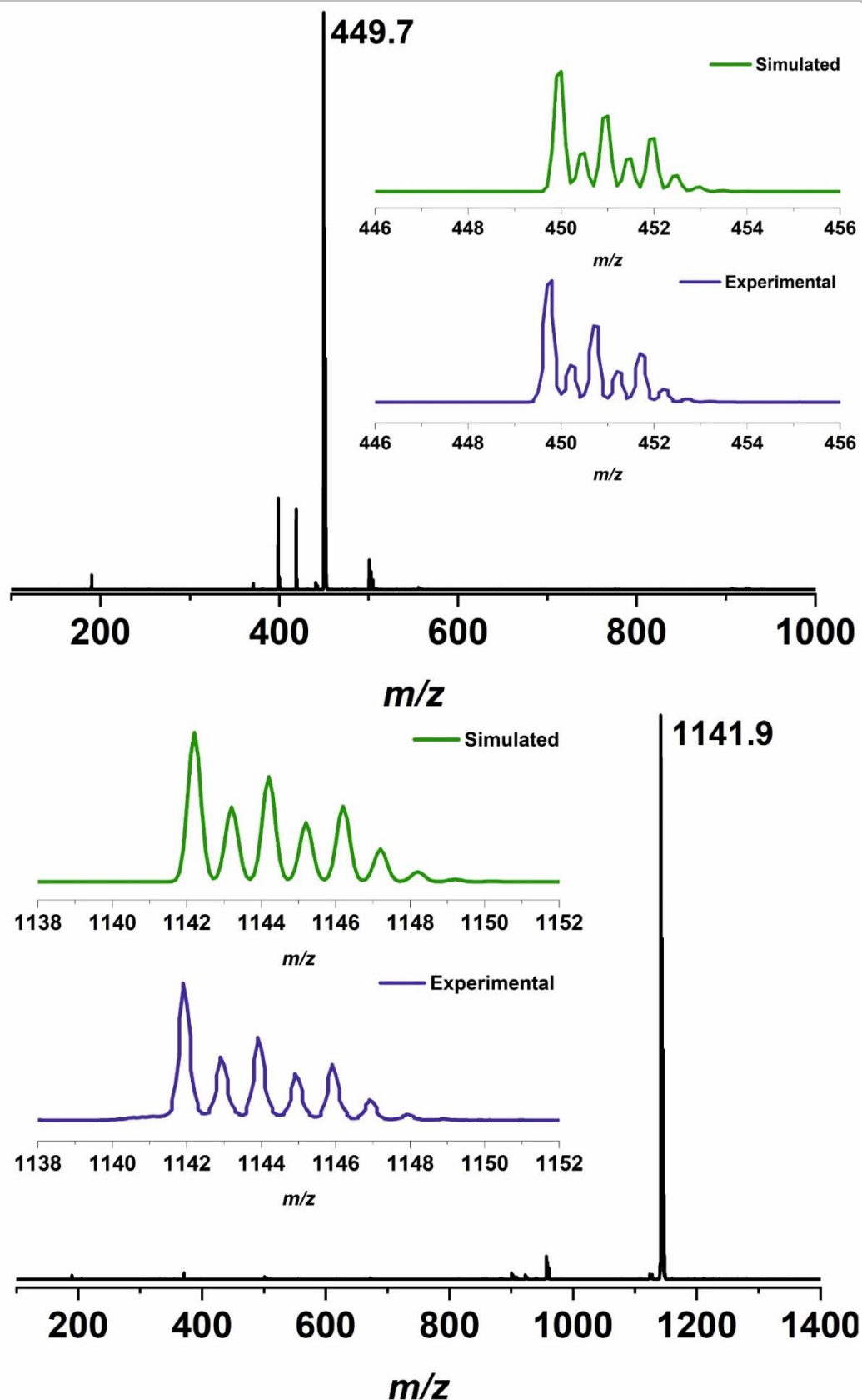
Figure S5. Negative ion ESI-MS of complex **3** recorded in acetonitrile with the spectrometer tuned to the respective *m/z* range for the expected ions. The inset shows the experimental and simulated isotopic distribution pattern for the ion [^{F}L$_2$Co]$^{2-}$ (top) and [^{F}L$_2$Co(K@18C6)]$^-$ (bottom).

.

Figure S6. Negative ion ESI-MS of complex **4** recorded in acetonitrile with the spectrometer tuned to the respective m/z range for the expected ions. The inset shows the experimental and simulated isotopic distribution pattern for the ion $[^{F}L_2Zn]^{2-}$ (top) and $[^{F}L_2Zn(TBA)]^{1-}$ (bottom).

Figure S7. ^{1}H NMR spectrum of complex **4** (CD$_3$CN, 400 MHz, 295 K).

Figure S8. ^{13}C NMR spectrum of complex **4** (CD$_3$CN, 101 MHz, 295 K).

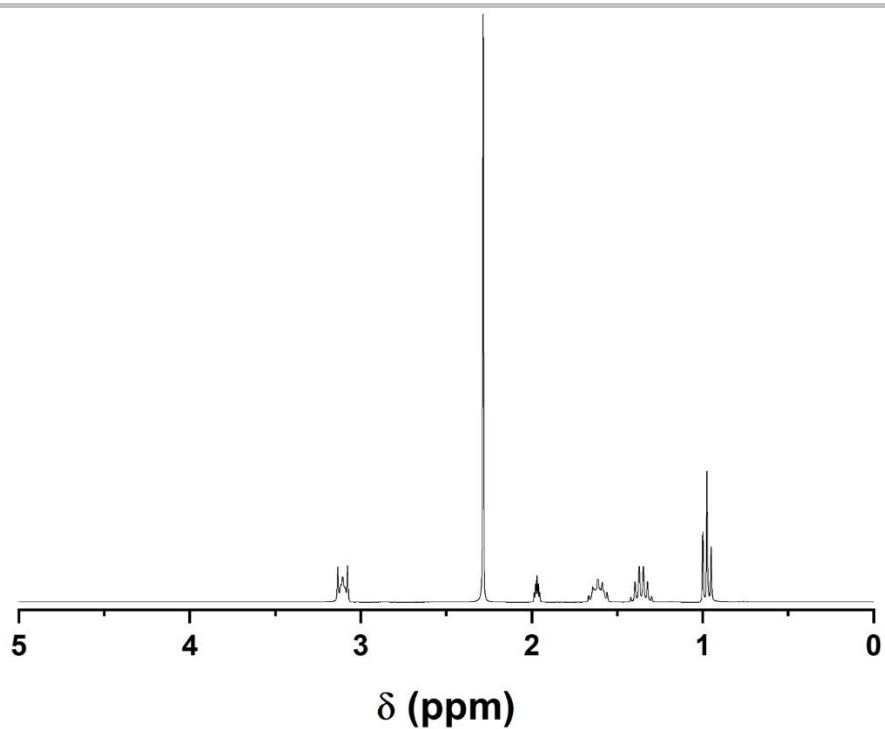**Figure S9.** ^{19}F NMR spectrum of complex **4** (CD$_3$CN, 377 MHz, 295 K).
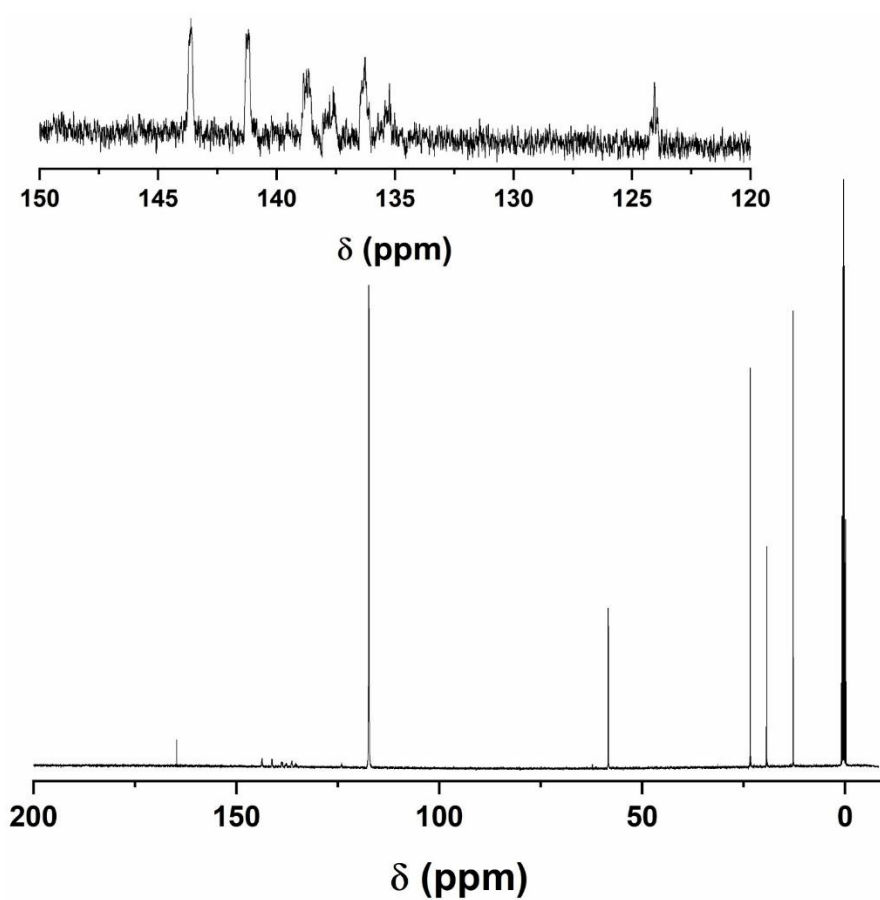
Figure S10. Negative ion ESI-MS of complex **5** recorded in acetonitrile with the spectrometer tuned to the respective *m/z* range for the expected ions. The inset shows the experimental and simulated isotopic distribution pattern for the ion [^FL_2Zn]$^{2-}$ (top) and [$^FL_2Zn(PPh_4)$]$^{1-}$ (bottom).
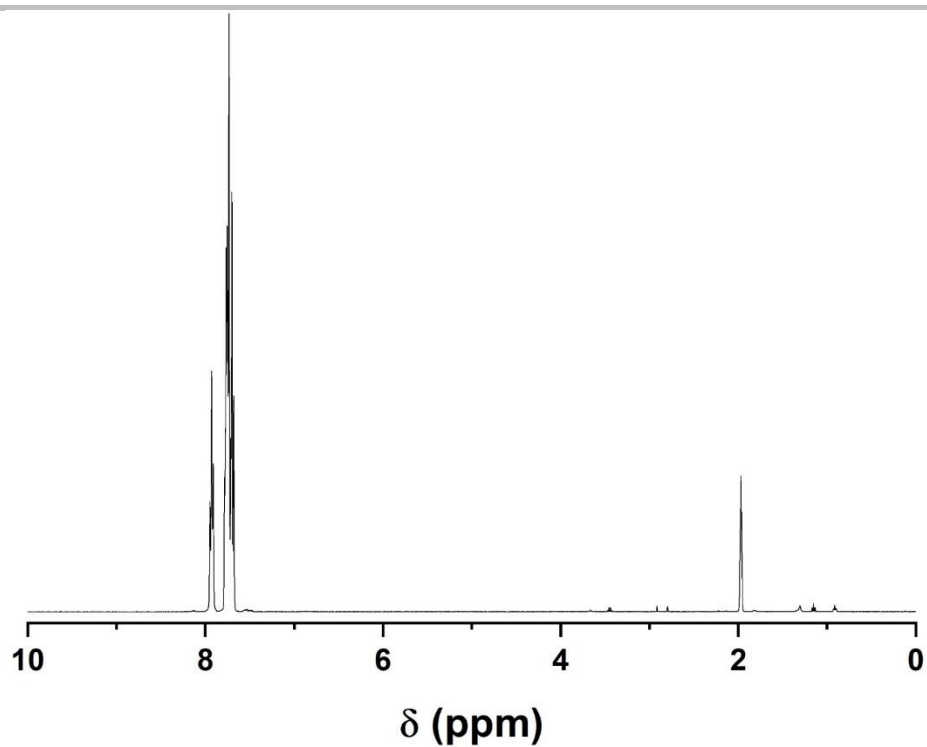
Figure S11. ^{1}H NMR spectrum of complex **5** (CD$_3$CN, 400 MHz, 295 K).
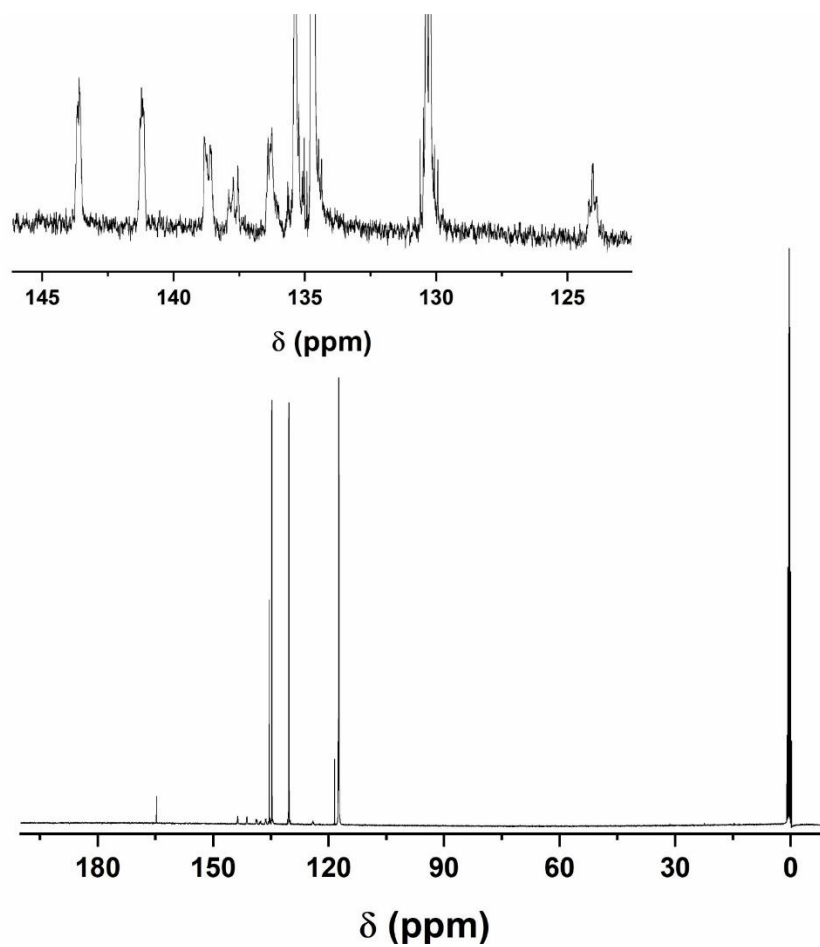
Figure S12. ^{13}C NMR spectrum of complex **5** (CD$_3$CN, 101 MHz, 295 K).
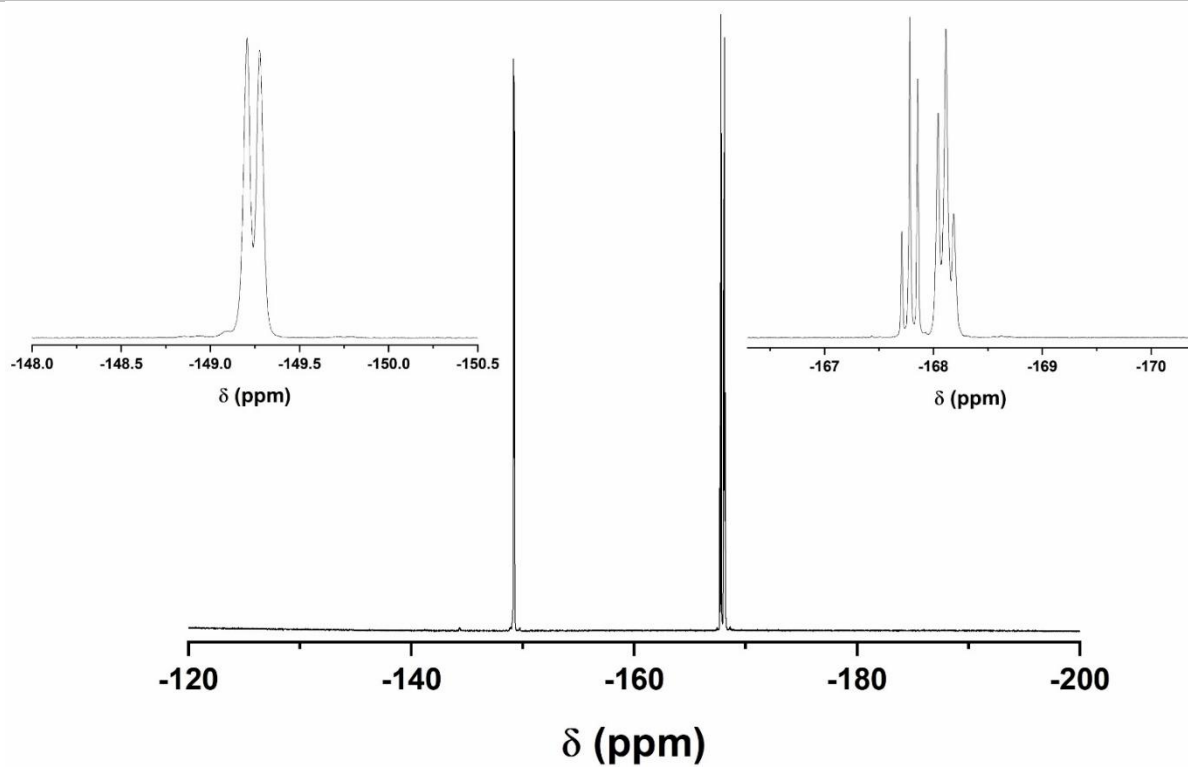
Figure S13. ^{19}F NMR spectrum of complex **5** (CD$_3$CN, 282 MHz, 295 K).
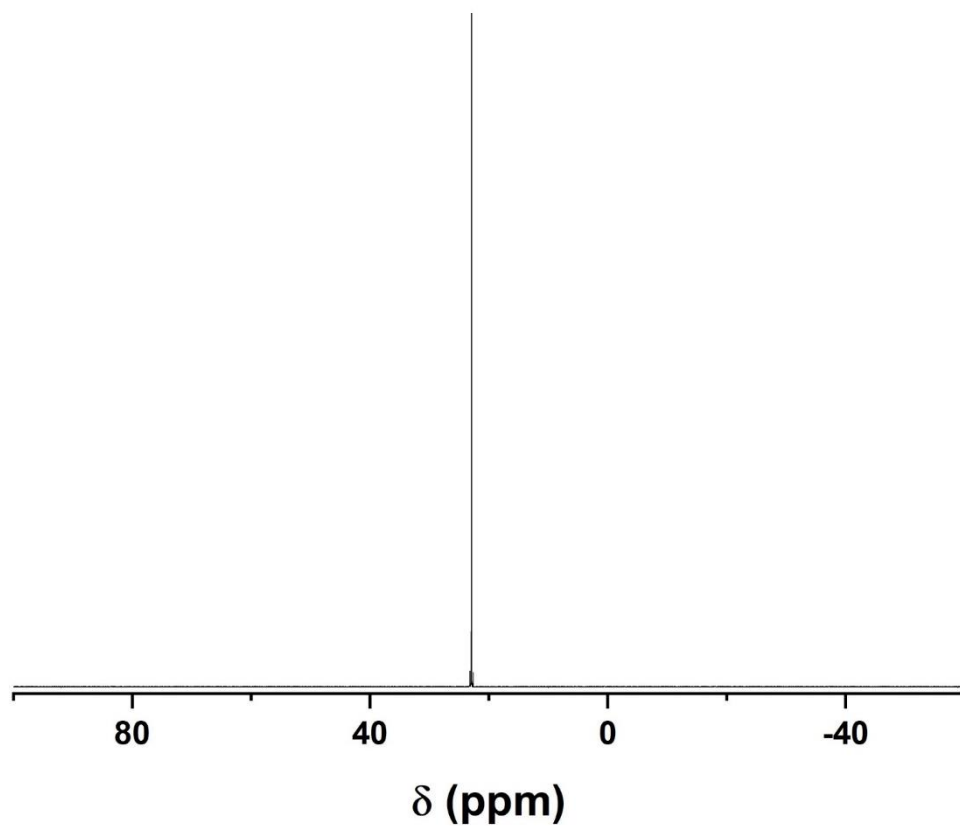
Figure S14. ^{31}P NMR spectrum of complex **5** (CD$_3$CN, 162 MHz, 295 K).

S13
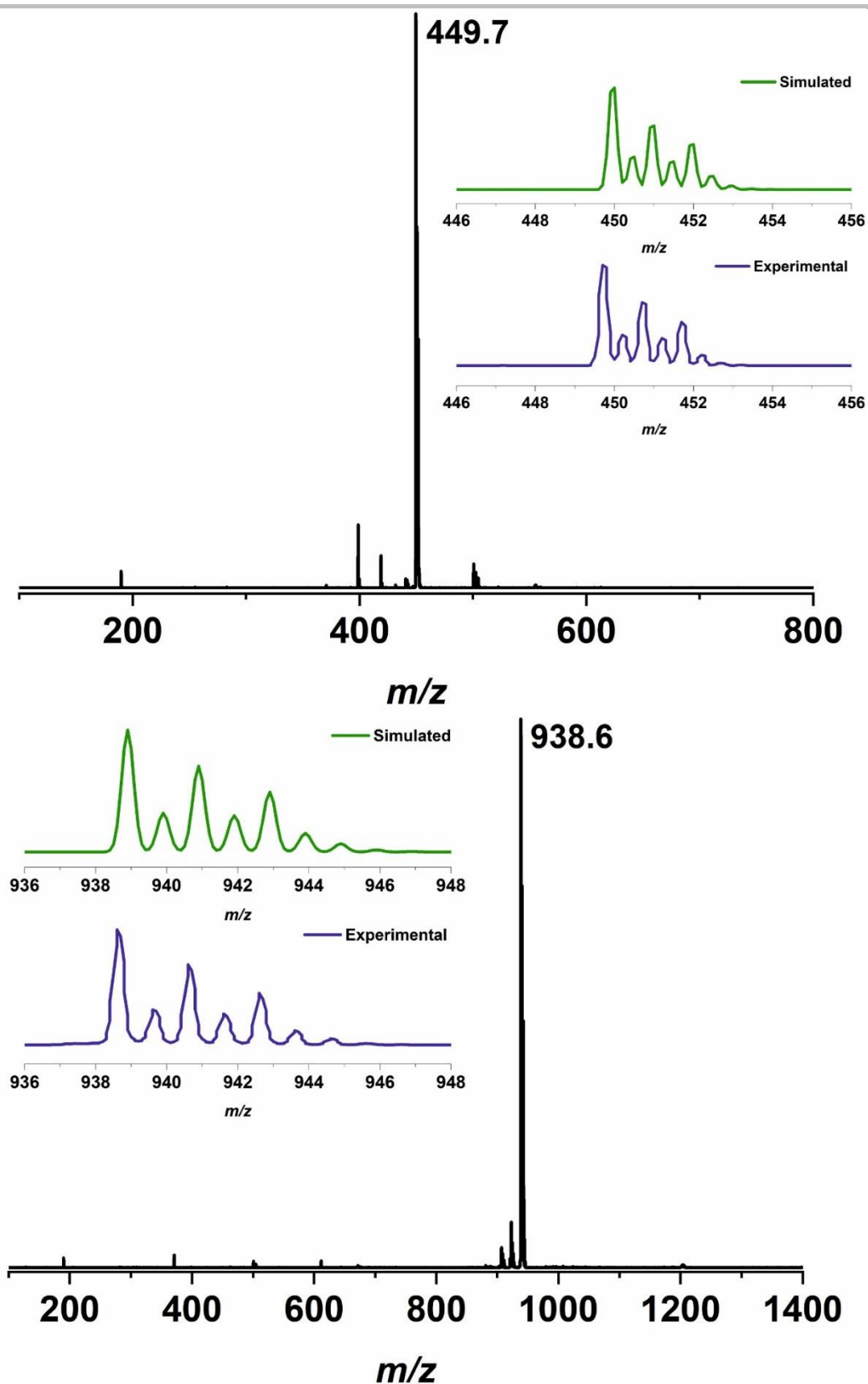
Figure S15. Negative ion ESI-MS of complex **6** recorded in acetonitrile with the spectrometer tuned to the respective m/z range for the expected ions. The inset shows the experimental and simulated isotopic distribution pattern for the ion $[^FL_2Zn]^{2-}$ (top) and $[^FL_2Zn(K@18C6)]^-$ (bottom).
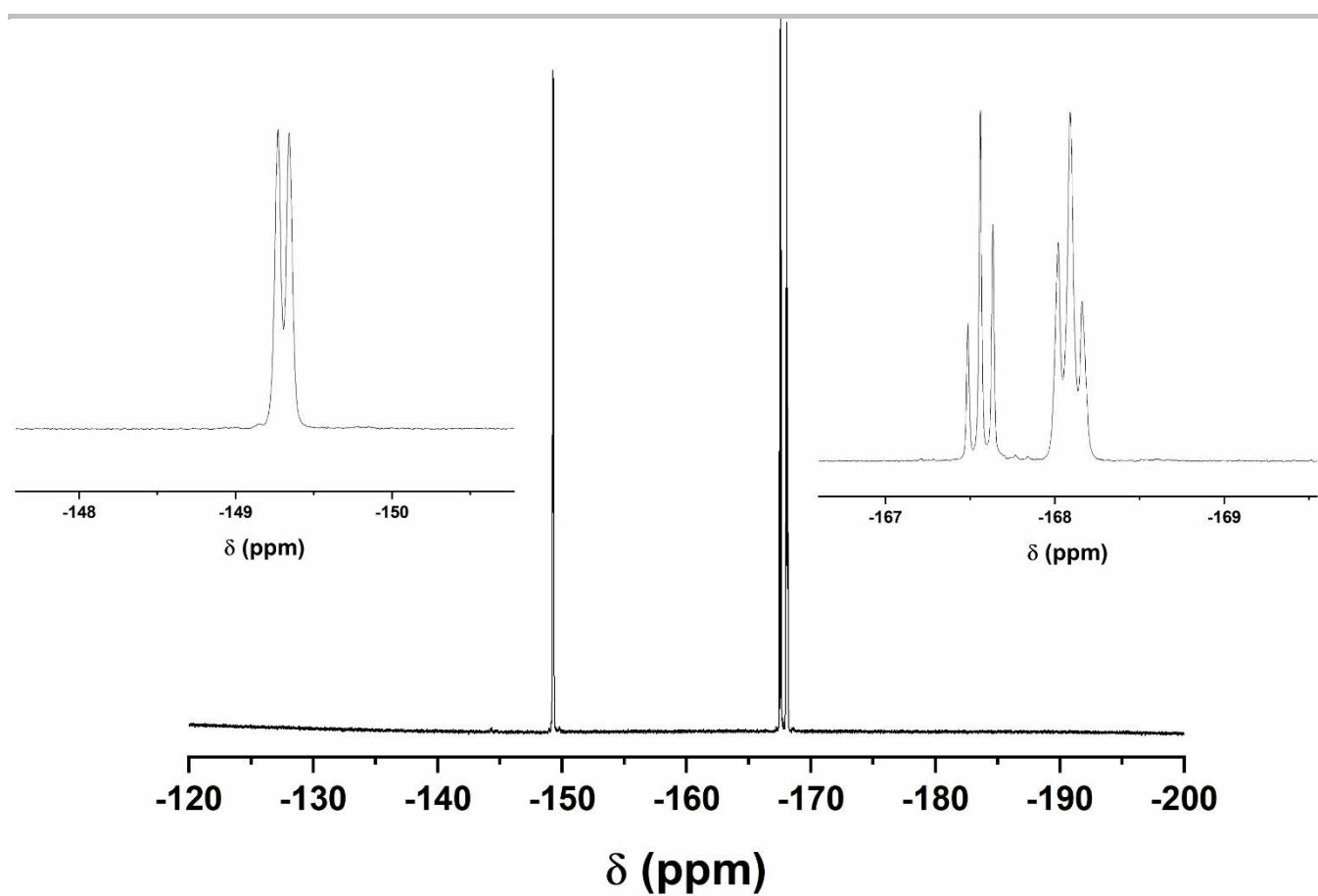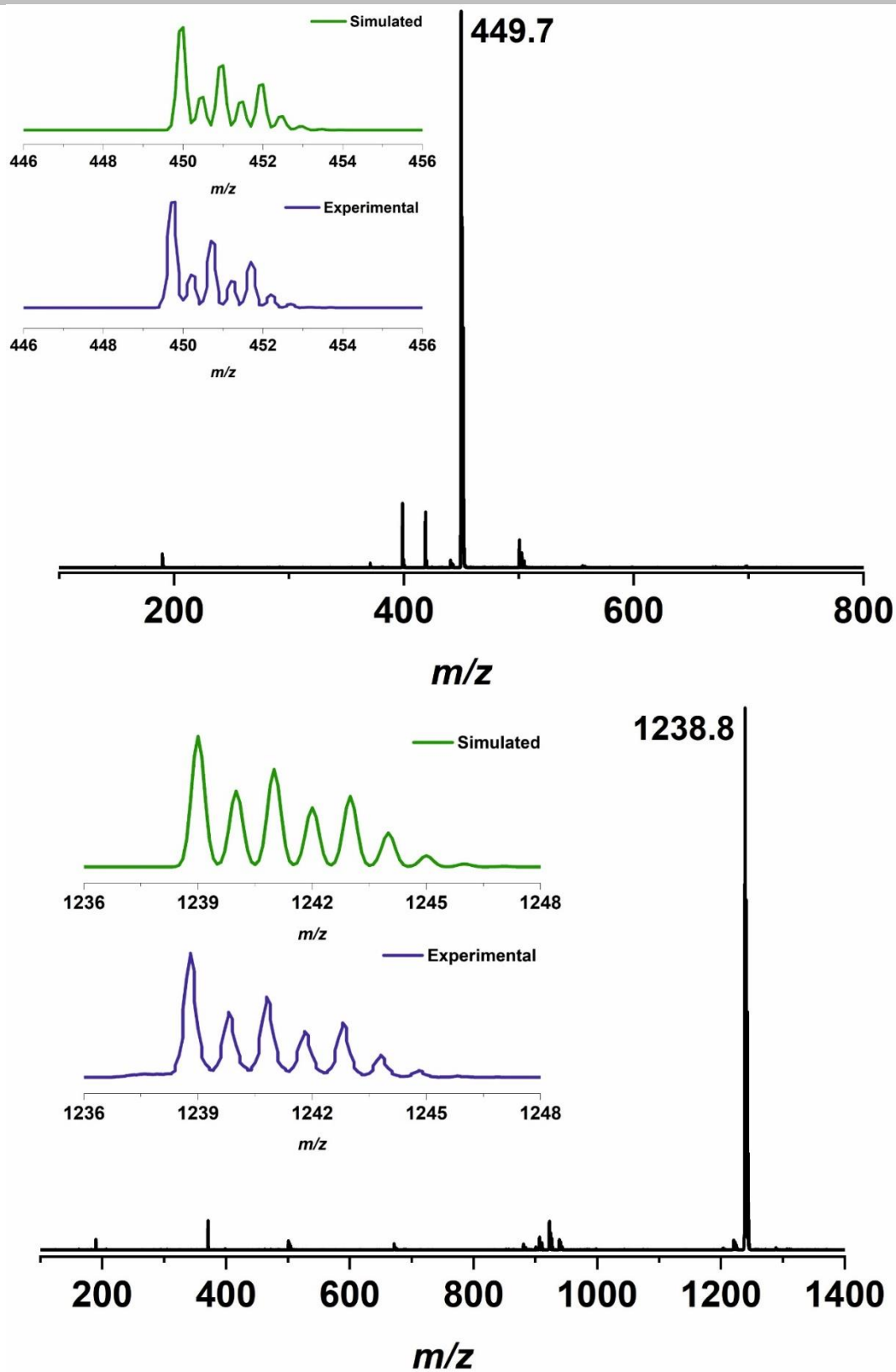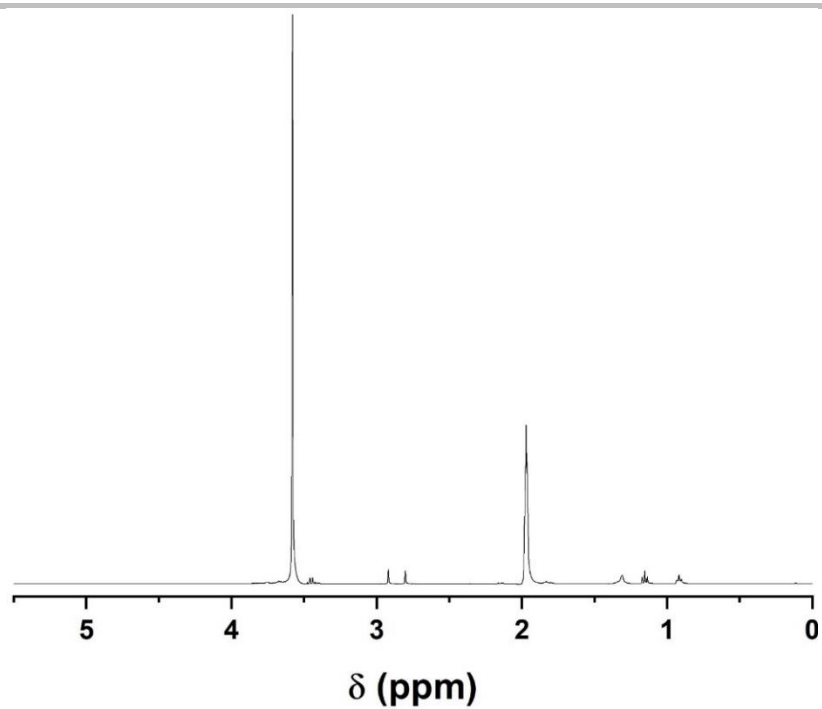
Figure S16. ^{1}H NMR spectrum of complex **6** (CD$_3$CN, 400 MHz, 295 K).
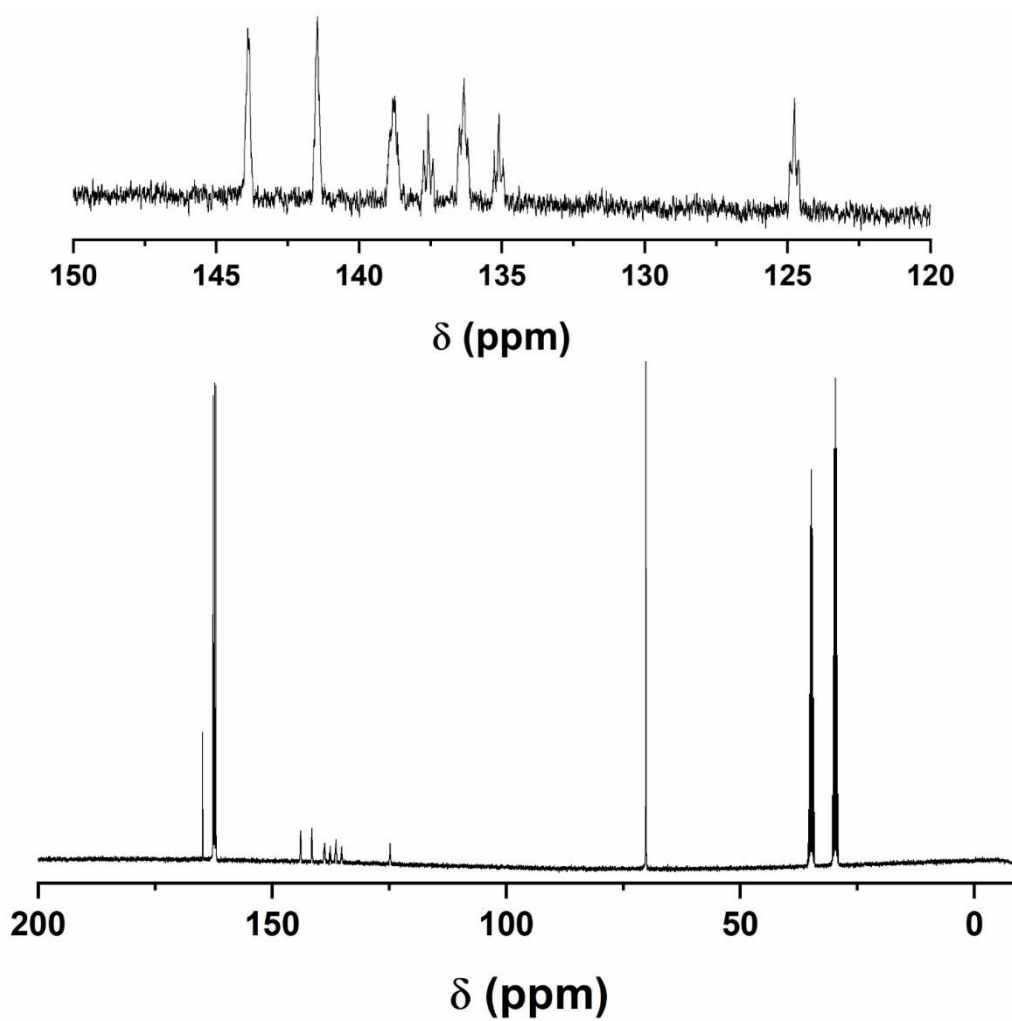
Figure S17. ^{13}C NMR spectrum of complex **6** (DMF-d_6, 101 MHz, 295 K).
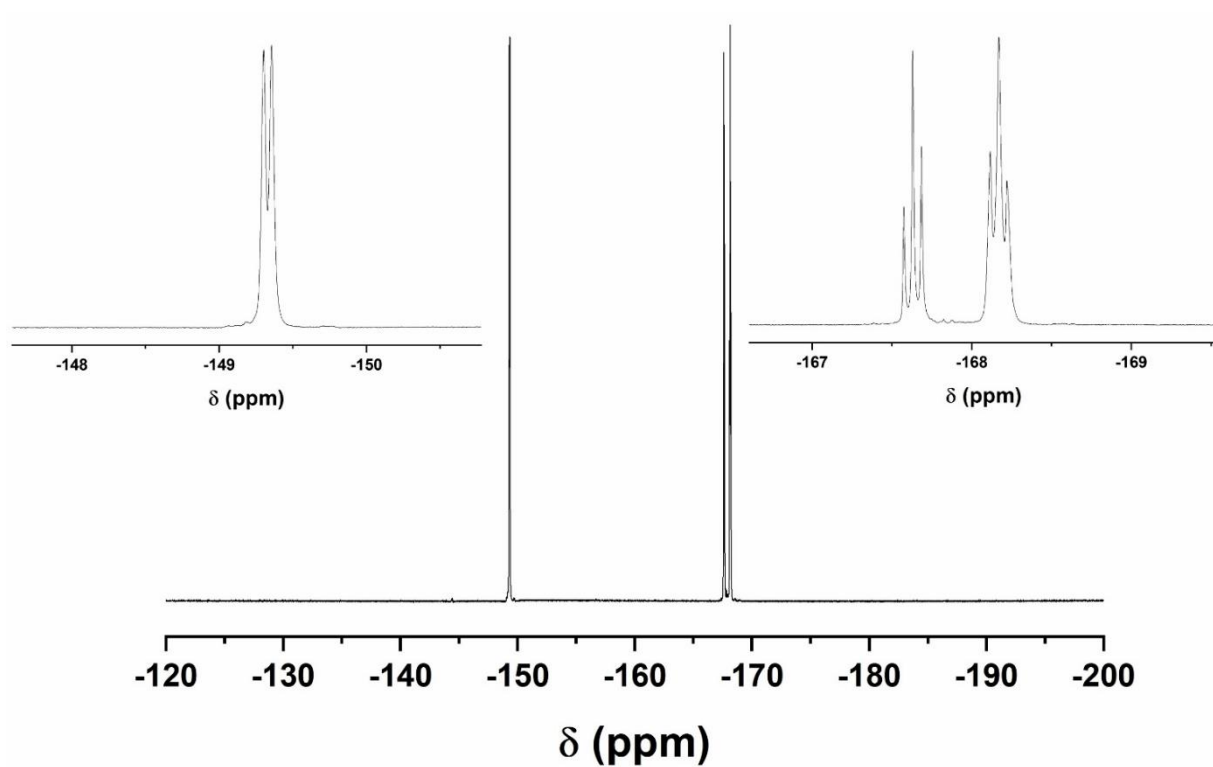
Figure S18. ^{19}F NMR spectrum of complex **6** (CD$_3$CN, 377 MHz, 295 K).
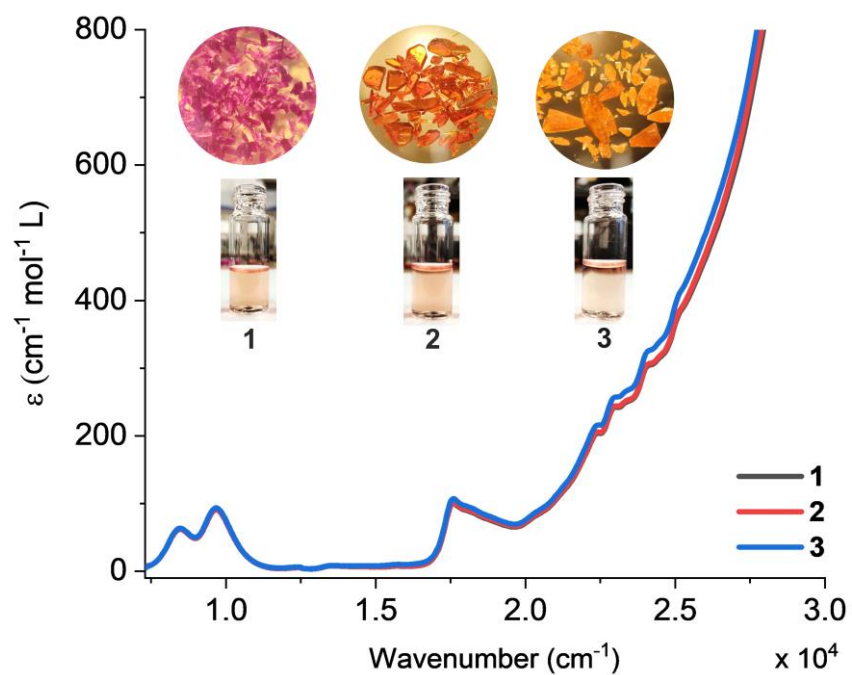
Figure S19. UV-Vis-NIR spectra of complexes **1-3** in DMF solution; the inset shows photographs of the solution samples and crystalline material.
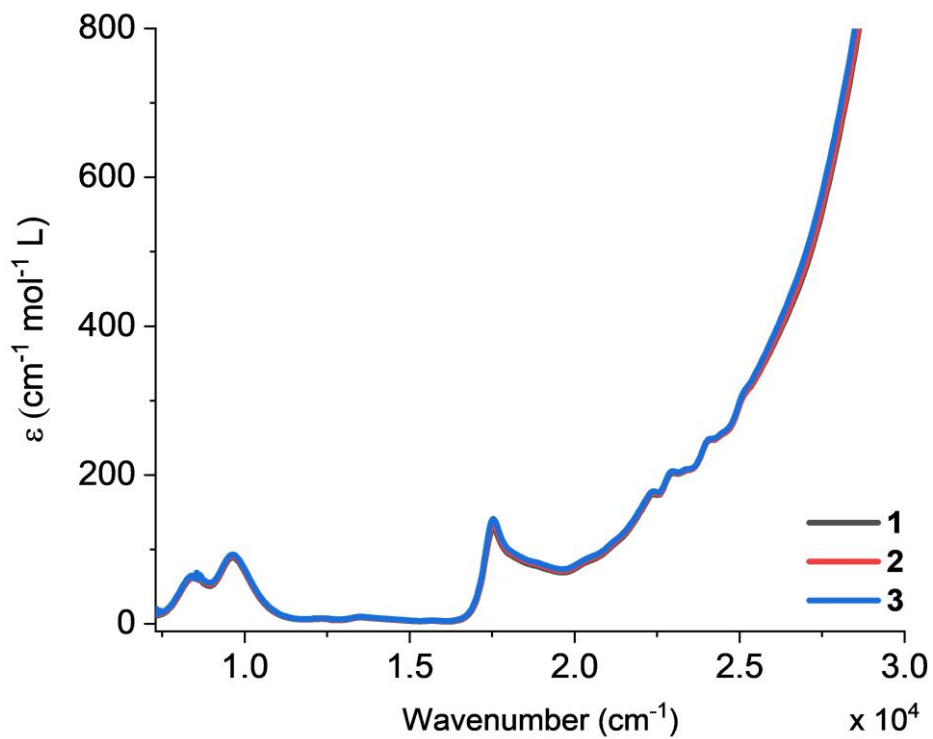
Figure S20. UV-Vis-NIR spectra of complexes **1**-**3** in MeCN.
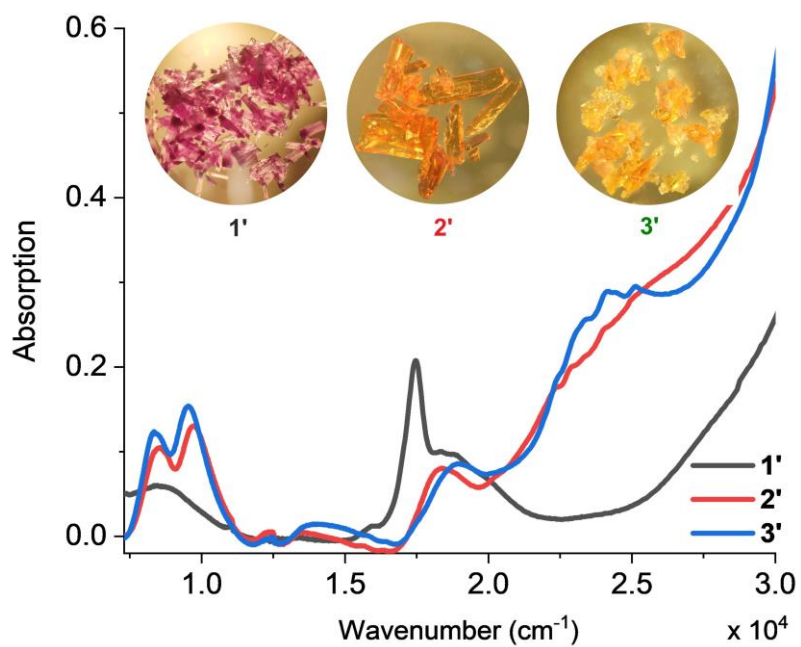
Figure S21. Solid-state UV-Vis-NIR spectra of complexes **1′-3′**.
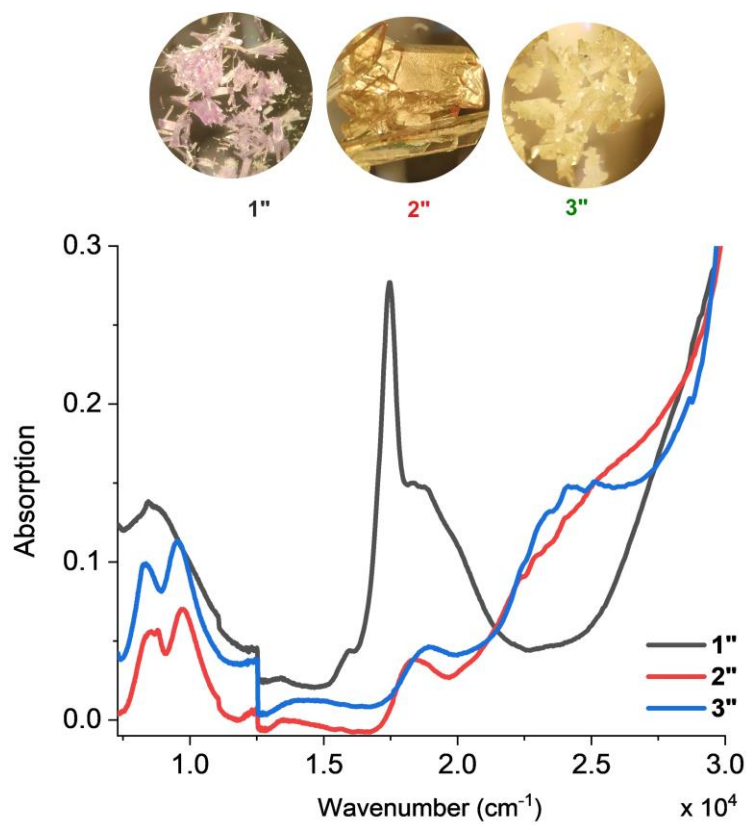
Figure S22. Solid-state UV-Vis-NIR spectra of complexes **1″-3″**.

2. Cyclic Voltammetry
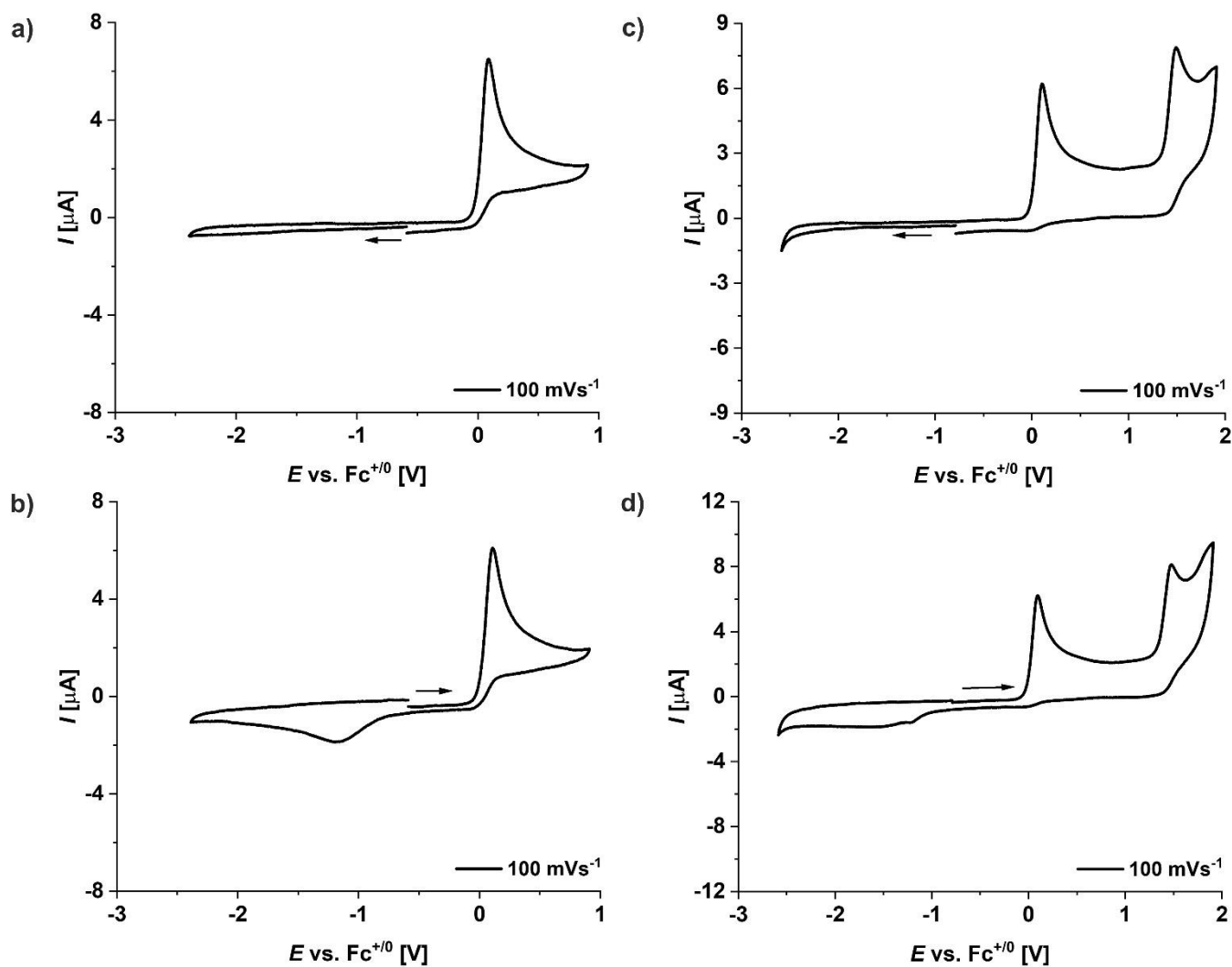
Figure S23. Cyclic voltammograms of complex **1** in MeCN (0.1 M [TBA]PF$_6$) at a scan rate of 100 mV s^{-1}; potentials vs the Fc$^+$/Fc couple.
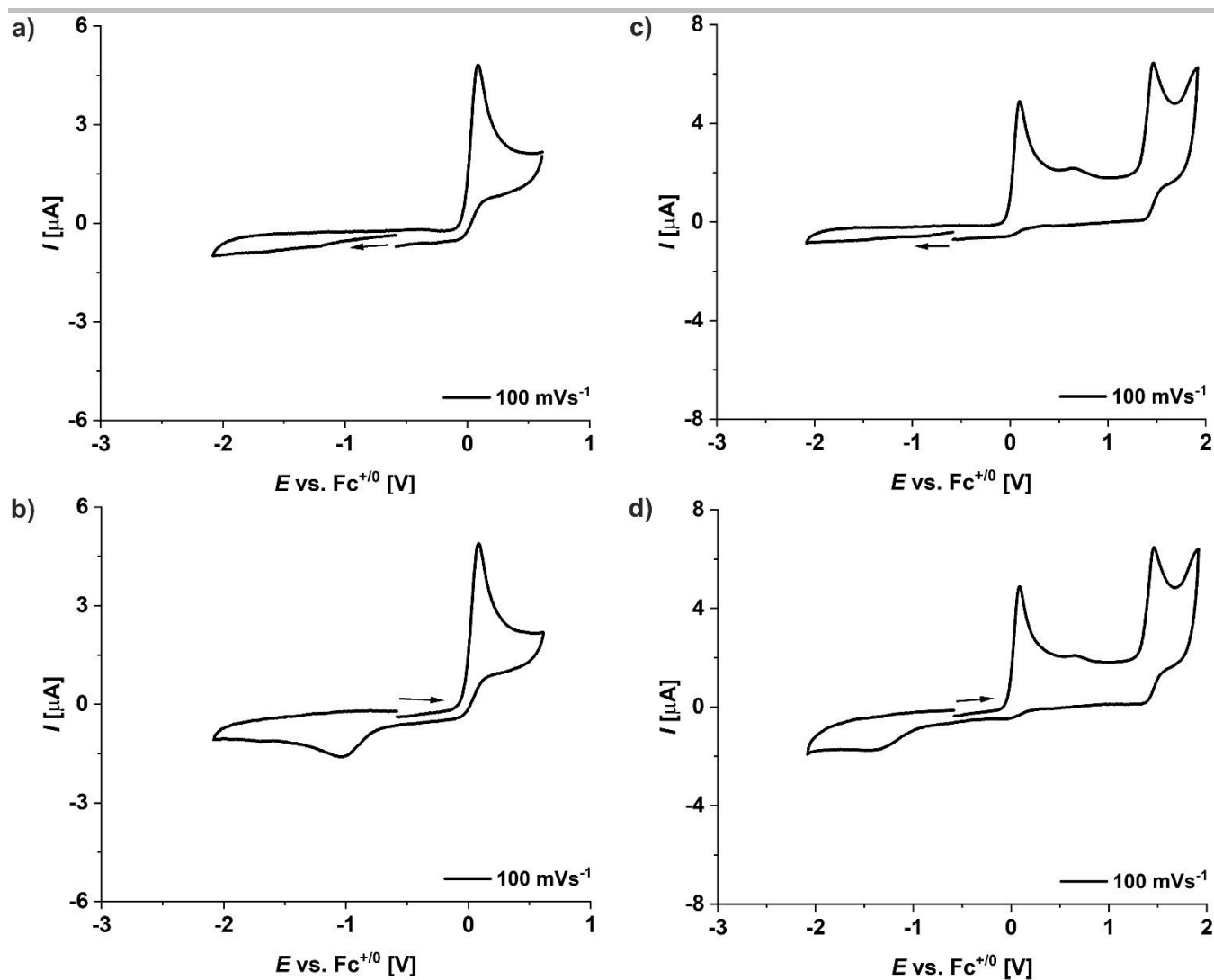
Figure S24. Cyclic voltammograms of complex **2** in MeCN (0.1 M [TBA]PF$_6$) at a scan rate of 100 mV s^{-1}; potentials vs the Fc$^+$/Fc couple.
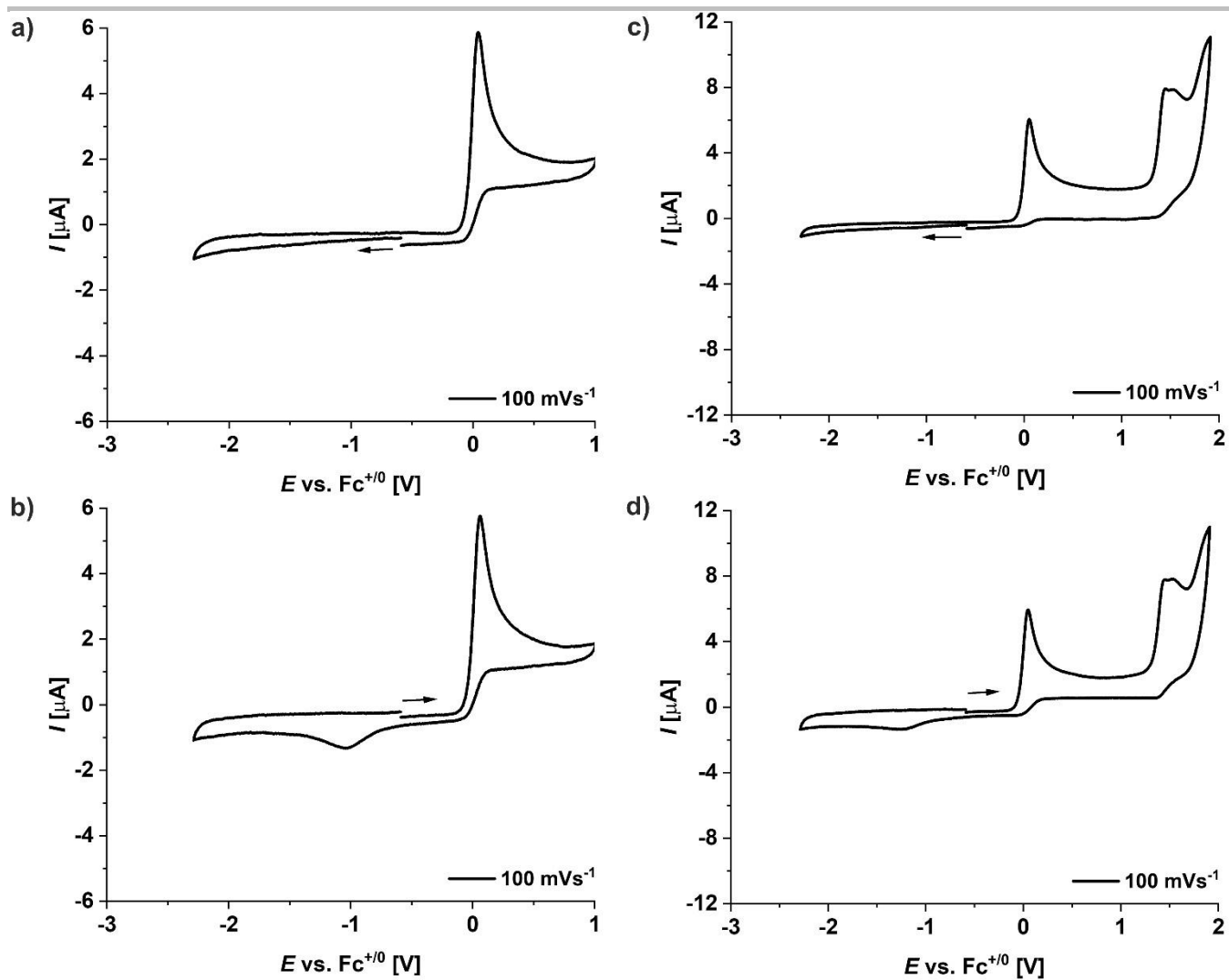
Figure S25. Cyclic voltammograms of complex **3** in MeCN (0.1 M [TBA]PF$_6$) at a scan rate of 100 mV s^{-1}; potentials vs the Fc$^+$/Fc couple.

Figure S26. Cyclic voltammograms of complex [$^{Cl}L_2Co$](TBA)$_2$ (**H**)[4b] in MeCN (0.1 M [TBA]PF$_6$) at a scan rate of 100 mV s^{-1}; potentials vs the Fc$^+$/Fc couple.

3. Crystallographic Structure Determinations

Table S1. Crystal data and refinement details for **1**, **2**, and **3**.

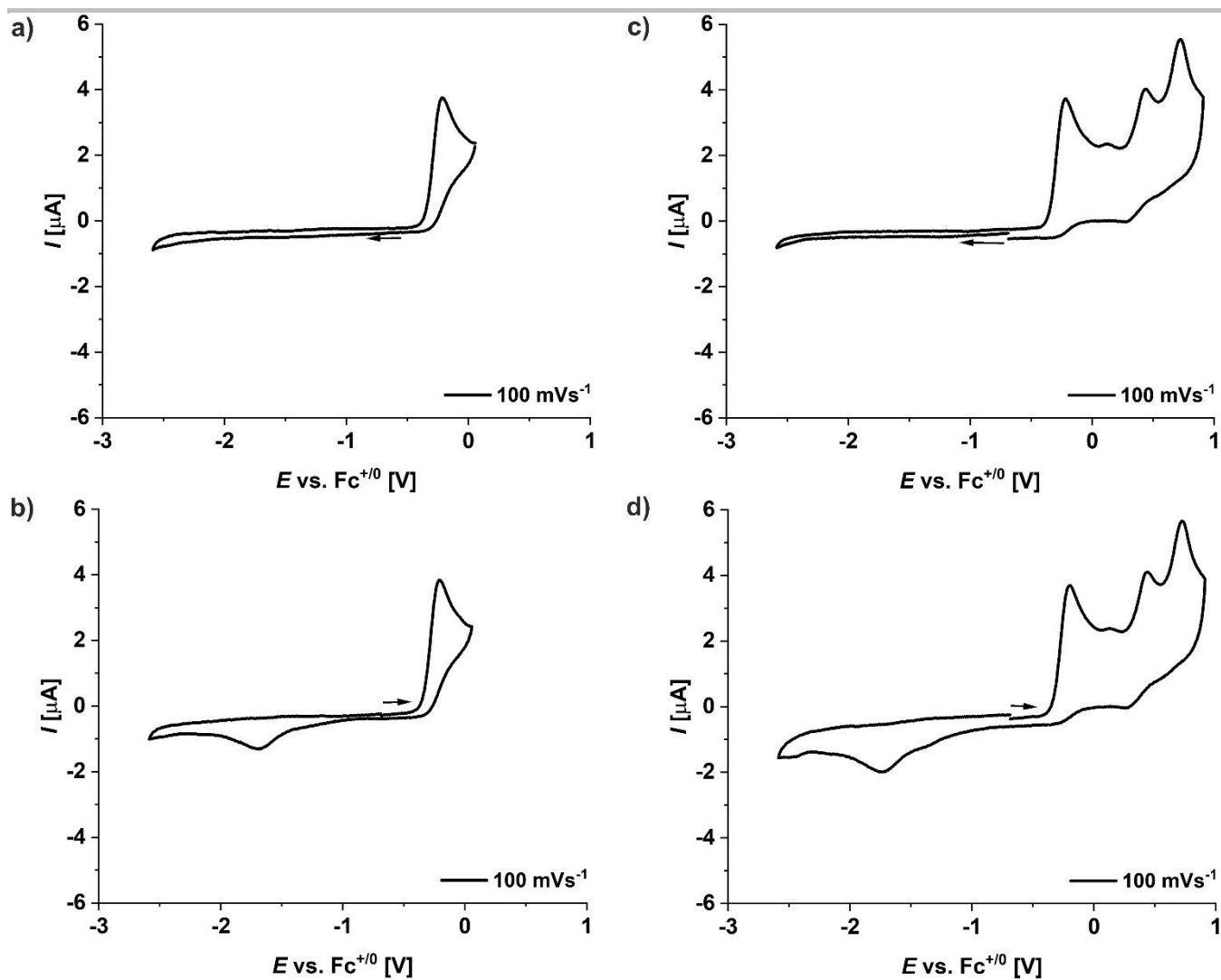| Compound	1 (sg37_21)	2 (sg33_2)	3 (sg34)
empirical formula	$C_{60}H_{72}CoF_{20}N_6O_4$	$C_{76}H_{40}CoF_{20}N_4O_4P_2$	$C_{60}H_{68}CoF_{20}K_2N_4O_{18}$
moiety formula	$C_{28}CoF_{20}N_4O_4{}^{2-}$, $2(C_{16}H_{36}N^+)$	$C_{28}CoF_{20}N_4O_4{}^{2+}$, $2(C_{24}H_{20}P^-)$	$C_{52}H_{48}CoF_{20}K_2N_4O_{16}$, $2(C_4H_{10}O)$
formula weight	1380.16	1573.99	1650.31
T [K]	133(2)	133(2)	133(2)
crystal size [mm³]	0.500 x 0.081 x 0.076	0.500 x 0.330 x 0.160	0.280 x 0.200 x 0.120
crystal system	monoclinic	triclinic	monoclinic
space group	$P2/c$ (No. 13)	$P–1$ (No. 2)	$C2/c$ (No. 15)
a [Å]	23.3077(17)	15.8085(7)	20.7015(9)
b [Å]	25.5036(18)	16.0570(8)	14.4358(5)
c [Å]	22.5731(17)	21.8265(11)	24.8704(12)
α [°]	90	69.295(4)	90
β [°]	106.170(3)	83.670(4)	108.502(4)
γ [°]	90	71.644(4)	90
V [Å³]	12887.3(16)	4918.8(4)	7048.2(5)
Z	8	3	4
ρ [g·cm⁻³]	1.423	1.594	1.555
$F(000)$	5704	2379	3380
μ [mm⁻¹]	0.374	0.425	0.484
T_{min} / T_{max}	0.80 / 0.97 (SADABS)	0.8377 / 0.9372	0.7779 / 0.9265
θ–range [°]	1.945 – 26.372	1.357 – 26.961	1.751 – 26.049
hkl–range	±29, ±31, ±28	–20 to 19, ±20, –27 to 26	–24 to 25, ±17, ±30
measured refl.	310689	67159	45614
unique refl. [R_{int}]	26342 [0.1974]	20854 [0.0702]	45614
observed refl. ($I > 2\sigma(I)$)	13888	12855	26689
data / restr. / param.	26342 / 1 / 1679	20854 / 2874 / 2205	45614 / 0 / 477
goodness–of–fit (F^2)	1.038	1.063	1.080
$R1$, $wR2$ ($I > 2\sigma(I)$)	0.0866 / 0.1888	0.0610 / 0.1956	0.0671 / 0.1897
$R1$, $wR2$ (all data)	0.1696 / 0.2317	0.1011 / 0.2438	0.1214 / 0.2214
res. el. dens. [e·Å⁻³]	–0.546 / 0.784	–0.654 / 0.768	–0.437 / 0.400

Table S2. Crystal data and refinement details for **5** and **6**.

Compound	5 (sg41)	6 (sg40)
empirical formula	$C_{76}H_{40}F_{20}N_4O_4P_2Zn$	$C_{60}H_{68}F_{20}K_2N_4O_{18}Zn$
moiety formula	$C_{28}F_{20}N_4O_4Zn^{2-}$, $2(C_{24}H_{20}P^+)$	$C_{52}H_{48}F_{20}K_2N_4O_{16}Zn$, $2(C_4H_{10}O)$
formula weight	1580.43	1656.75
T [K]	133(2)	133(2)
crystal size [mm³]	0.500 x 0.190 x 0.160	0.500 x 0.490 x 0.450
crystal system	triclinic	monoclinic
space group	P–1 (No. 2)	$C2/c$ (No. 15)
a [Å]	14.5633(7)	20.7537(6)
b [Å]	15.7822(8)	14.4628(3)
c [Å]	16.1274(8)	24.8305(7)
α [°]	71.806(4)	90
β [°]	82.645(4)	108.382(2)
γ [°]	68.825(4)	90
V [Å³]	3283.2(3)	7072.7(3)
Z	2	4
ρ [g·cm⁻³]	1.599	1.556
$F(000)$	1592	3392
μ [mm⁻¹]	0.537	0.587
T_{min} / T_{max}	0.7762 / 0.9801	0.5879 / 0.6809
θ–range [°]	1.329 – 26.871	1.728 – 26.847
hkl–range	±18, ±19, ±20	±26, ±18, –30 to 31
measured refl.	45577	50226
unique refl. [R_{int}]	13939 [0.0575]	7506 [0.0503]
observed refl. ($I > 2\sigma(I)$)	9685	6621
data / restr. / param.	13939 / 1024 / 1464	7506 / 0 / 477
goodness–of–fit (F^2)	1.115	1.123
$R1$, $wR2$ ($I > 2\sigma(I)$)	0.0718 / 0.1404	0.0448 / 0.1481
$R1$, $wR2$ (all data)	0.1029 / 0.1592	0.0521 / 0.1616
res. el. dens. [e·Å⁻³]	–1.054 / 1.529	–0.301 / 0.720
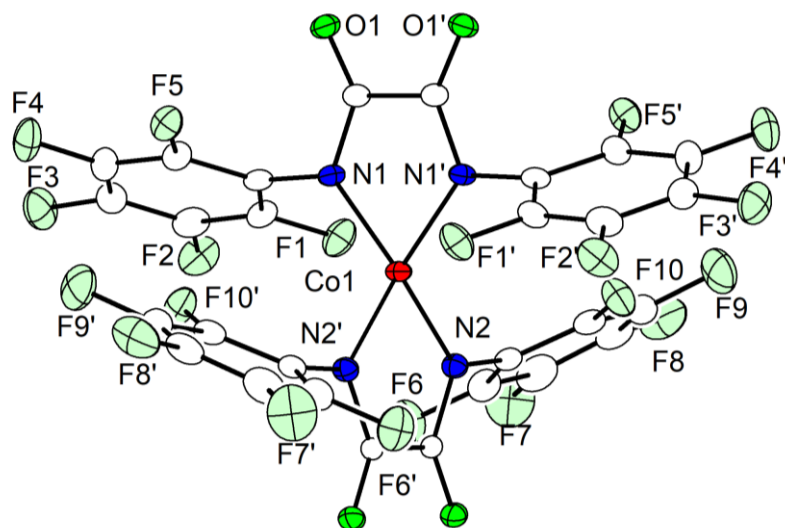
Figure S27. Plot (30% probability thermal ellipsoids) of the molecular structure of the anionic part of **1**. Only one of the four crystallographically independent molecules is shown. Selected bond lengths [Å] and angles [°]: Co1–N1 1.988(4), Co1–N2 1.978(4); N1–Co1–N2 125.45(17), N1–Co1–N2' 123.53(17), N1'–Co1–N1 82.5(2), N2'–Co1–N2 82.3(2). Symmetry transformation used to generate equivalent atoms: (') 1–x, y, 1/2–z.
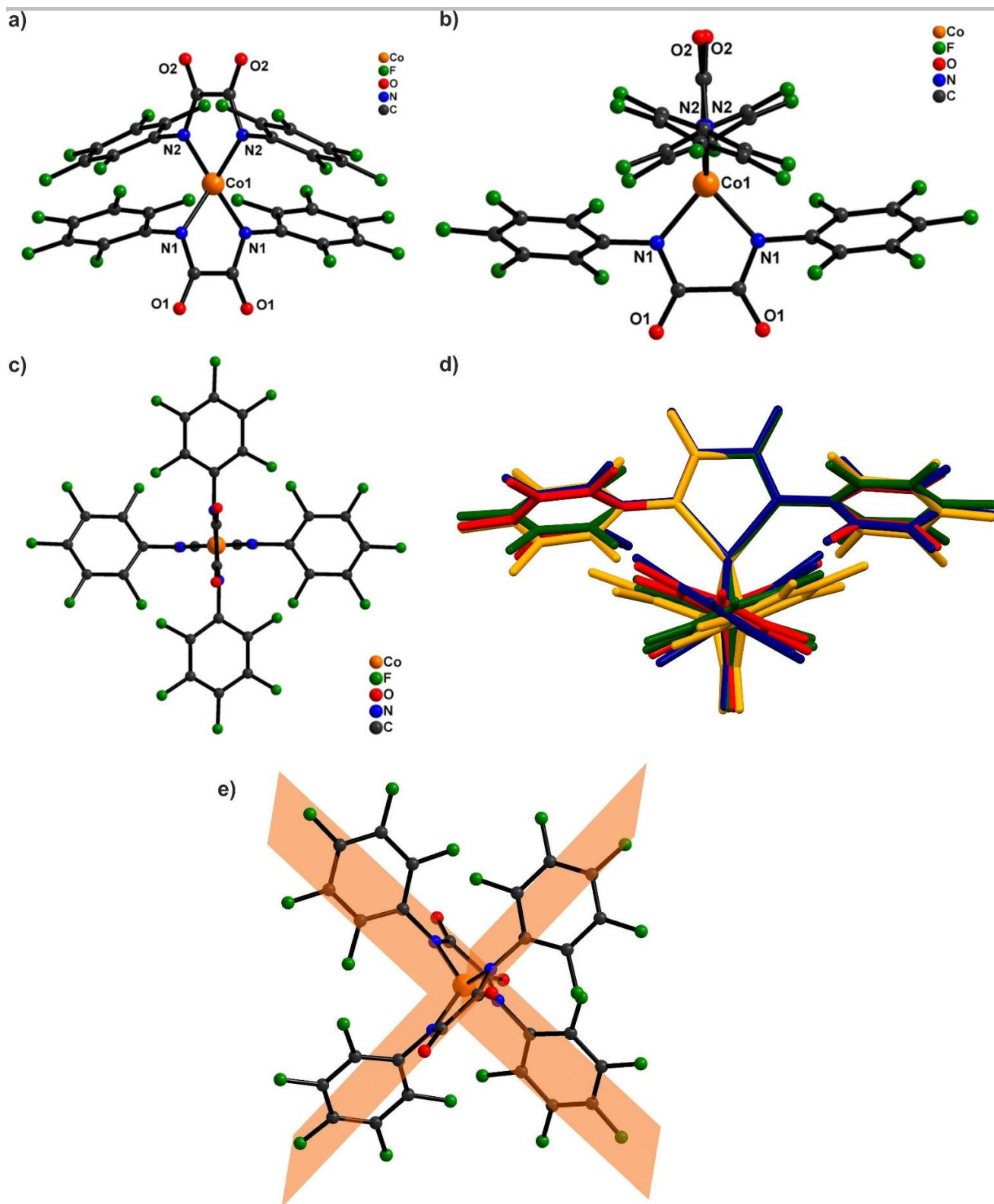
Figure S28. (a-c) View of the molecular structure of the anionic part of **1** in the asymmetric part of the unit cell through different orientations. Only one of the four crystallographically independent molecules is shown. (d) Overlay of the different entities showing the orthogonal ligation of the central Co(II) ion in complex **1**. (e) A view of the two intersecting N-Co-N planes in **1**.

Figure S29. Plot (30% probability thermal ellipsoids) of the molecular structure of the anionic part of **2**. Only one of the two crystallographically independent molecules is shown. Selected bond lengths [Å] and angles [°]: Co1–N1 1.966(3), Co1–N2 1.988(3), Co1–N11 1.996(3), Co1–N12 1.972(3); N1–Co1–N2 82.38(12), N11–Co1–N12 82.41(12), N1–Co1–N11 105.64(13), N1–Co1–N12 148.41(14), N2–Co1–N11 148.90(13), N2–Co1–N12 106.68(13).

Figure S30. (a-c) View of the molecular structure of the anionic part of **2** through different orientations showing $\pi-\pi$ stacking between the perfluorophenyl rings. Only one of the two crystallographically independent molecules is shown. (d) Overlay of the two disordered part structural equivalence. (e) A view of the two intersecting N-Co-N planes in **2**.
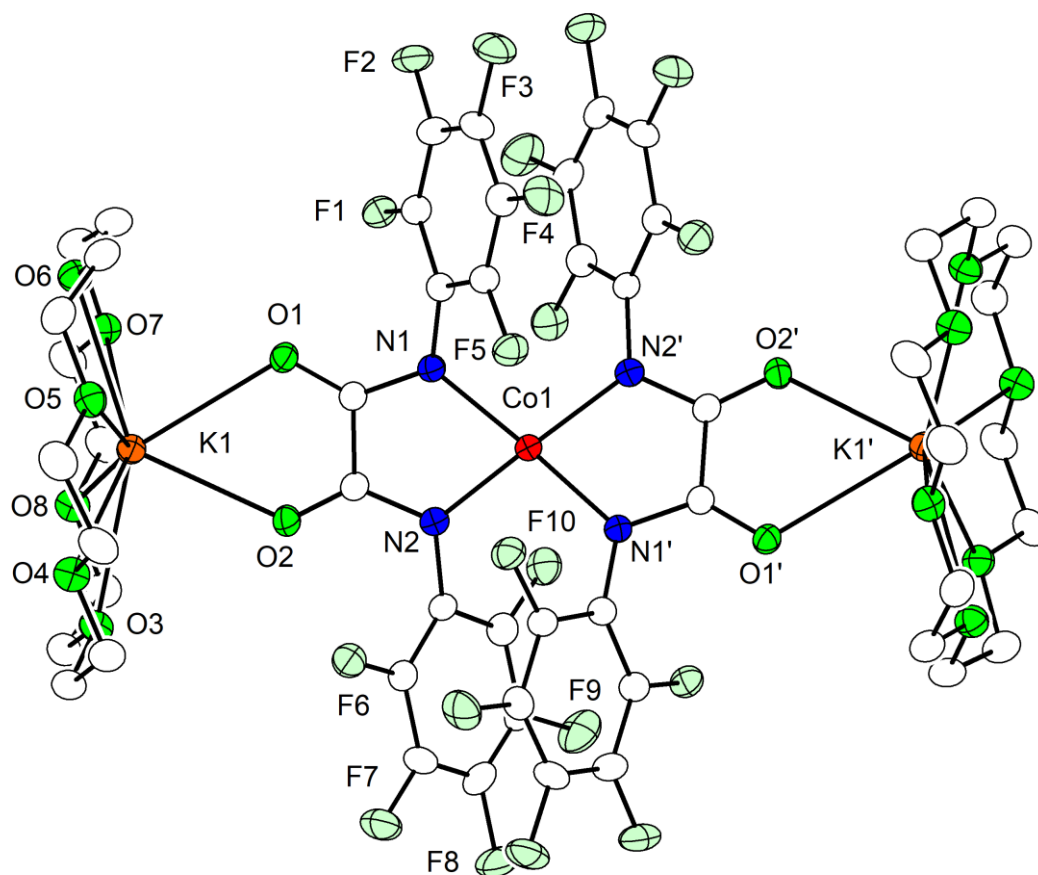
Figure S31. Plot (30% probability thermal ellipsoids) of the molecular structure of **3** (hydrogen atoms omitted for clarity). Selected bond lengths [Å] and angles [°]: Co1–N1 1.994(5), Co1–N2 1.990(5), K1–O1 2.827(4), K1–O2 2.699(4); N1–Co1–N2 82.82(19), N1–Co1–N2' 105.6(2), N1–Co1–N1' 148.3(3), N2–Co1–N2' 149.3(3), O1–K1–O2 59.64(12). Symmetry transformation used to generate equivalent atoms: (') 1–*x, y*, 1/2–*z*.
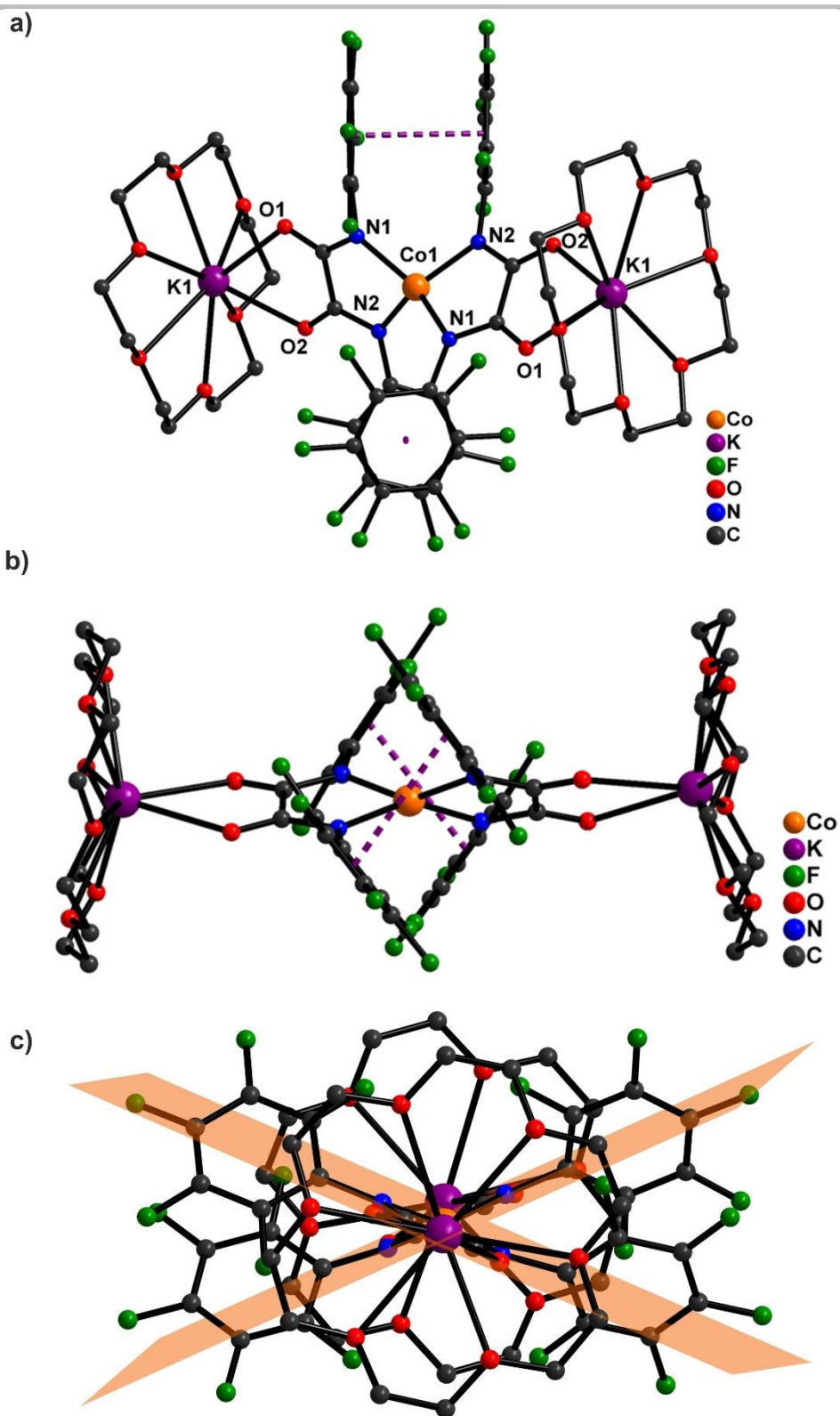
Figure S32. (a and b) View of the molecular structure of complex **3** in two orientations showing $\pi-\pi$ stacking between the perfluorophenyl rings. (c) A view of the two intersecting N-Co-N planes in **3**.
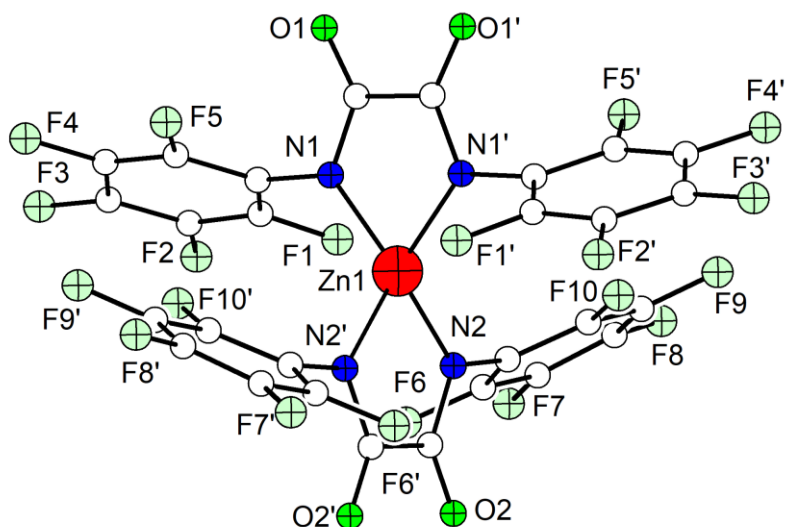
Figure S33. Plot of the molecular structure of the anionic part of **4**. Only one of the four crystallographically independent molecules is shown. Symmetry transformation used to generate equivalent atoms: (') 1−*x*, *y*, 1/2−*z*.
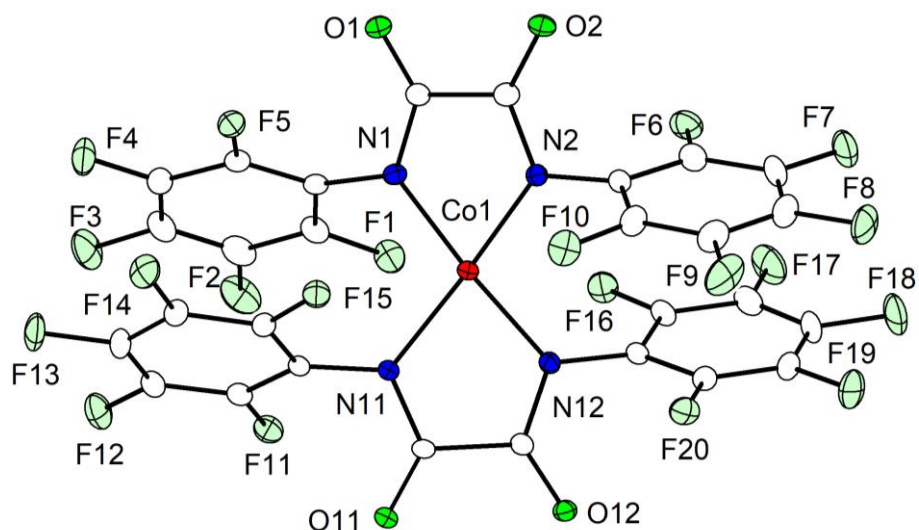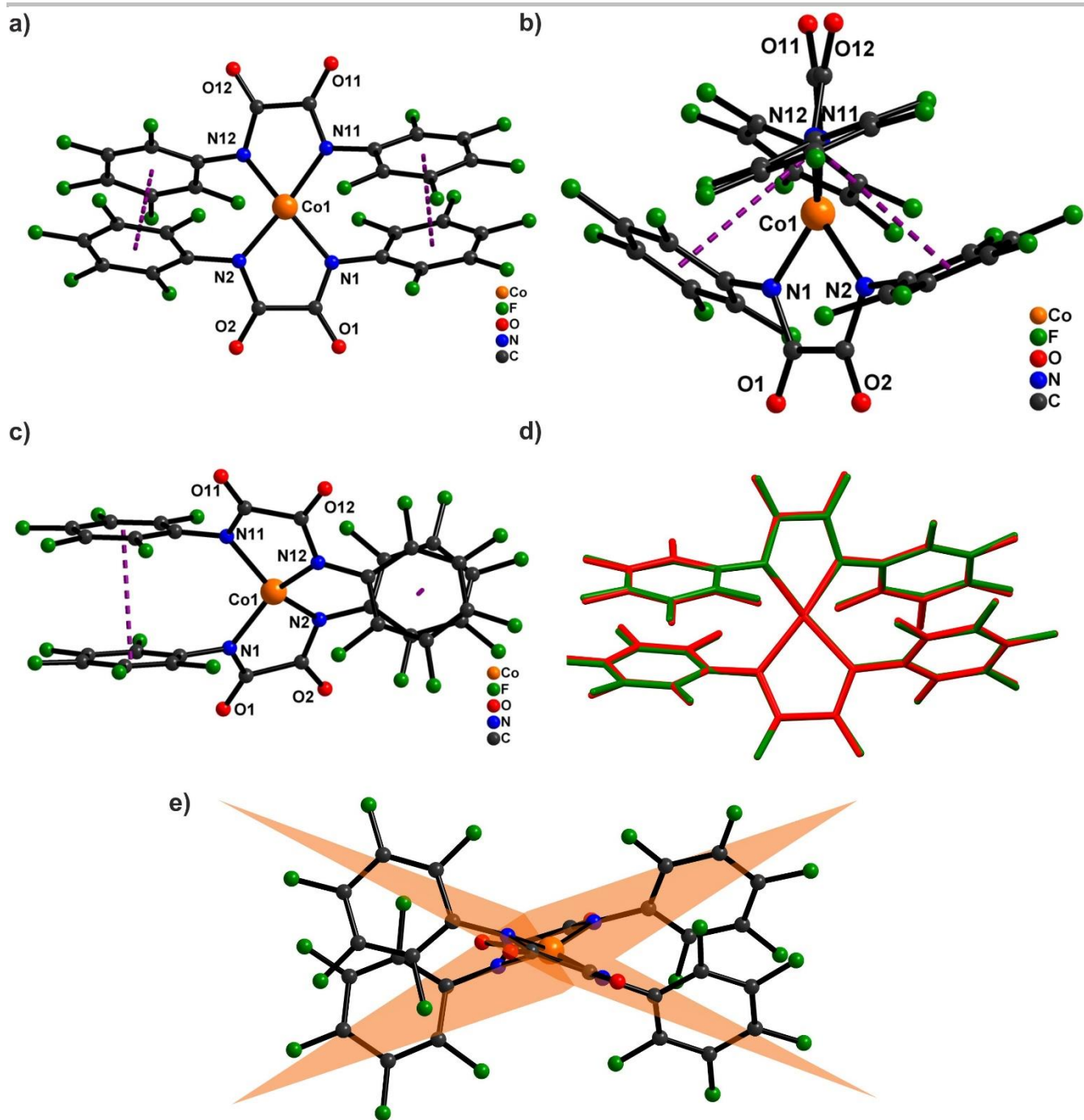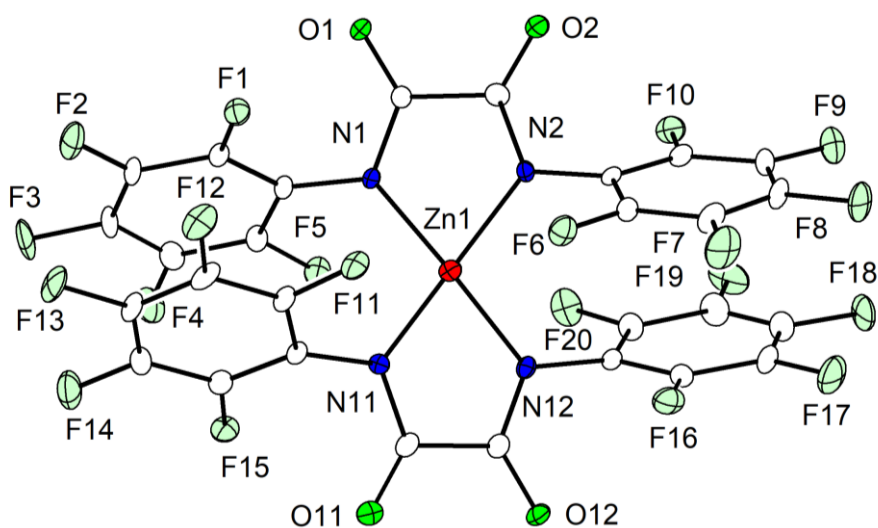

Figure S34. Plot (30% probability thermal ellipsoids) of the molecular structure of the anionic part of **5**. Selected bond lengths [Å] and angles [°]: Zn1–N1 2.000(4), Zn1–N2 1.992(4), Zn1–N11 1.940(4), Zn1–N12 2.017(4); N1–Zn1–N2 83.17(17), N11–Zn1–N12 83.55(17), N1–Zn1–N11 107.4(2), N1–Zn1–N12 141.8(2), N2–Zn1–N11 146.8(2), N2–Zn1–N12 107.8(2).
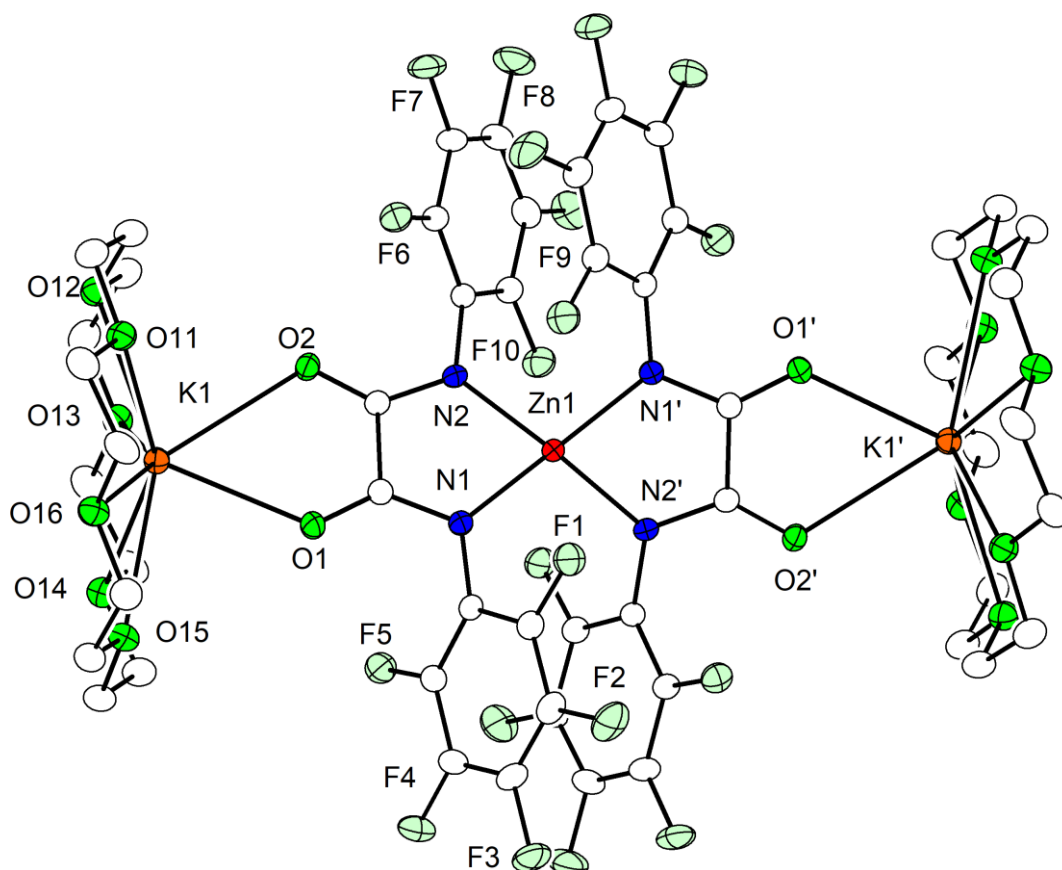
Figure S35. Plot (30% probability thermal ellipsoids) of the molecular structure of **6** (hydrogen atoms omitted for clarity). Selected bond lengths [Å] and angles [°]: Zn1–N1 1.991(2), Zn1–N2 1.990(2), K1–O1 2.692(2), K1–O2 2.821(2); N1–Zn1–N1' 145.14(14), N2–Zn1–N2' 146.67(14), N1–Zn1–N2 83.12(9), N1–Zn1–N2' 106.95(9), O1–K1–O2 59.60(6). Symmetry transformation used to generate equivalent atoms: (') −x, y, 1/2−z.
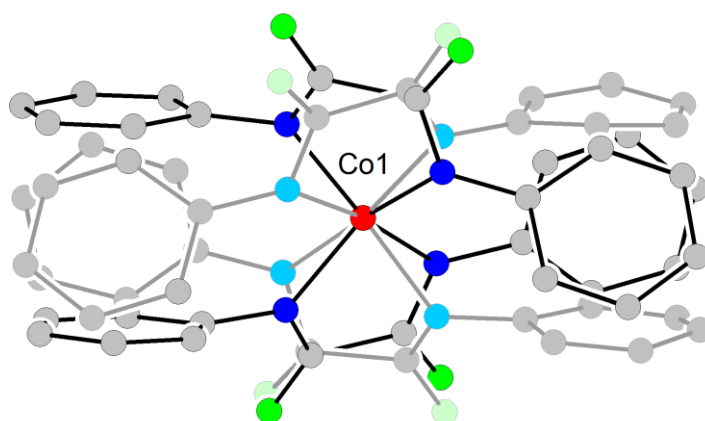

Figure S36. Emphasis of the disorder in **2** for one of the two molecules. A similar disorder has been observed in **5**.

Table S3. SHAPE measures of tetracoordinate Co(II) complexes.[1]

Complex	Metal Center	vTBPY-4	SS-4	T-4	SP-4	τ_4	Dihedral angle between N-Co-N planes
1	Co1	8.739	9.541	5.477	24.914	0.7876	88.20
	Co2	8.796	9.765	5.52	25.407	0.7868	89.17
	Co3	8.965	8.557	5.715	22.073	0.7859	82.31
	Co4	10.234	7.634	7.051	17.569	0.7723	72.51
2	Co1	14.745	7.286	12.038	8.571	0.448	48.79
	Co1	14.429	6.558	12.582	8.389	0.433	49.08
	Co2	15.185	7.144	12.513	8.18	0.434	47.80
3	Co1	15.048	7.387	12.186	8.261	0.4425	47.97

vTBPY-4 (Vacant trigonal bipyramid) = C_{3v}

SS-4 (Seesaw) = C_{2v}

T-4 (Tetrahedron) = T_d

SP-4 (Square) = D_{4h}

Table S4. Selected bond distances (Å) and angles (º) in complex **1**.

Co(1)-N(2)	1.978(4)	N(2)#1-Co(1)-N(2)	82.3(2)	N(22)-Co(3)-N(22)#3	82.6(3)
Co(1)-N(1)	1.988(4)	N(2)#1-Co(1)-N(1)#1	125.46(17)	N(22)-Co(3)-N(21)#3	120.57(19)
Co(2)-N(11)	1.992(4)	N(2)#1-Co(1)-N(1)	123.53(17)	N(22)#3-Co(3)-N(21)#3	128.6(2)
Co(2)-N(12)	1.994(4)	N(1)#1-Co(1)-N(1)	82.5(2)	N(21)#3-Co(3)-N(21)	82.2(3)
Co(3)-N(22)	1.988(5)	N(11)-Co(2)-N(11)#2	82.4(2)	N(32)-Co(4)-N(32)#4	81.5(3)
Co(3)-N(21)	1.991(4)	N(11)-Co(2)-N(12)#2	124.92(17)	N(32)-Co(4)-N(31)	134.56(17)
Co(4)-N(32)	1.995(4)	N(11)#2-Co(2)-N(12)#2	124.09(19)	N(32)#4-Co(4)-N(31)	116.51(17)
Co(4)-N(31)	2.012(4)	N(12)#2-Co(2)-N(12)	82.3(2)	N(31)-Co(4)-N(31)#4	81.4(2)

Table S5. Selected bond distances (Å) and angles (º) in complex **2**.

Co(1)-N(2B)	1.993(9)	Co(1)-N(1)	1.967(3)	N(1)-Co(1)-N(2)	82.32(13)
Co(1)-N(11)	1.998(3)	Co(1)-N(12)	1.977(3)	N(12)-Co(1)-N(11)	82.55(13)
Co(1)-N(1B)	2.025(9)	Co(1)-N(12B)	1.812(10)	N(2B)-Co(1)-N(1B)	80.8(3)
Co(1)-N(11B)	2.095(9)	Co(1)-N(2)	1.988(3)	N(12B)-Co(1)-N(11B)	84.0(3)
Co(2)-N(22A)	2.030(6)	Co(2)-N(21A)	1.927(5)	N(21A)-Co(2)-N(22A)	74.4(2)
Co(2)-N(22B)	2.034(6)	Co(2)-N(21B)	1.980(6)	N(21B)-Co(2)-N(22B)	74.4(2)

Table S6. Selected bond distances (Å) and angles (º) in complex **3**.

Co(1)-N(2)#1	1.990(5)	K(1)-O(2)	2.699(4)	N(2)-Co(1)-N(1)#1	105.6(2)
Co(1)-N(2)	1.990(5)	K(1)-O(1)	2.827(4)	N(2)#1-Co(1)-N(1)	105.6(2)
Co(1)-N(1)#1	1.994(5)	N(2)#1-Co(1)-N(2)	149.3(3)	N(2)-Co(1)-N(1)	82.82(19)
Co(1)-N(1)	1.994(5)	N(2)#1-Co(1)-N(1)#1	82.82(19)	N(1)#1-Co(1)-N(1)	148.3(3)

4. Magnetic Measurements

The experimental data obtained were analysed with the julX_2S program[2] using a fitting procedure to the spin Hamiltonian given in eq. (1).

$$\hat{H} = D\left[\hat{S}_z^2 - \frac{1}{3}S(S+1)\right] + E(\hat{S}_x^2 - \hat{S}_y^2) + \mu_B \vec{B}\boldsymbol{g}\vec{S}....(1)$$

where D and E represent the axial and the rhombic zero-field splitting (ZFS) parameters, S, S_x, S_y and S_z represent the total spin and its corresponding x, y and z components, μ_B, $\boldsymbol{g}$, B represent the Bohr magneton, the g-tensor, and the magnetic flux density, respectively. The magnetic susceptibility data for complexes **1-3** were simultaneously fitted along with the variable-temperature variable-field (VTVH) magnetization data. However, the number of parameters used in the data modeling was minimized to the extent possible. For complexes **1-3**, no satisfactory fits could be obtained using an isotropic g value as it did not produce the desired line shape of the curve. Further, anisotropic g values with positive D or isotropic g values with negative D also did not lead to any reasonable fits. Including E values also did not improve the quality of the fits for complex **1**. Satisfactory fits could be only obtained using anisotropic g values with large negative D for complex **1**. On the other hand, in the case of complexes **2** and **3**, the inclusion of the rhombic component E was necessary to improve the quality of the fits. It should be noted that the fitting of only variable temperature $\chi_M T$ data without VTVH magnetization data was not pursued, as it leads to an unreliable sign and magnitude of the ZFS parameters, D and E.

Figure S37. Variable field magnetization at 2.0 K for **1**.
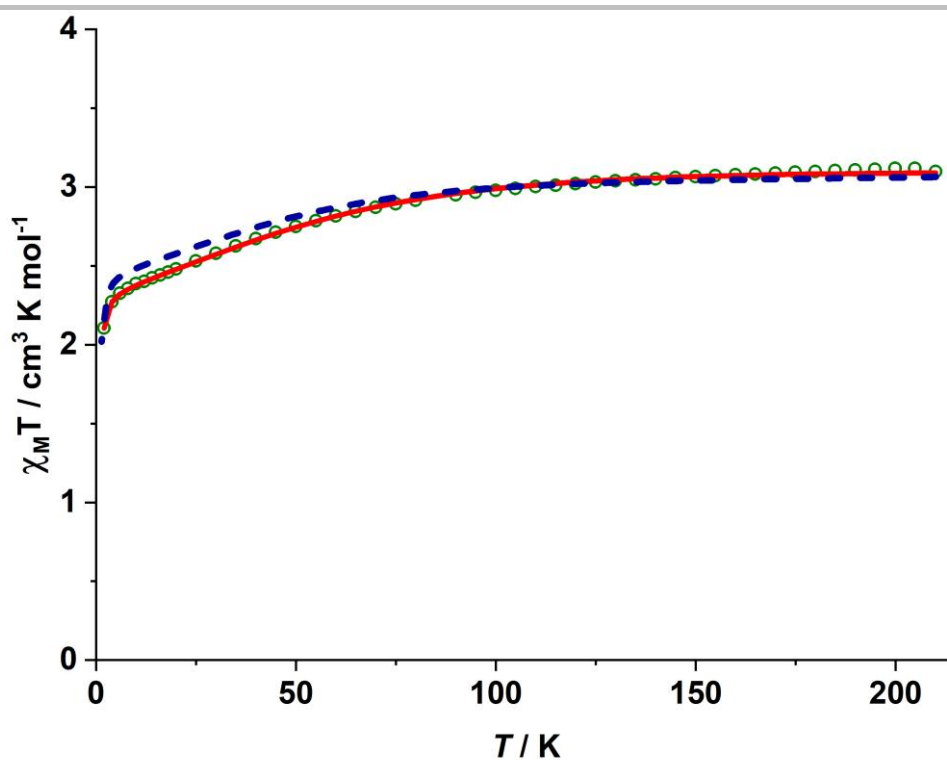
Figure S38. Variable-temperature $\chi_M T$ product for complex **2** measured under an applied dc field of 0.5 T. The solid line is the best fit and the dashed line is the theoretical prediction with CASSCF/NEVPT2.
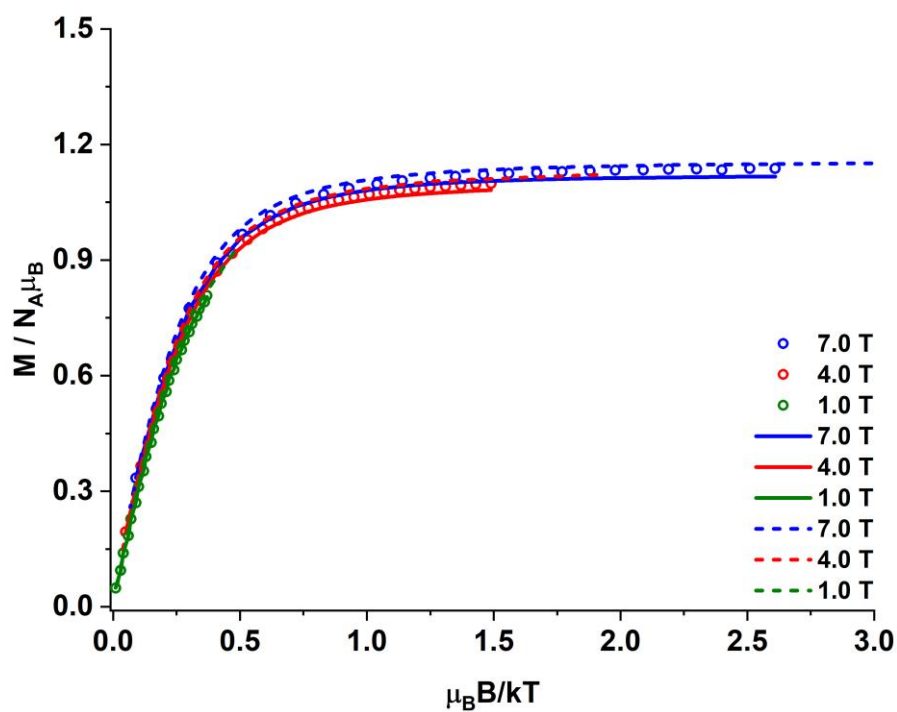
Figure S39. Variable-temperature variable-field magnetization for complex **2.** The solid line is the best fit and the dashed line is the theoretical prediction with CASSCF/NEVPT2.
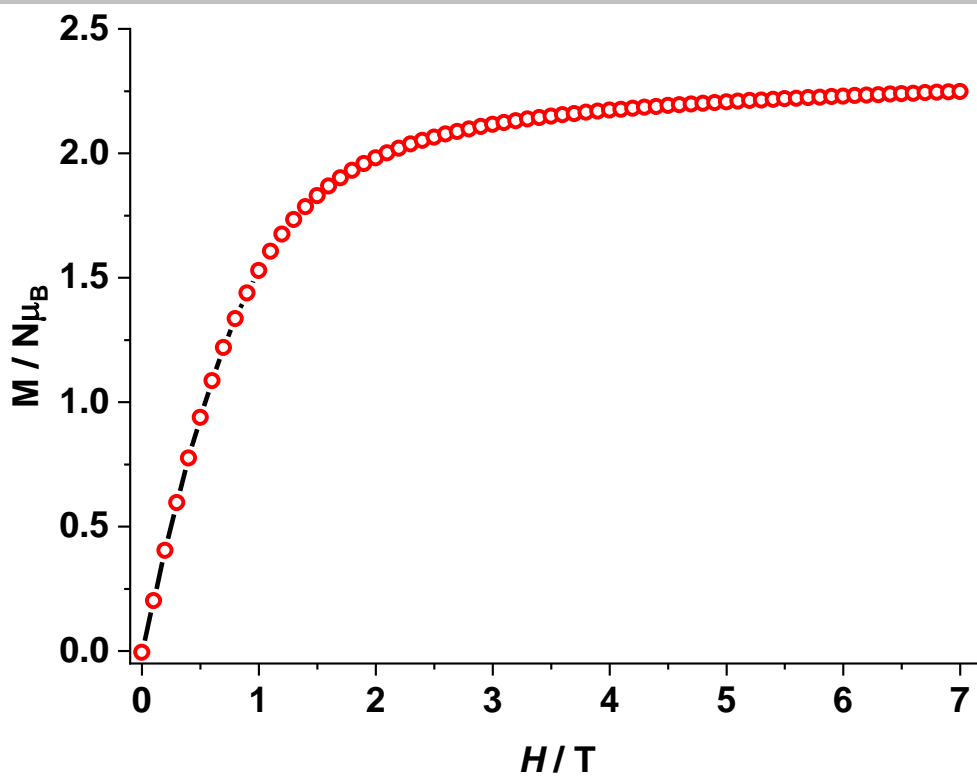
Figure S40. Variable field magnetization at 2.0 K for **2**.
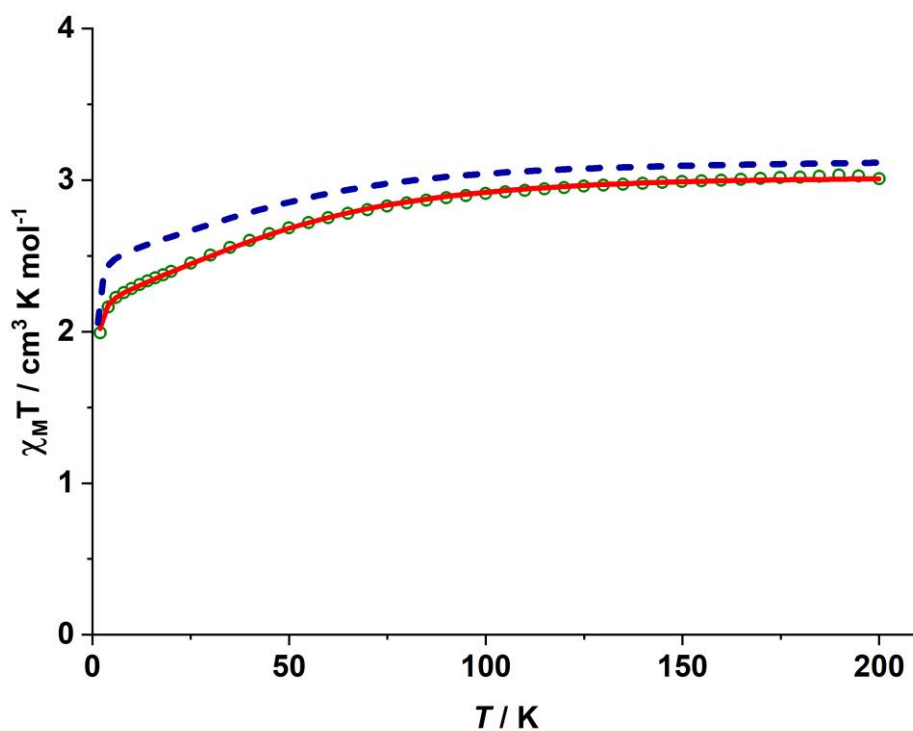
Figure S41. Variable-temperature χ_MT product for complex **3** measured under an applied dc field of 0.5 T. The solid line is the best fit and the dashed line is the theoretical prediction with CASSCF/NEVPT2.

Figure S42. Variable-temperature variable-field magnetization for complex **3.** The solid line is the best fit and the dashed line is the theoretical prediction with CASSCF/NEVPT2.
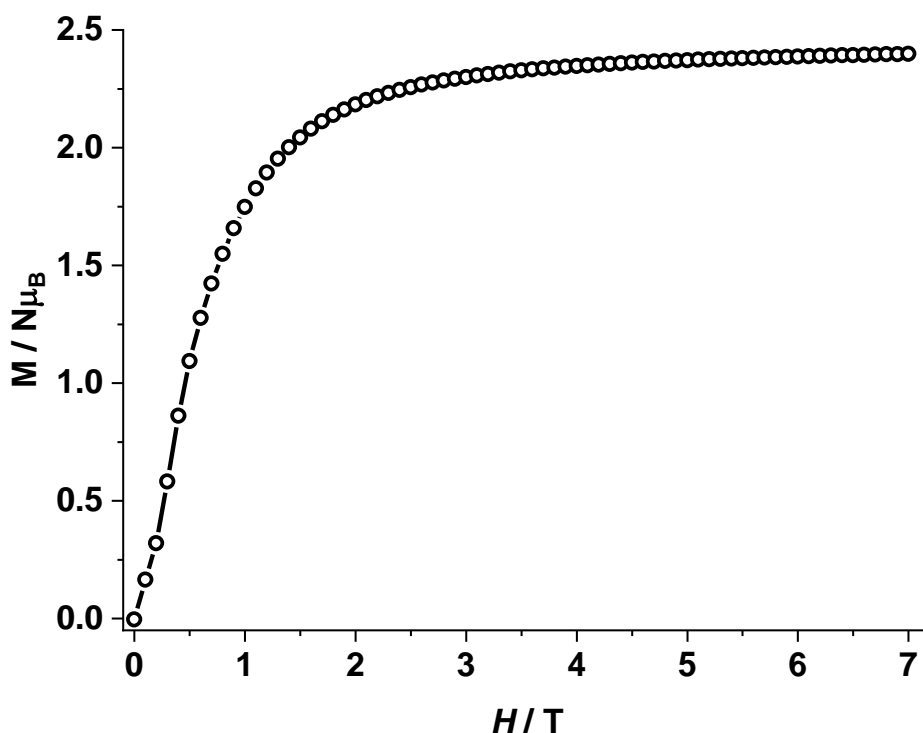

Figure S43. Variable field magnetization at 2.0 K for **3**.

Analysis of the relaxation dynamics

The relaxation times were extracted by fitting the in-phase (χ_M') and out-of-phase (χ_M'') components of the ac susceptibility to a generalized Debye model using the CC-FIT2 prog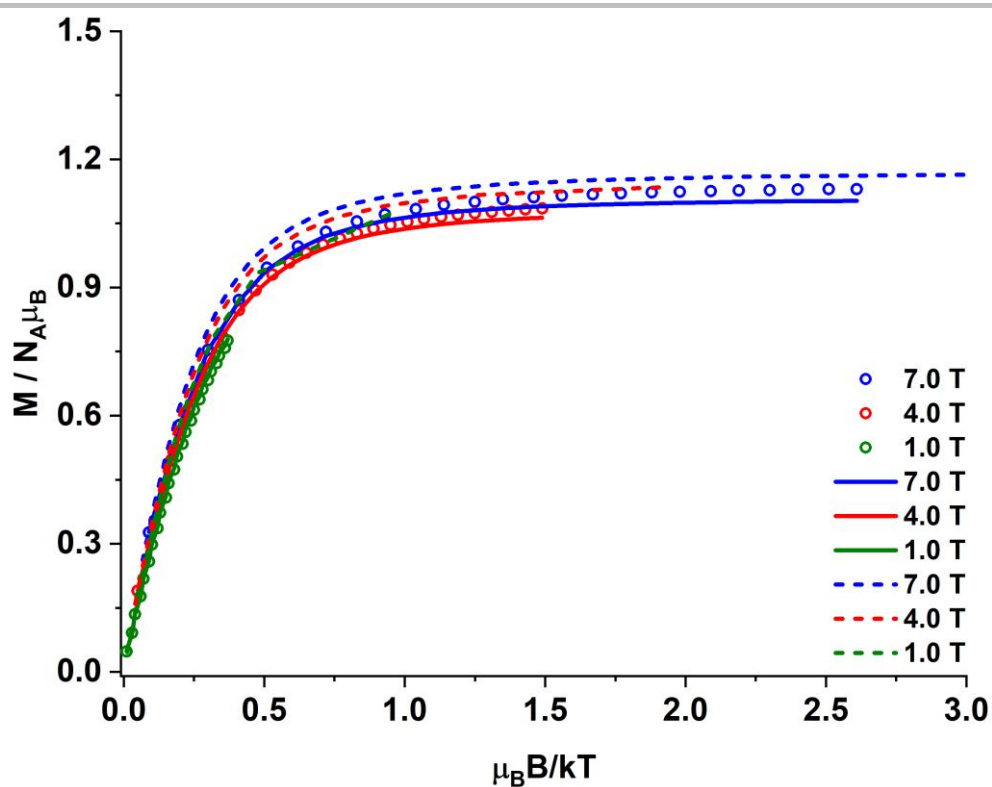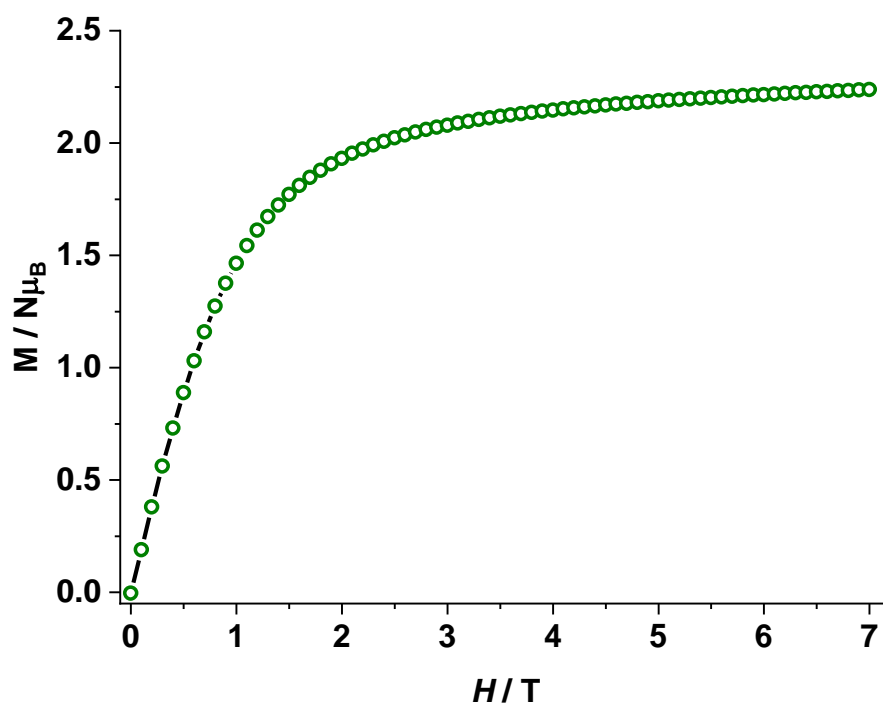ram.[3] Fits that seemed erroneous were excluded during analysis. The temperature dependence of the relaxation time was analyzed by considering relaxation via quantum tunnelling, the Raman process, and the Orbach relaxation pathway, respectively as shown in the following equation,

$$1/\tau = 1/\tau_{QTM} + CT^n + \tau_o^{-1}\exp(-U_{eff}/k_BT)$$

The least possible number of parameters has been used in all cases to avoid overparameterization. For complex **1**, no reasonable fit was obtained for the relaxation rates over the entire temperature range with any combination of these relaxation processes. As the Orbach process begins to dominate only at high temperatures, it is not straightforward to refine the Orbach parameters and include their contribution to the fit, as has been observed in several Co(II)-based SIMs with high anisotropy.[4] As a standard practice with highly anisotropic SIMs,[4] U_{eff} was restrained to $2D$ like in the related complex $[^{Cl}L_2Co](TBA)_2$ (**A**)[4b] having only one Co(II) molecule in the asymmetric part of the unit cell. Restraining n to 3 and U_{eff} to 410 K reproduced well the relaxation times at higher temperatures but showed significant deviation at lower temperatures. Using a higher value of n was not fruitful. The application of an external dc field only slightly affected the relaxation times at lower temperatures, and the inclusion of a quantum tunneling process also did not lead to a satisfactory fit of the data. As already stated in the main text, this might be either due to different contributions from the four crystallographically independent Co(II) complexes with a significant variation in dihedral angles (72.6 to 89.2°) or due to some complex relaxation mechanisms operating at lower temperatures. Considering only the relaxation times at lower temperatures below 20 K or 15 K was also not effective. Additionally**,** it is worth mentioning that the inclusion of a direct process did not improve the quality of the fits. However, it seems that the relaxation is mostly dominated by the Raman relaxation process for complex **1** over the entire temperature range, with the Orbach process being relevant mostly at higher temperatures at the limits of the frequency range of the magnetometer. Based on these challenges and consideratios, we refrain from over-analyzing the fits for complex **1** or **1'**; additional exhaustive studies are likely required to derive unambiguous conclusions for this system. For complexes **2** and **3** ins solid state, as well as for complexes **1** and **2** in frozen solution, the relaxation rate over the entire temperature range could be fit satisfactorily by considering either the Raman relaxation pathway only, or a combination of the Raman relaxation pathway and QTM.
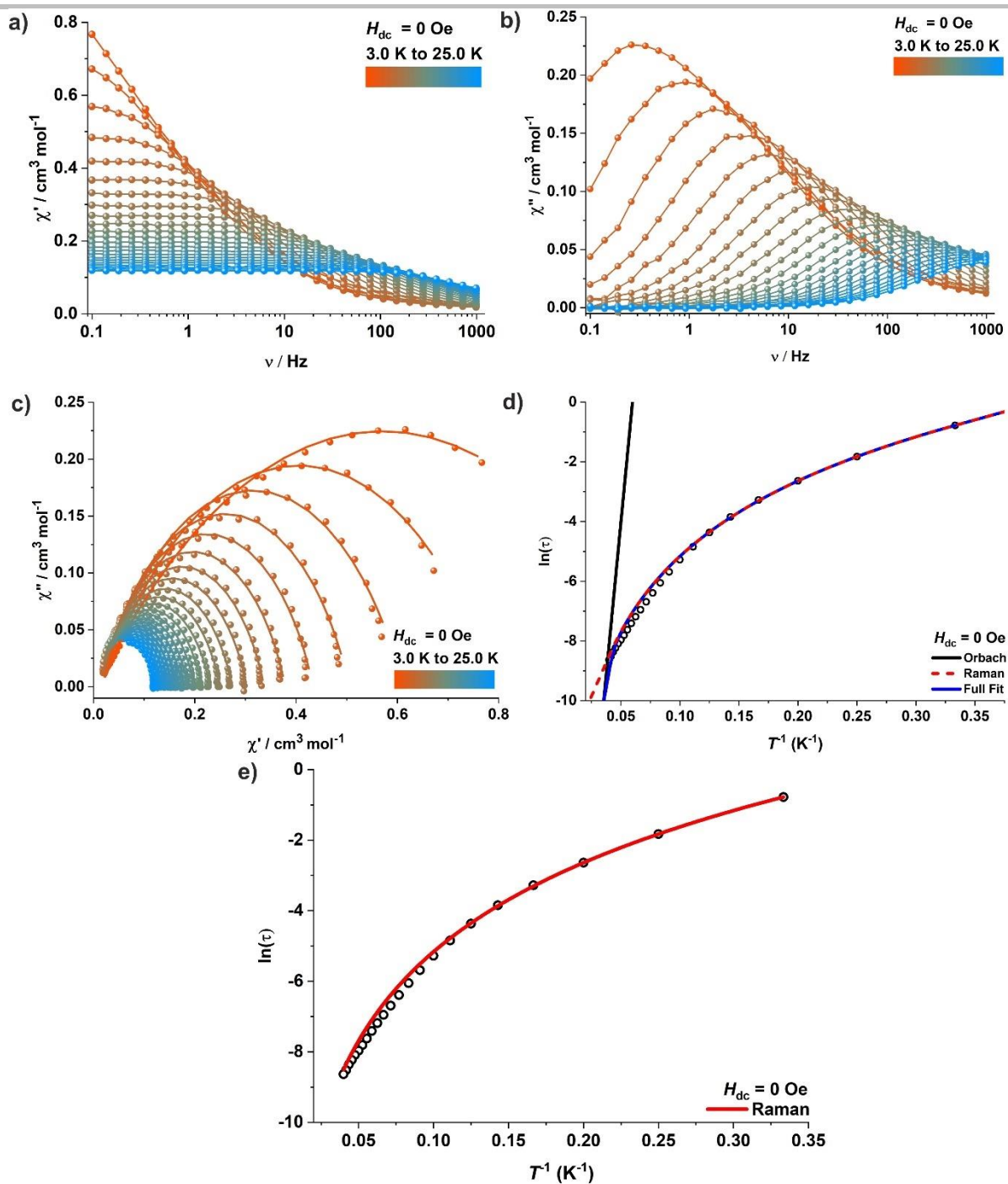
Figure S44. (a) In-phase (χ_M') and (b) out-of-phase (χ_M'') component of the frequency-dependent (0.1–1000 Hz) ac susceptibility measured in an oscillating ac field of 3.0 Oe under zero dc field for complex **1**. (c) Cole-Cole plots for complex **1** under zero field. (d) Dependence of the natural logarithm of the relaxation time $\ln(\tau)$ on inverse temperature (T^{-1}); the solid blue line represents the best fit considering a combination of Orbach (U_{eff} = 410 K, τ_0 = 2.25 × 10^{-11} s) and Raman (C = 0.0399 $s^{-1} K^{-n}$, n = 3.64) relaxation pathways. (e) Dependence of the natural logarithm of the relaxation time $\ln(\tau)$ on inverse temperature (T^{-1}); the solid red line represents the best fit considering only the Raman (C = 0.0319 $s^{-1} K^{-n}$, n = 3.80) relaxation pathway.
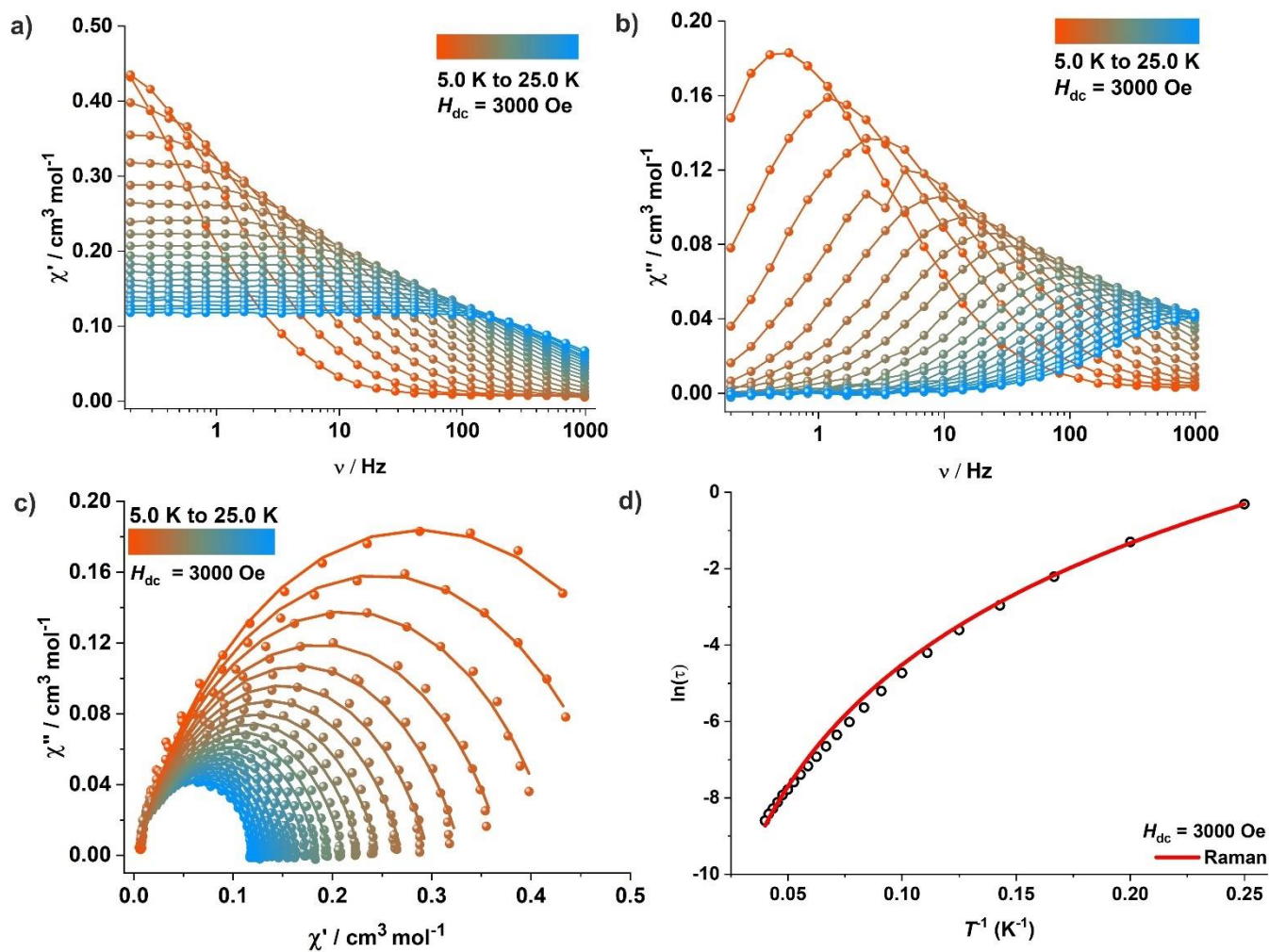
Figure S45. (a) In-phase (χ_M') and (b) out-of-phase (χ_M'') component of the frequency-dependent (0.1–1000 Hz) ac susceptibility measured in an oscillating ac field of 3.0 Oe under an applied dc field of 3000 Oe for complex **1**. (c) Cole-Cole plots for complex **1** under an applied dc field of 3000 Oe. (d) Dependence of the natural logarithm of the relaxation time $\ln(\tau)$ on inverse temperature (T^{-1}); the solid red line represents the best fit considering the Raman (C = 0.0023 s^{-1} K^{-n}, n = 4.59) relaxation pathway.

Figure S46. Variable field magnetization for **1** at a sweep rate of 30 Oe/s at indicated temperatures.

Figure S47. Variable field magnetization for **1** at a sweep rate of 100 Oe/s at indicated temperatures.
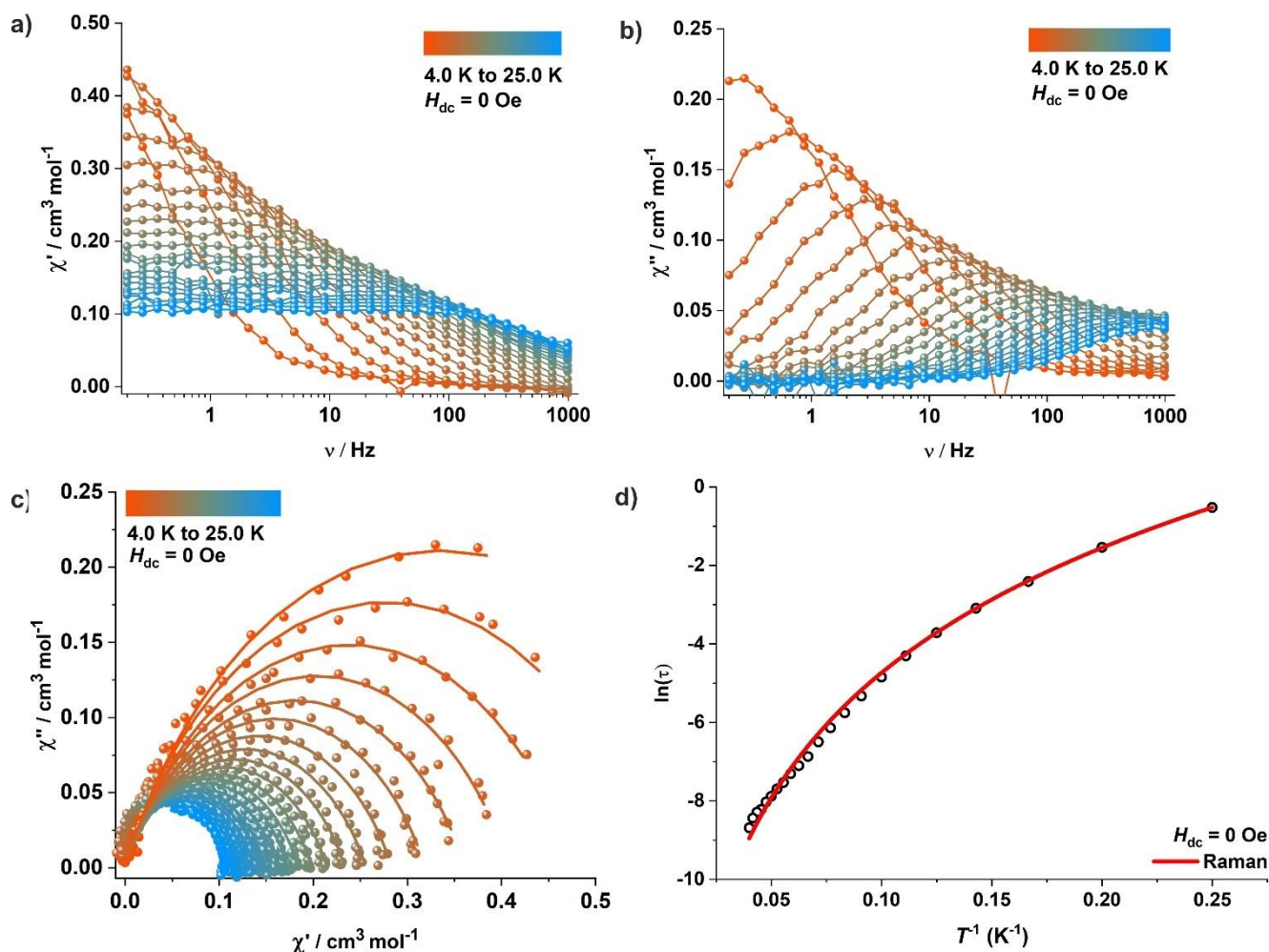
Figure S48. (a) In-phase (χ_M') and (b) out-of-phase (χ_M'') component of the frequency-dependent (0.1–1000 Hz) ac susceptibility measured in an oscillating ac field of 3.0 Oe under zero dc field for complex **1′** (*ca.* 10% **1** in the analogous zinc(II) complex **4**). (c) Cole-Cole plots for complex **1′** under zero dc field. (d) Dependence of the natural logarithm of the relaxation time $\ln(\tau)$ on inverse temperature (T^{-1}); the solid red line represents the best fit considering the Raman (C = 0.0029 s^{-1} K^{-n}, n = 4.60) relaxation pathway.

Figure S49. Comparison of the relaxation time [ln(τ)] *versus* T^{-1} for **1** (at 0 Oe), **1** (at 3000 Oe), and **1′** (at 0 Oe).
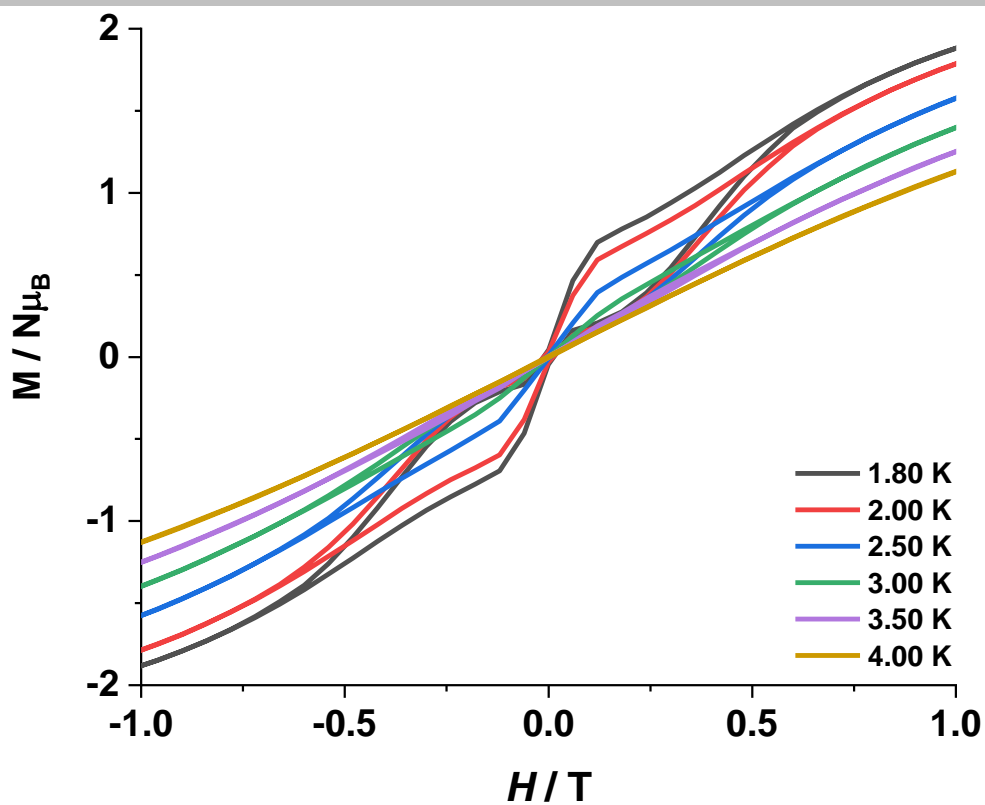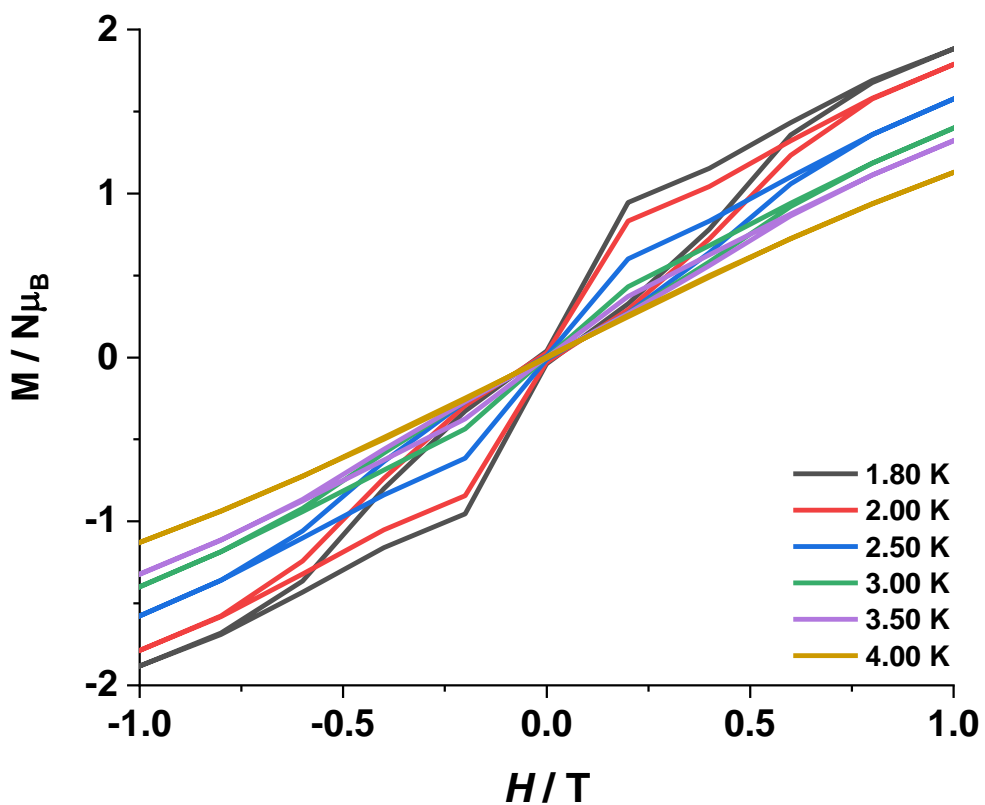

Figure S50. Variable field magnetization for **1′** at a sweep rate of 30 Oe/s at indicated temperatures.

Figure S51. Variable field magnetization for **1′** (*ca.* 10% **1** in the analogous zinc(II) complex **4**) at a sweep rate of 100 Oe/s at indicated temperatures.

Figure S52. Variable field magnetization for **1″** (*ca.* 2% **1** in the analogous zinc(II) complex **4**) at a sweep rate of 30 Oe/s at indicated temperatures.
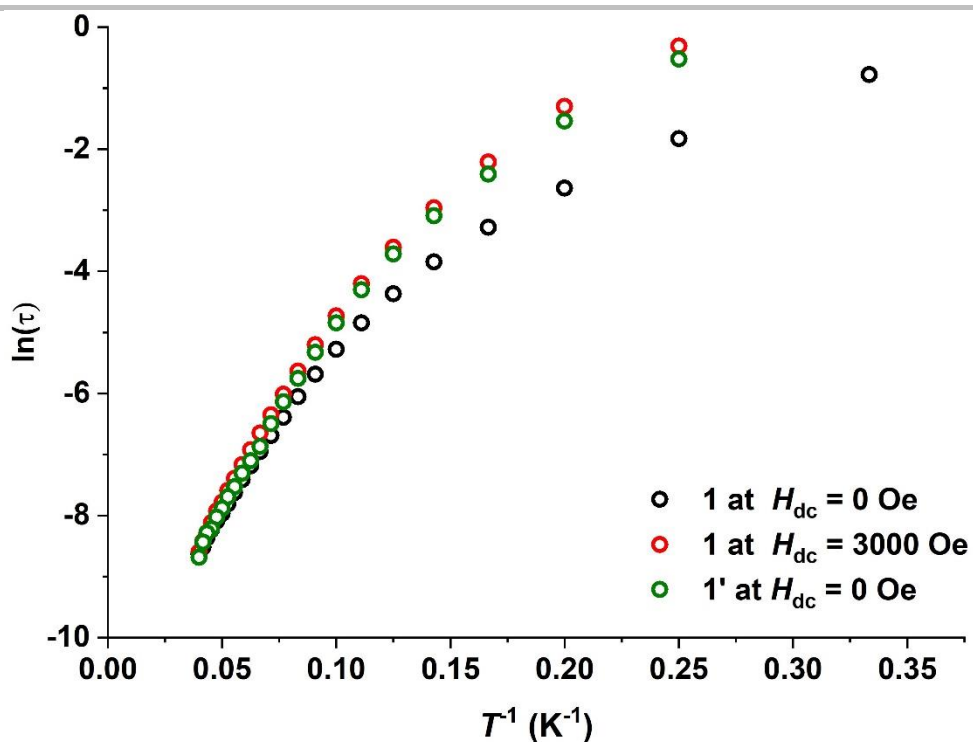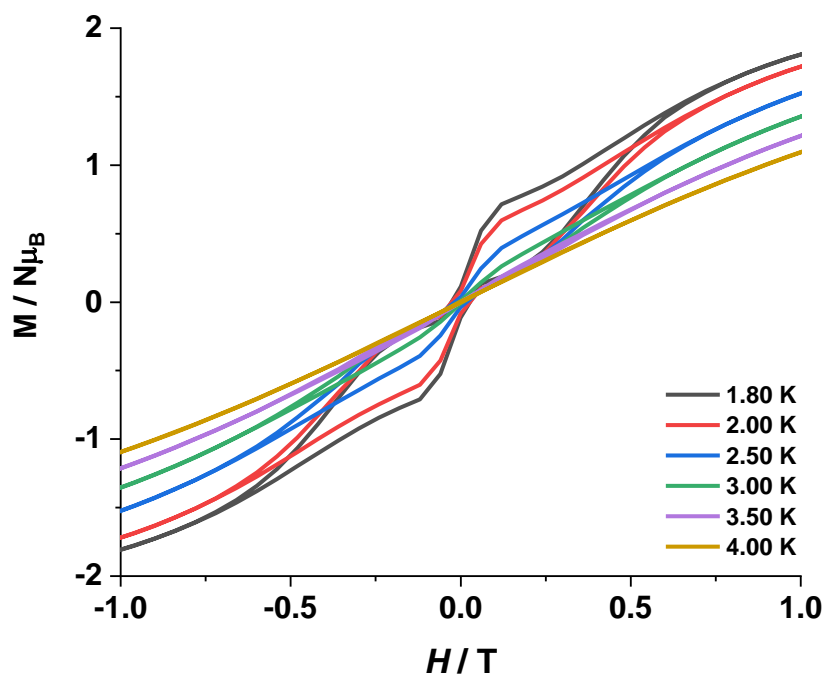
Figure S53. Variable field magnetization for **1″** at a sweep rate of 100 Oe/s at indicated temperatures.

Figure S54. (a) In-phase (χ_M') and (b) out-of-phase (χ_M'') component of the temperature-dependent (0.1– 1000 Hz) ac susceptibility measured in an oscillating ac field of 3.0 Oe under zero dc field for complex **2**.
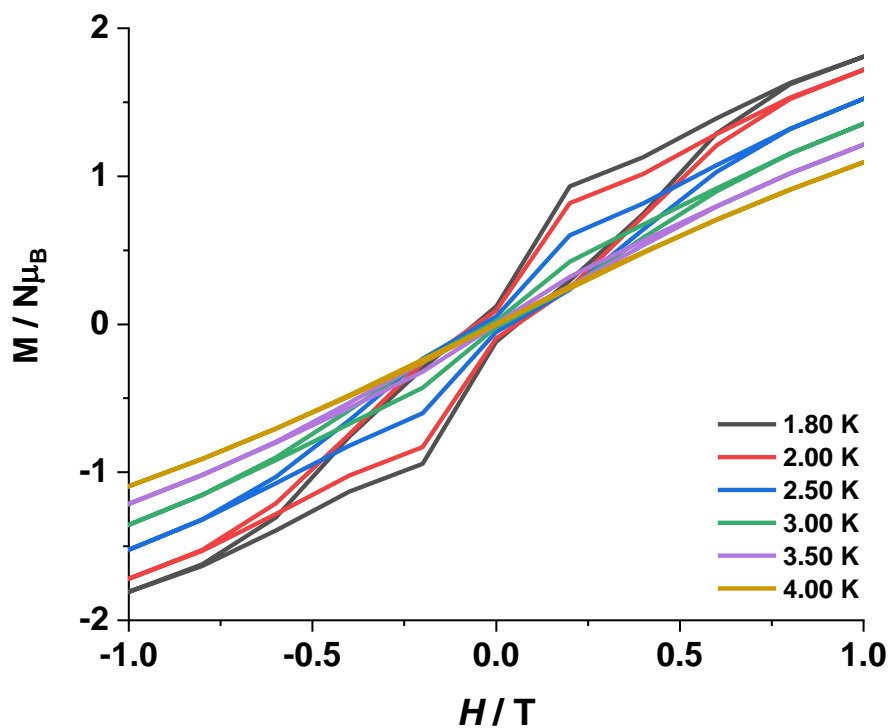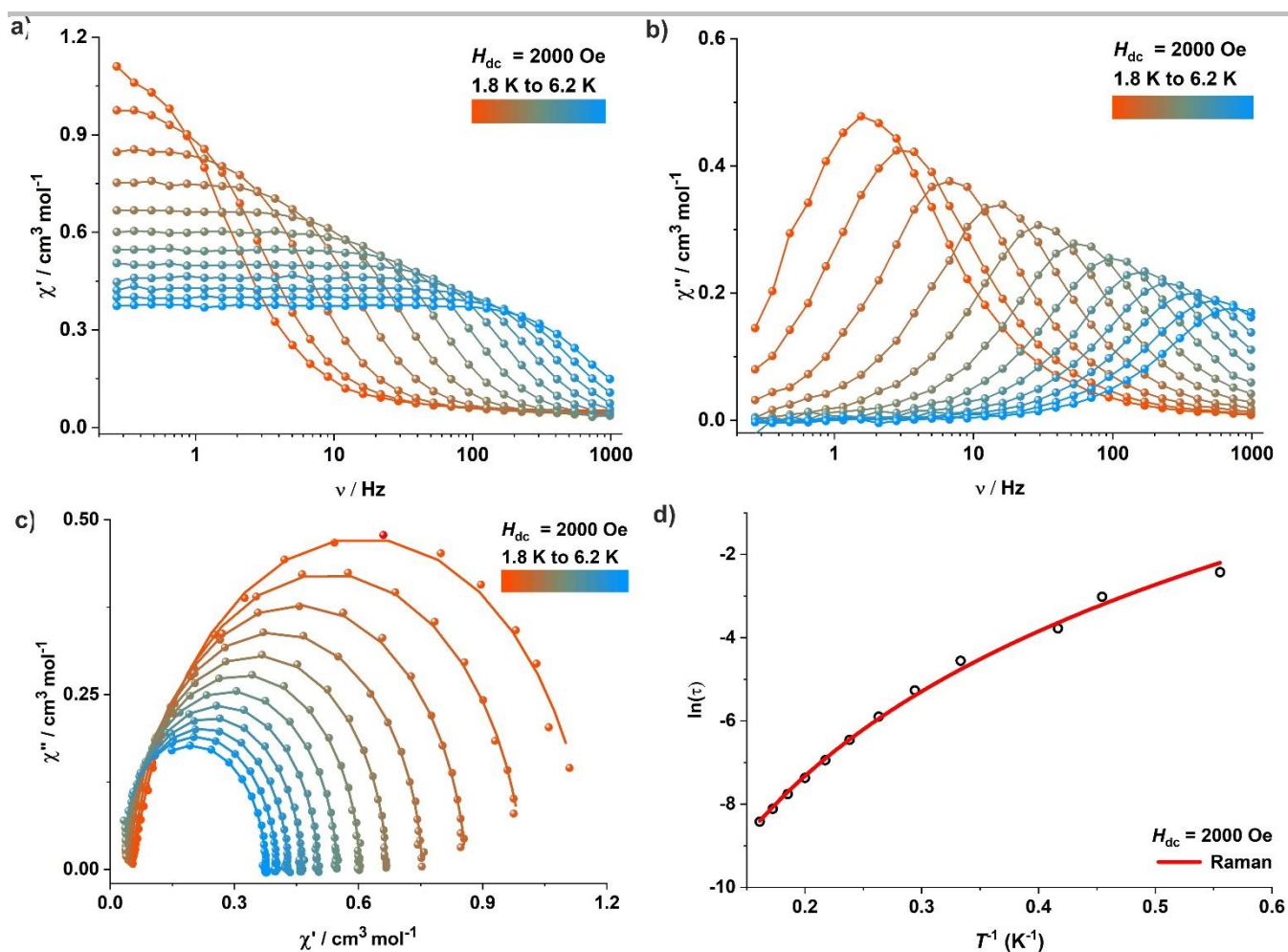
Figure S55. (a) In-phase (χ_M') and (b) out-of-phase (χ_M'') component of the frequency-dependent (0.1–1000 Hz) ac susceptibility measured in an oscillating ac field of 3.0 Oe under an applied dc field of 2000 Oe for complex **2**. (c) Cole-Cole plots for **2** under an applied dc field of 2000 Oe. (d) Dependence of the natural logarithm of the relaxation time $\ln(\tau)$ on inverse temperature (T^{-1}); the solid red line represents the best fit considering the Raman (C = 0.473 $s^{-1}\,K^{-n}$, n = 5.02) relaxation pathway.

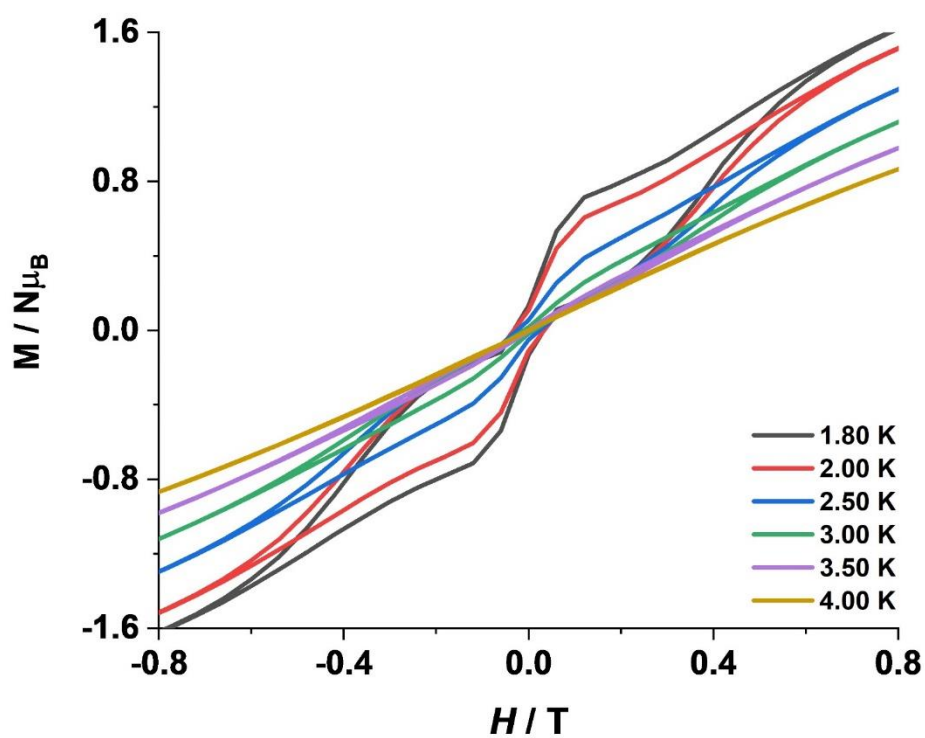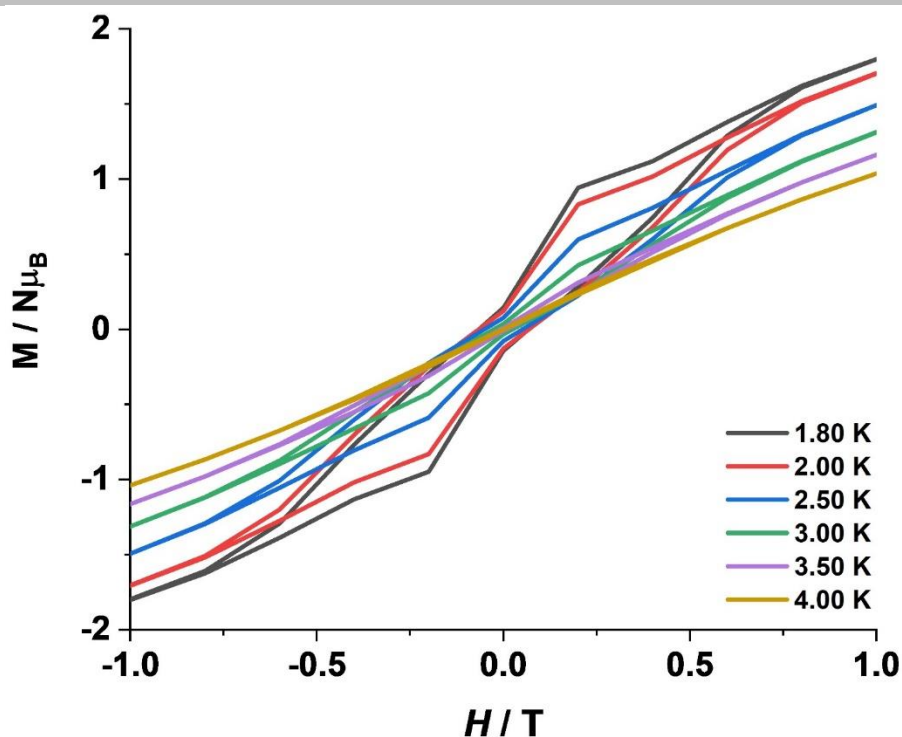**Figure S56**. (a) In-phase (χ_M') and (b) out-of-phase (χ_M'') component of the temperature-dependent (0.1–1000 Hz) ac susceptibility measured in an oscillating ac field of 3.0 Oe under zero dc field for complex **3**.

Figure S57. (a) In-phase (χ_M') and (b) out-of-phase (χ_M'') component of the frequency-dependent (0.1–1000 Hz) ac susceptibility measured in an oscillating ac field of 3.0 Oe under an applied dc field of 3000 Oe for complex **3**. (c) Cole-Cole plots for **3** under an applied dc field of 3000 Oe. (d) Dependence of the natural logarithm of the relaxation time $\ln(\tau)$ on inverse temperature (T^{-1}); the solid blue line represents the best fit considering a combination of Raman (C = 16.64 s^{-1} K^{-n}, n = 3.23) and QTM (τ_{QTM} = 2.0 x 10^{-3} s) relaxation pathways.
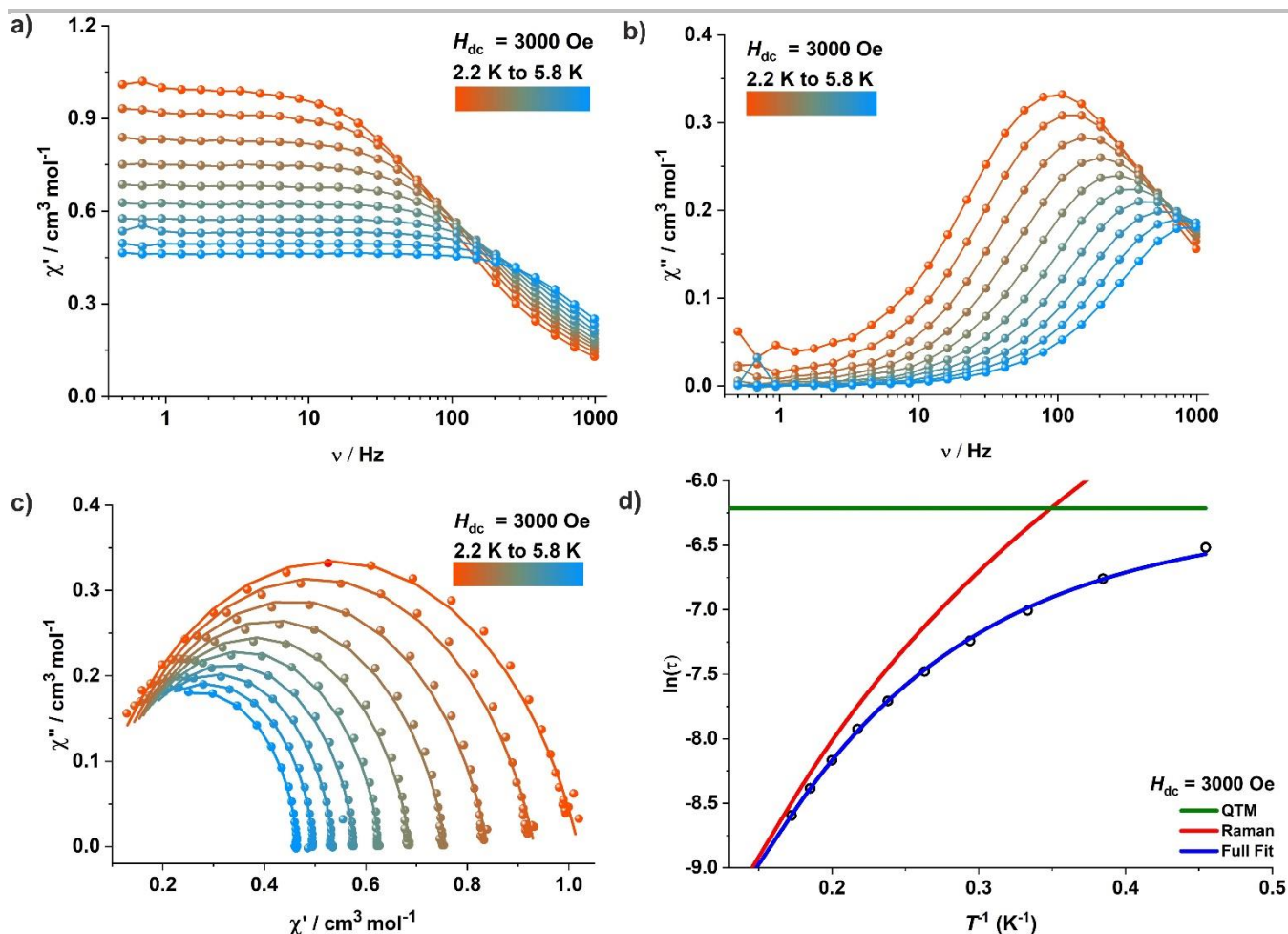
Figure S58. (a) In-phase (χ_M') and (b) out-of-phase (χ_M'') component of the frequency-dependent (0.1–1000 Hz) ac susceptibility measured in an oscillating ac field of 3.0 Oe under zero dc field for complex **2′** (*ca.* 10% **2** in the analogous zinc(II) complex **5**). (c) Cole-Cole plots for **2′** under zero dc field. (d) Dependence of the natural logarithm of the relaxation time $\ln(\tau)$ on inverse temperature (T^{-1}); the solid blue line represents the best fit considering a combination of Raman (C = 0.135 $s^{-1}\,K^{-n}$, n = 5.86) and QTM (τ_{QTM} = 8.70 x 10^{-4} s) relaxation pathways.
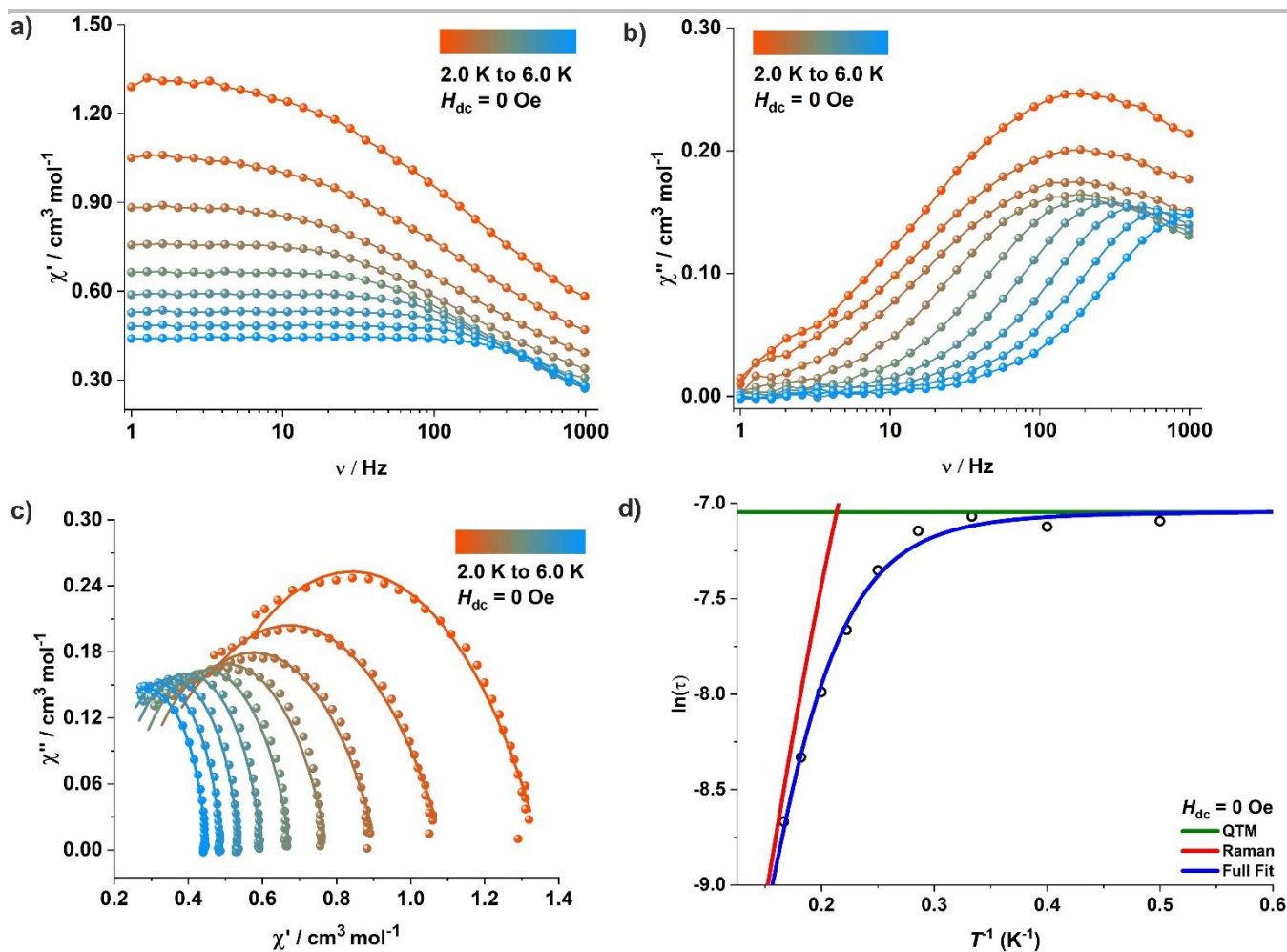
Figure S59. (a) In-phase (χ_M') and (b) out-of-phase (χ_M'') component of the frequency-dependent (0.1–1000 Hz) ac susceptibility measured in an oscillating ac field of 3.0 Oe under an applied dc field of 2000 Oe for complex **2′**. (c) Cole-Cole plots for **2′** under an applied dc field of 2000 Oe. (d) Dependence of the natural logarithm of the relaxation time ln(τ) on inverse temperature (T^{-1}); the solid red line represents the best fit considering the Raman (C = 0.156 s^{-1} K^{-n}, n = 5.63) relaxation pathway.

Figure S60. Variable field magnetization for **2″** (*ca.* 2% **2** in the analogous zinc(II) complex **5**) at a sweep rate of 100 Oe/s at 1.8 K.
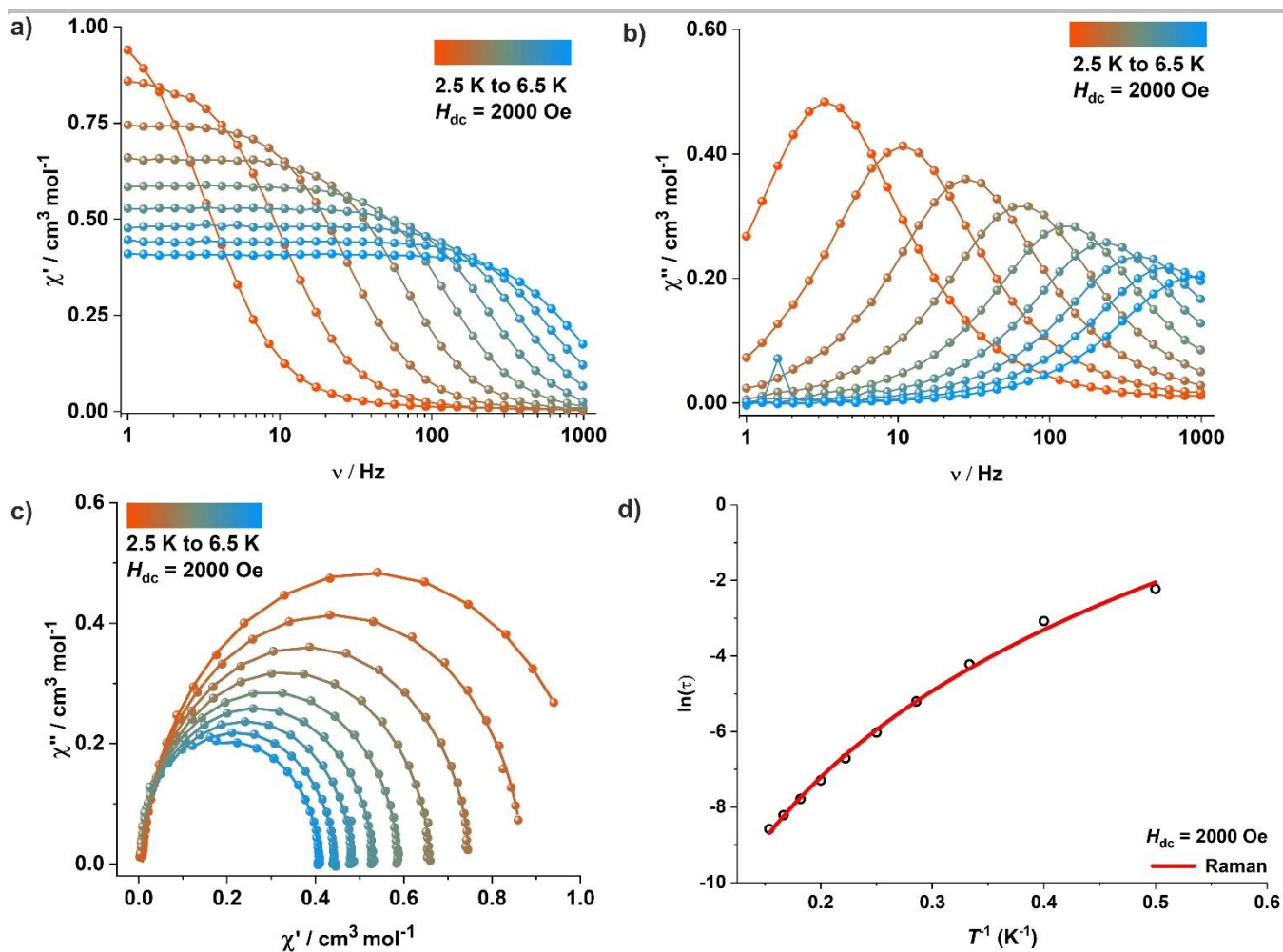
Figure S61. (a) In-phase ($\chi_M{}'$) and (b) out-of-phase ($\chi_M{}''$) component of the frequency-dependent (0.1–1000 Hz) ac susceptibility measured in an oscillating ac field of 3.0 Oe under zero dc field for complex **3′** (*ca.* 10% **3** in the analogous zinc(II) complex **6**). (c) Cole-Cole plots for **3′** under zero dc field. (d) Dependence of the natural logarithm of the relaxation time $\ln(\tau)$ on inverse temperature (T^{-1}); the solid blue line represents the best fit considering a combination of Raman (C = 0.275 $s^{-1}K^{-n}$, n = 4.77) and QTM (τ_{QTM} = 1.83 x 10^{-3} s) relaxation pathways.
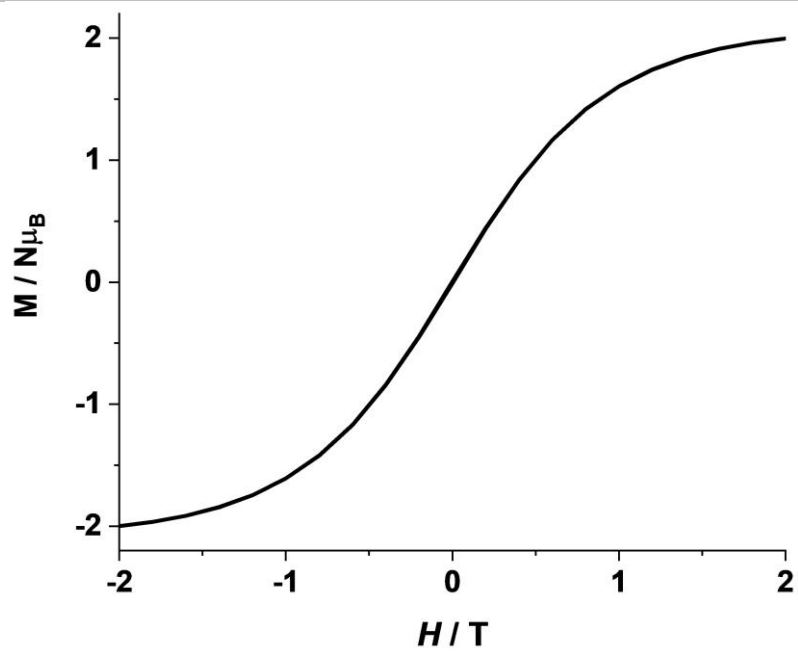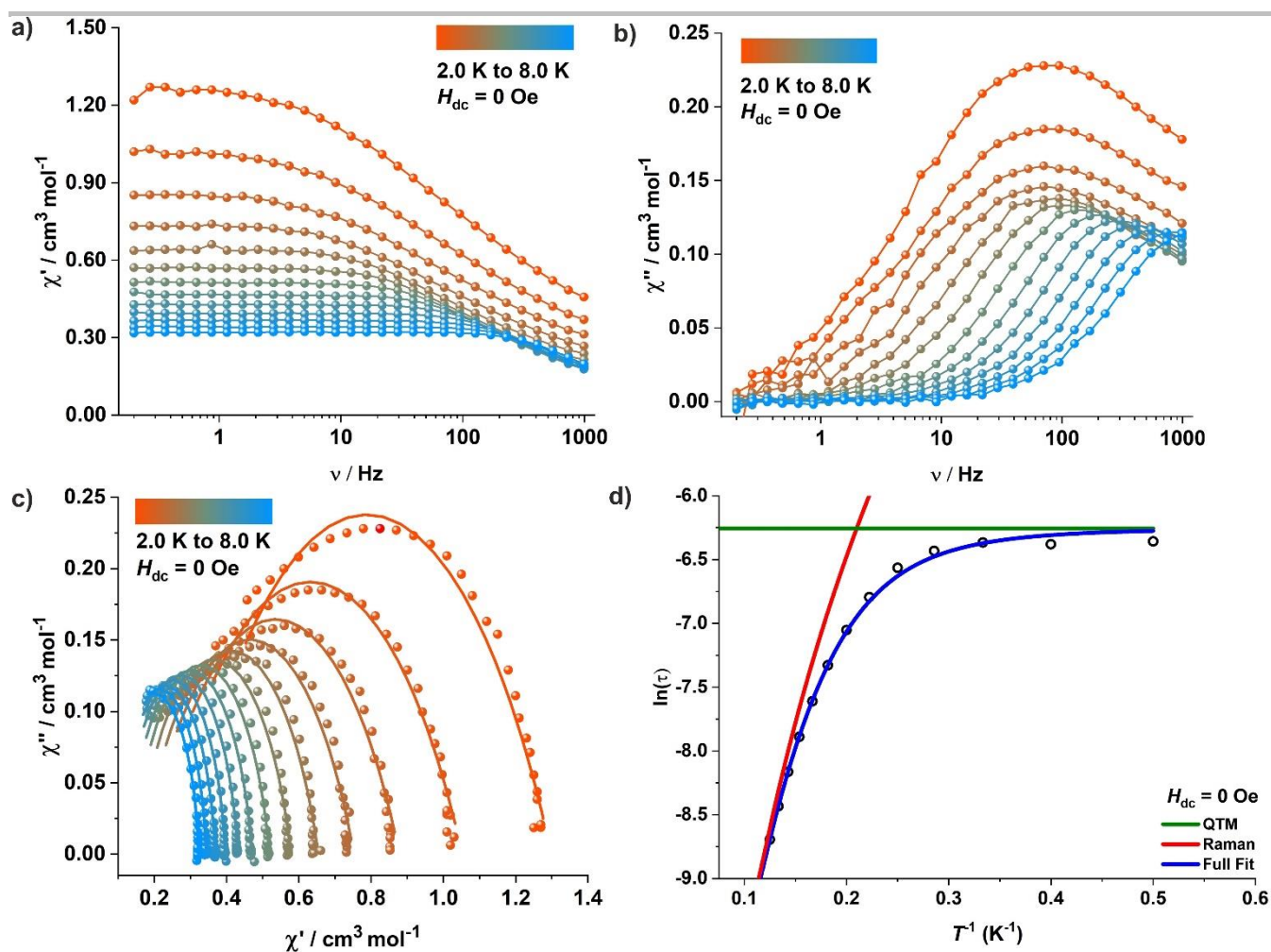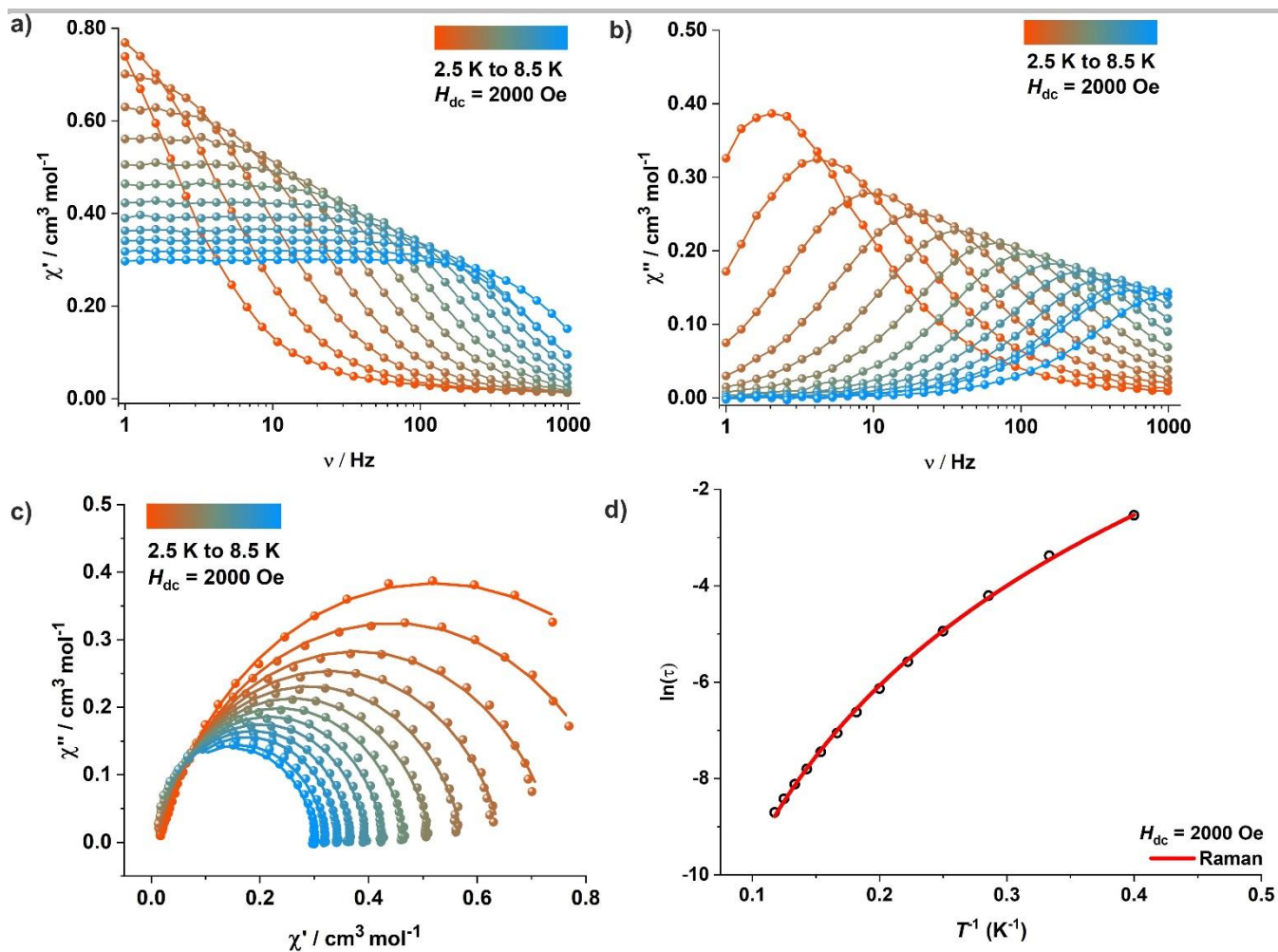
Figure S62. (a) In-phase (χ_M') and (b) out-of-phase (χ_M'') component of the frequency-dependent (0.1–1000 Hz) ac susceptibility measured in an oscillating ac field of 3.0 Oe under an applied dc field of 2000 Oe for complex **3'**. (c) Cole–Cole plots for **3'** under an applied dc field of 2000 Oe. (d) Dependence of the natural logarithm of the relaxation time ln(τ) on inverse temperature (T^{-1}); the solid red line represents the best fit considering the Raman (C = 0.117 $s^{-1}K^{-n}$, n = 5.411) relaxation pathway.

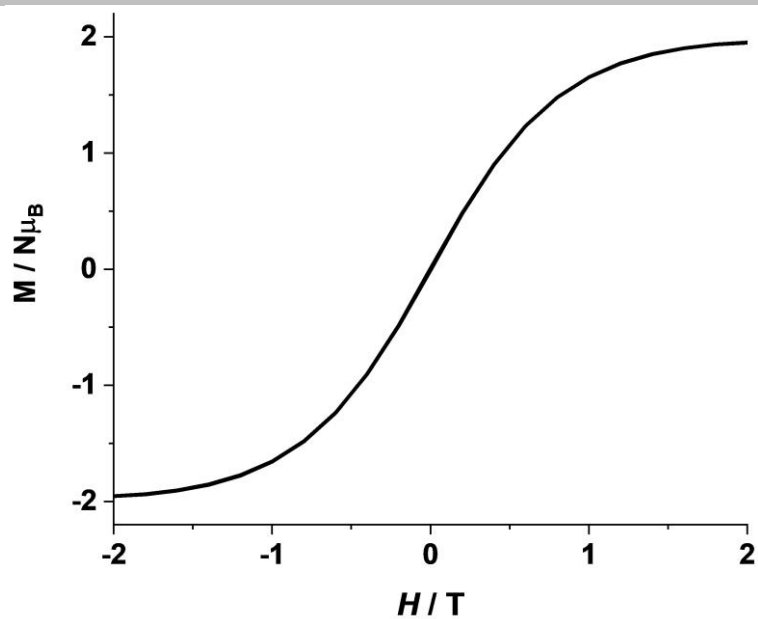**Figure S63**. Variable field magnetization for **3″** (*ca.* 2% **3** in the analogous zinc(II) complex **6**) at a sweep rate of 100 Oe/s at 1.8 K.

Figure S64. Variable-temperature χ_MT product for a frozen DMF solution of complex **1** measured under an applied dc field of 0.5 T.

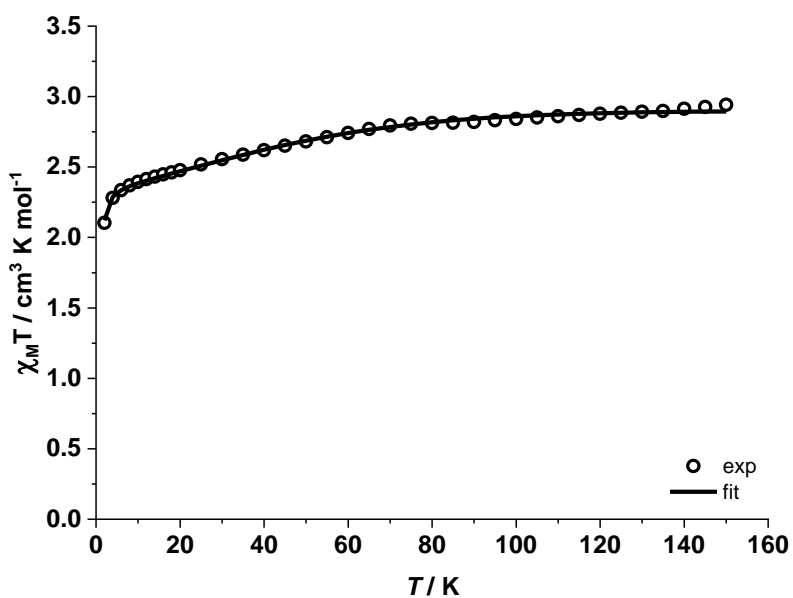**Figure S65**. Variable-temperature variable-field magnetization for a frozen DMF solution of complex **1**.
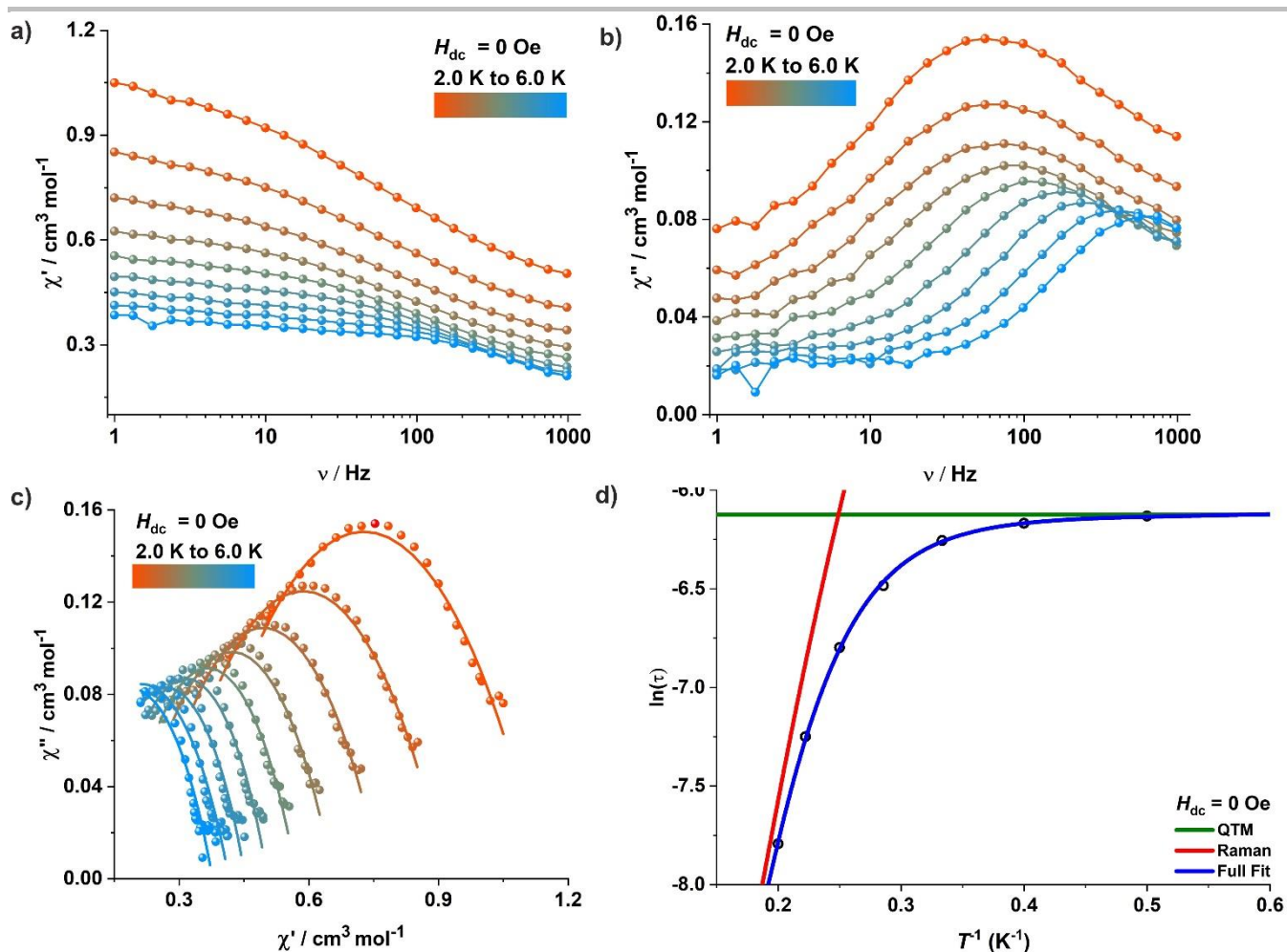
Figure S66. (a) In-phase (χ_M') and (b) out-of-phase (χ_M'') component of the frequency-dependent (0.1–1000 Hz) ac susceptibility measured in an oscillating ac field of 3.0 Oe under zero dc field for a frozen DMF solution of complex **1**. (c) Cole-Cole plots for a frozen DMF solution of complex **1** under zero dc field. (d) Dependence of the natural logarithm of the relaxation time $\ln(\tau)$ on inverse temperature (T^{-1}); the solid blue line represents the best fit considering a combination of Raman (C = 0.047 $s^{-1} K^{-n}$, n = 6.61) and QTM (τ_{QTM} = 2.19 x 10^{-3} s) relaxation pathways.
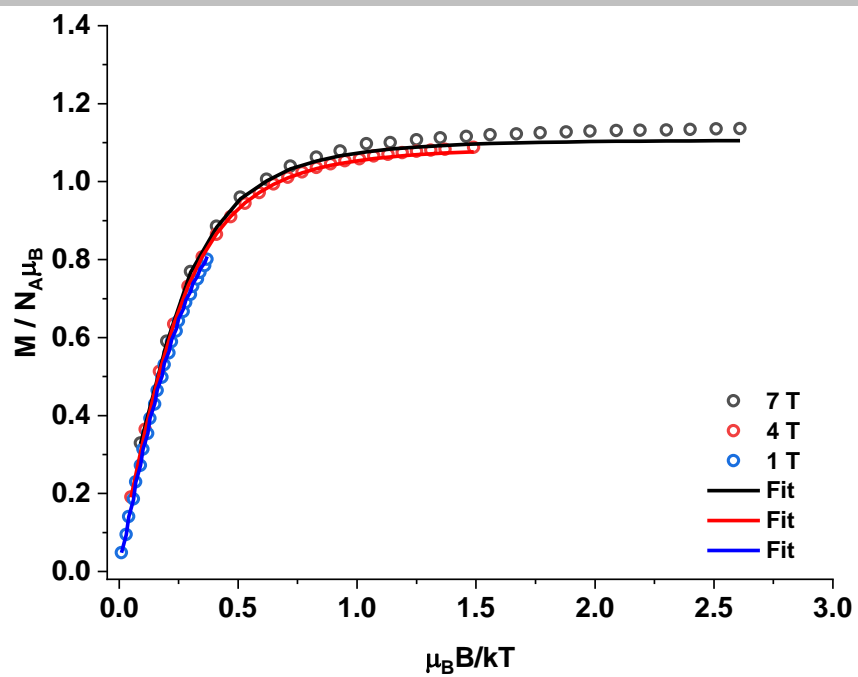
Figure S67. (a) In-phase (χ_M') and (b) out-of-phase (χ_M'') component of the frequency-dependent (0.1–1000 Hz) ac susceptibility measured in an oscillating ac field of 3.0 Oe under an applied dc field of 2000 Oe for a frozen DMF solution of complex **1**. (c) Cole-Cole plots for a frozen DMF solution of complex **1** under an applied dc field of 2000 Oe. (d) Dependence of the natural logarithm of the relaxation time $\ln(\tau)$ on inverse temperature (T^{-1}); the solid blue line represents the best fit considering a comination of Raman (C = 0.165 s^{-1} K^{-n}, n = 5.47) and QTM (τ_{QTM} = 9.93 x 10^{-2} s) relaxation pathways.

Figure S68. Variable field magnetization for a frozen DMF solution of complex **1** at a sweep rate of 100 Oe/s at 1.8 K.


Figure S69. Variable-temperature χ_MT product for a frozen DMF solution of complex **2** measured under an applied dc field of 0.5 T.
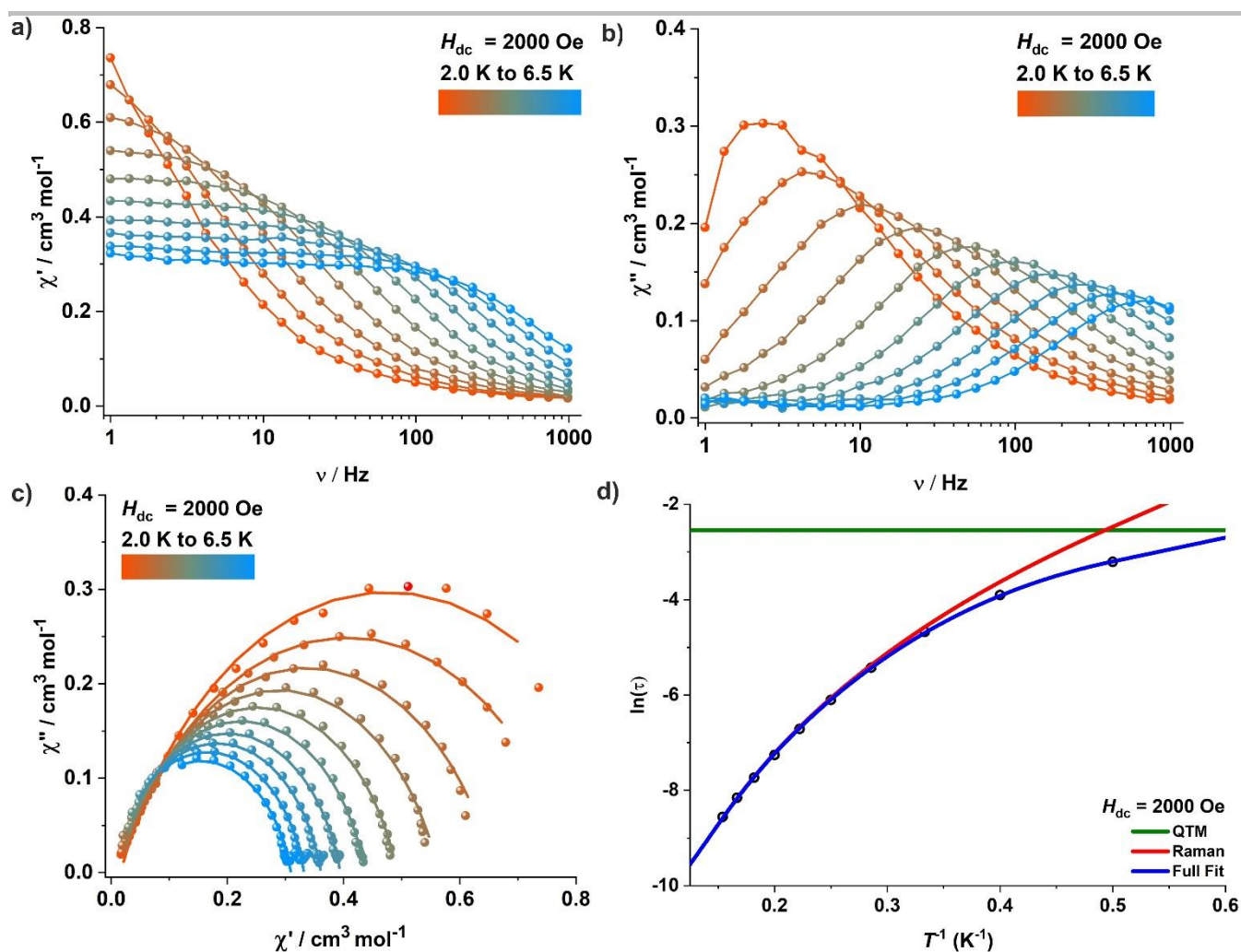
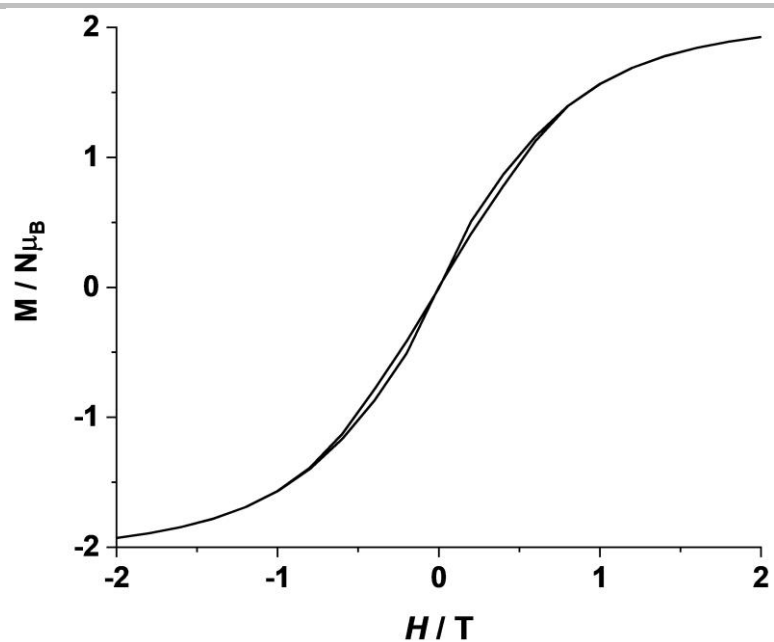**Figure S70**. Variable-temperature variable-field magnetization for a frozen DMF solution of complex **2**.
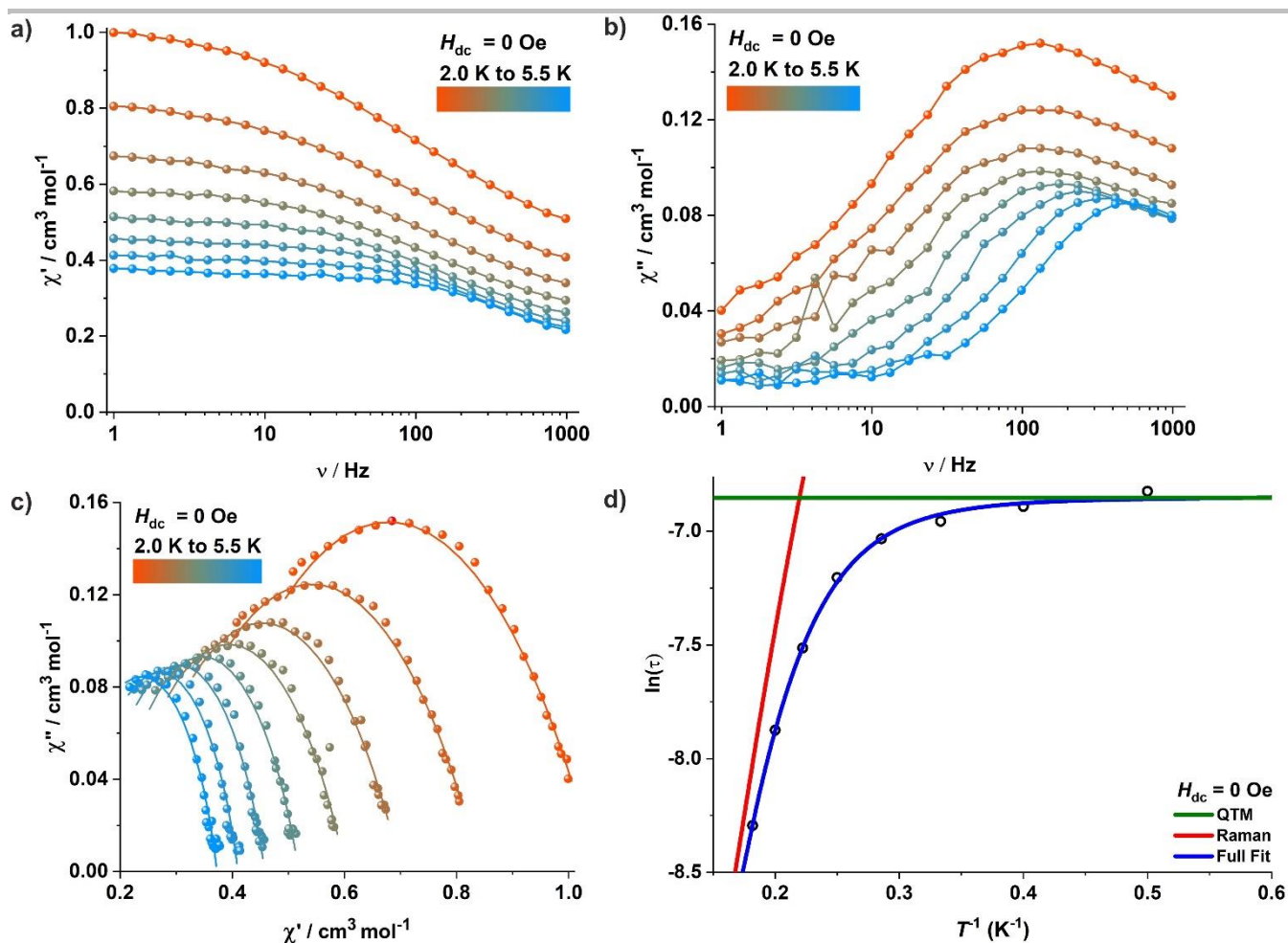
Figure S71. (a) In-phase (χ_M') and (b) out-of-phase (χ_M'') component of the frequency-dependent (0.1–1000 Hz) ac susceptibility measured in an oscillating ac field of 3.0 Oe under zero dc field for a frozen DMF solution of complex **2**. (c) Cole-Cole plots for a frozen DMF solution of complex **2** under zero dc field. (d) Dependence of the natural logarithm of the relaxation time $\ln(\tau)$ on inverse temperature (T^{-1}); the solid blue line represents the best fit considering a combination of Raman (C = 0.079 $s^{-1}\,K^{-n}$, n = 6.19) and QTM (τ_{QTM} = 1.06 x 10^{-3} s) relaxation pathways.
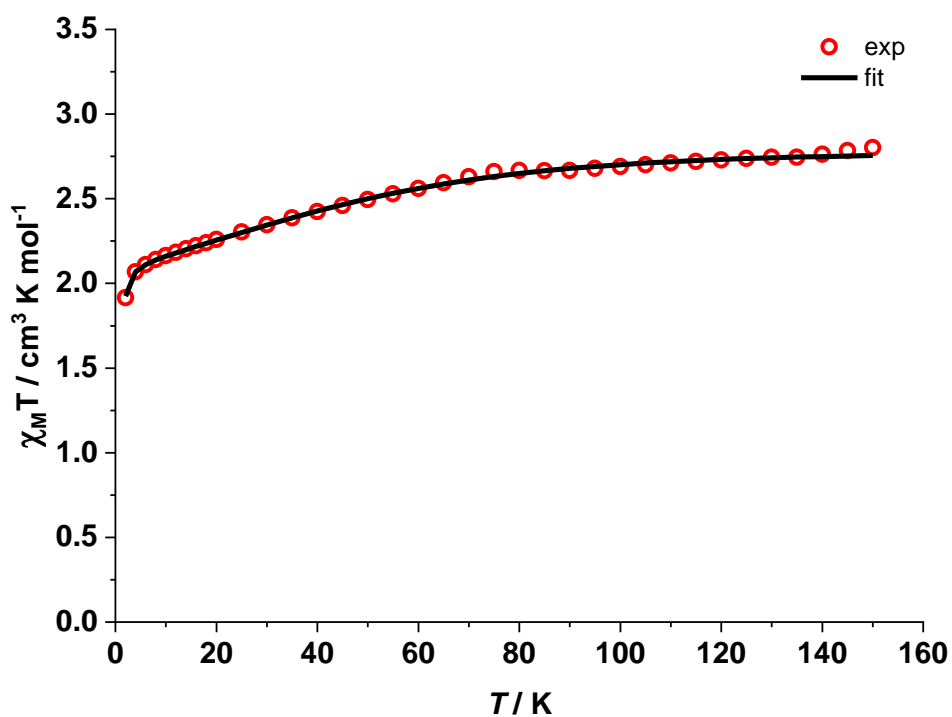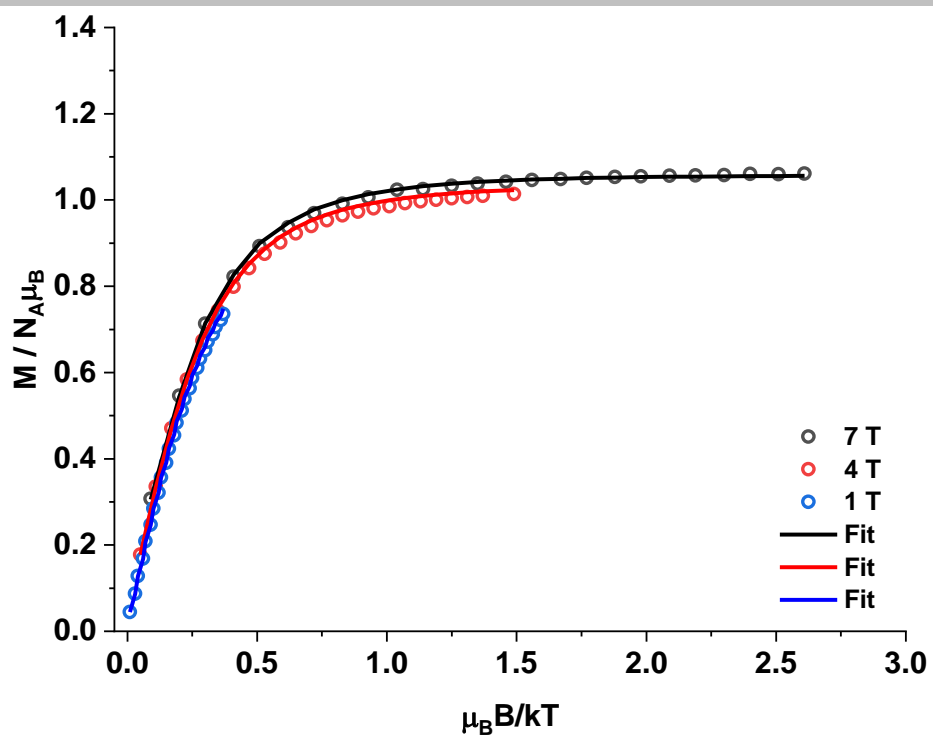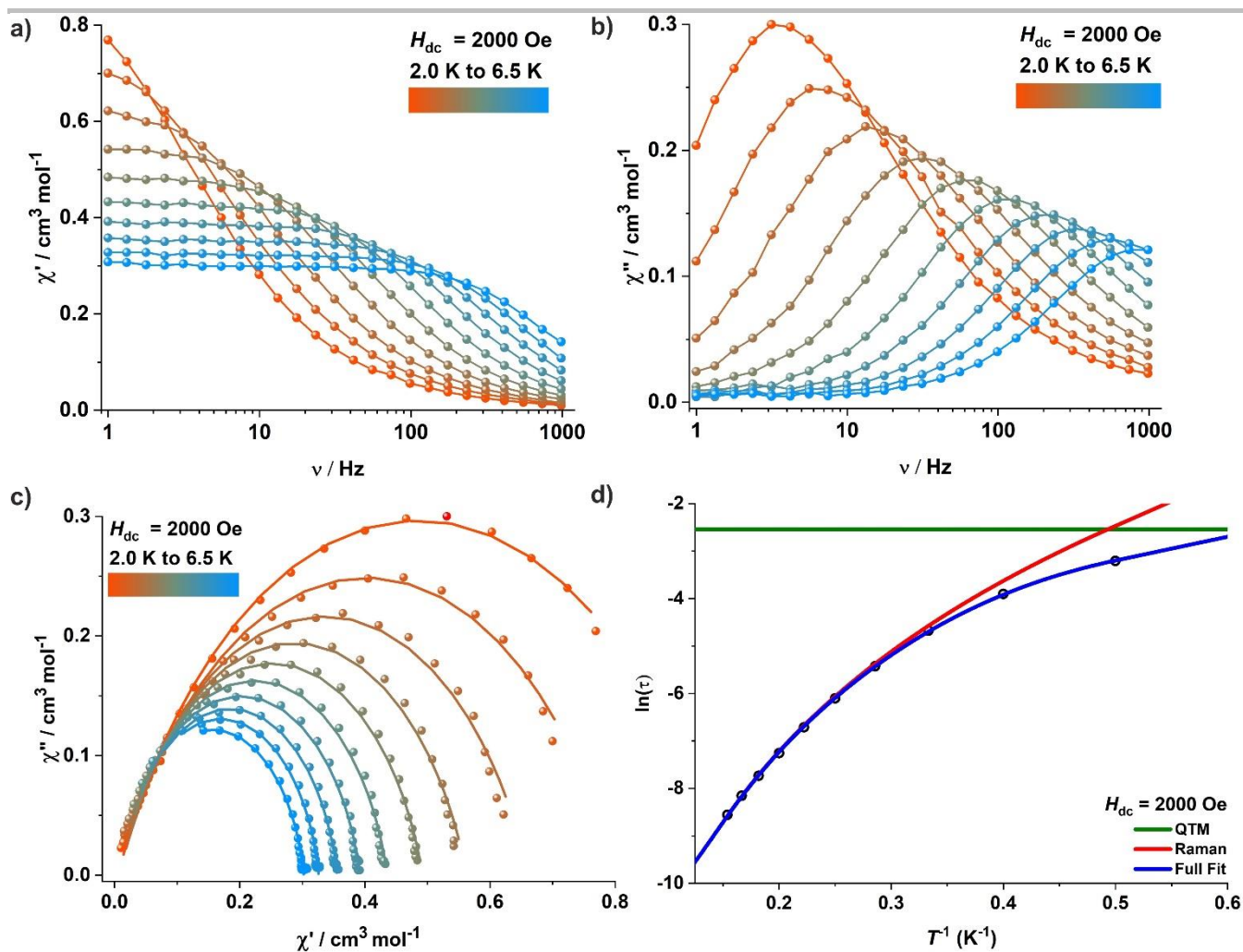
Figure S72. (a) In-phase (χ_M') and (b) out-of-phase (χ_M'') component of the frequency-dependent (0.1–1000 Hz) ac susceptibility measured in an oscillating ac field of 3.0 Oe under an applied dc field of 2000 Oe for a frozen DMF solution of complex **2**. (c) Cole-Cole plots for a frozen DMF solution of complex **2** under an applied dc field of 2000 Oe. (d) Dependence of the natural logarithm of the relaxation time $\ln(\tau)$ on inverse temperature (T^{-1}); the solid blue line represents the best fit considering a combination of Raman (C = 0.325 s^{-1} K^{-n}, n = 5.18) and QTM (τ_{QTM} = 7.88 x 10^{-2} s) relaxation pathways.
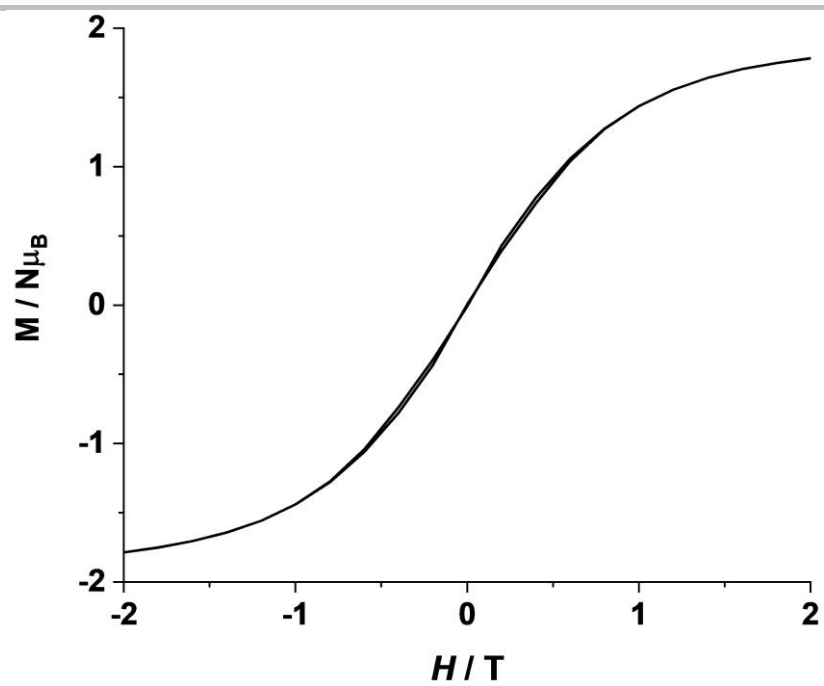
Figure S73. Variable field magnetization for a frozen DMF solution of complex **2** at a sweep rate of 100 Oe/s at 1.8 K.

5. Computational Studies

Table S7. Composition of ab-initio ligand field orbitals for all structures obtained at the NEVPT2 level

		d_{z2}	d_{xz}	d_{yz}	d_{x2-y2}	d_{xy}			d_{z2}	d_{xz}	d_{yz}	d_{x2-y2}	d_{xy}
1a	**1**	0.22	0.00	0.00	0.78	0.00	**2a**	**1**	0.00	0.75	0.11	0.00	0.14
	2	0.78	0.00	0.00	0.22	0.00		**2**	0.14	0.11	0.15	0.51	0.09
	3	0.00	1.00	0.00	0.00	0.00		**3**	0.11	0.01	0.39	0.03	0.47
	4	0.00	0.00	0.03	0.00	0.97		**4**	0.12	0.13	0.28	0.24	0.24
	5	0.00	0.00	0.97	0.00	0.03		**5**	0.63	0.00	0.08	0.23	0.06
1b	**1**	0.26	0.00	0.00	0.74	0.00	**2b**	**1**	0.00	0.92	0.03	0.00	0.05
	2	0.74	0.00	0.00	0.26	0.00		**2**	0.07	0.03	0.20	0.64	0.06
	3	0.00	1.00	0.00	0.00	0.00		**3**	0.14	0.00	0.36	0.00	0.49
	4	0.00	0.00	0.99	0.00	0.01		**4**	0.09	0.04	0.30	0.19	0.37
	5	0.00	0.00	0.01	0.00	0.99		**5**	0.70	0.00	0.11	0.16	0.03
1c	**1**	0.32	0.00	0.00	0.67	0.00	**3**	**1**	0.37	0.02	0.00	0.61	0.00
	2	0.61	0.08	0.00	0.31	0.00		**2**	0.61	0.00	0.00	0.39	0.00
	3	0.06	0.92	0.00	0.01	0.00		**3**	0.00	0.00	0.99	0.00	0.01
	4	0.00	0.00	0.98	0.00	0.02		**4**	0.00	0.00	0.01	0.00	0.99
	5	0.00	0.00	0.02	0.00	0.98		**5**	0.02	0.97	0.00	0.01	0.00
1d	**1**	0.29	0.01	0.00	0.70	0.00							
	2	0.46	0.28	0.00	0.26	0.00							
	3	0.25	0.71	0.00	0.04	0.00							
	4	0.00	0.00	0.94	0.00	0.06							
	5	0.00	0.00	0.06	0.00	0.94							

5.1 Code Sample. Sample AOMX input for structure **1a**:

```
7

VAR OPT
esig = 6000
epis = 4000
*
epic = 0
epis' = 0
pic/2pis0 = 0.6
epis0 = epis / 2 + epis' / 2
episdiff = epis - epis'
A = 186773.7
B = 948.6
C = 3759.8
zeta = 505.5

XYZ
-0.8747 -1.4942 -0.9757
-0.9414 1.4885 0.8990
0.8747 -1.4942 0.9757
0.9415 1.4885 -0.8990

AOM
esig epis0 epic
esig epis0 epic
esig epis0 epic
esig epis0 epic

CON
1 3
2 4

VEE 0 B C

HSO zeta

EXP
state2 0.000000 1 2 1
state4 299.460000 1 2 2
state6 645.680000 1 2 3
state8 999.380000 1 2 4
state10 8910.840000 1 2 5
state12 9114.310000 1 2 6
state14 9266.630000 1 2 7
state16 9491.590000 1 2 8
state18 9650.460000 1 2 9
state20 9863.890000 1 2 10

RUN
```

5.2 Computational Methods

The splitting of the terms due to spin-orbit coupling is computed using the principle of the Breit-Pauli operator[5]. This consists of one and two-electron parts.

$$\hat{H}_{SO} = \frac{\alpha^2}{2} \sum_A \sum_i \frac{Z_A}{|\vec{R}_A - \vec{r}_i|^3} \hat{\vec{l}}_i^A \hat{\vec{s}}_i - \frac{\alpha^2}{2} \sum_i \hat{\vec{s}}_i \sum_{i \neq j} \frac{1}{|\vec{r}_i - \vec{r}_j|^3} (\hat{\vec{l}}_i^j + \hat{\vec{l}}_i^i) \quad ...(1)$$

where α is the fine structure constant, $\hat{\vec{l}}_i^A = (\vec{r}_i - \vec{R}_A) \times \vec{p}_i$ is the angular momentum for the electron i at position r_i with respect to nucleus A of charge Z_A at position R_A and $\hat{\vec{l}}_j^i = (\vec{r}_i - \vec{r}_j) \times \vec{p}_i$ is the angular momentum of the electron i with respect to electron j. The one- and two-electron integrals are computed using a mean-field approximation (SOMF)[6].

The magnetic susceptibilities are then computed on the basis of the CASSCF/NEVPT2 wavefunctions using the 50 computed states. The Zeeman and spin-orbit matrix elements are given by[7]:

$$\langle \Psi_I^{SM_S} | \hat{H}_{BO} + \hat{H}_{SOC} + \hat{H}_Z | \Psi_J^{S'M'_S} \rangle = \delta_{IJ} \delta_{SS} \delta_{M_S M'_S} E_I^S$$
$$+ \langle \Psi_I^{SM_S} | \hat{H}_{SOC} + \beta \vec{B} (\hat{\vec{L}} + g_e \hat{\vec{S}}) | \Psi_J^{S'M'_S} \rangle \quad .....(2)$$

Where the he $\hat{H}_{BO}$ is the Born-Oppenheimer Hamiltonian, $\hat{H}_{SOC}$ is the Spin-Orbit coupling hamiltonian and $\hat{H}_Z$ is the zeeman operator, E_I^S is the energy of the wavefunction with spin S and index I, g_e is the gyromagnetic ratio of the electron and β is the bohr magneton. The magnetization and magnetic susceptibilities of a state i can be calculated by taking computing the first and second derivatives of energy along a fixed direction α. These are computed numerically by taking finite differences.

From perturbation theory the D value can be expressed as the following (tetrahedral point group):

$$D_1 = -\frac{4}{9} \zeta_{eff}^2 \left[\frac{1}{E(^4B_2)} \right] \quad ......(3)$$

where ζ_{eff}^2 is the effective SOC constant and the $E(^4B_2)$ corresponds to the energy of the $^4B_1 \rightarrow {}^4B_2$ transition and D_1 is the contribution to the D value from the first excited scalar relativistic state. However, the perturbation theory expressions become qualitative when the energy of the $^4B_2$ state is much lower than the ζ_{eff}.

5.3 Contribution to *D* and *E* across compounds using perturbation theory
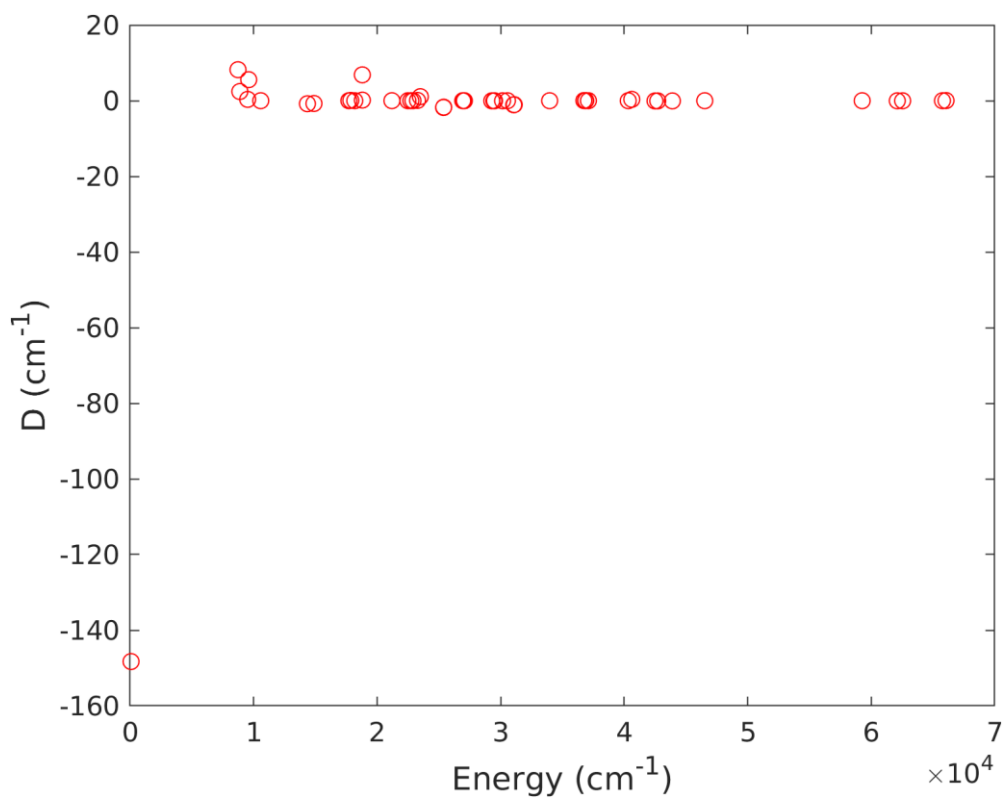
Figure S74. Contributions to *D* from various excited states for compound **1a**.
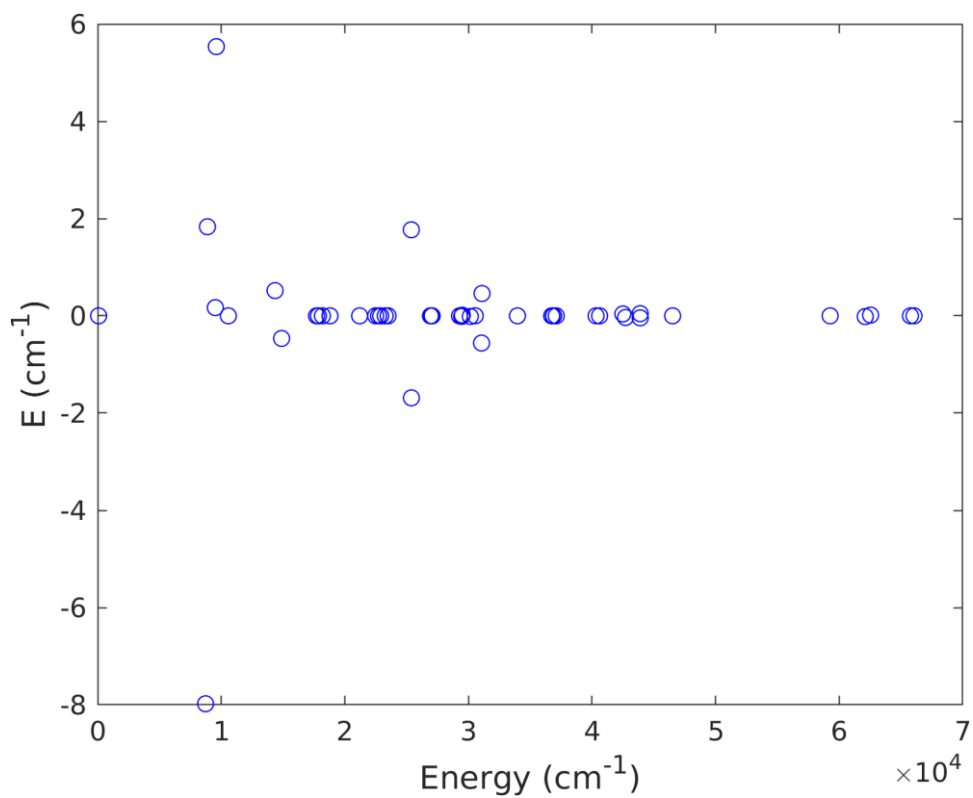
Figure S75. Contributions to *E* from various excited states for compound **1a**.
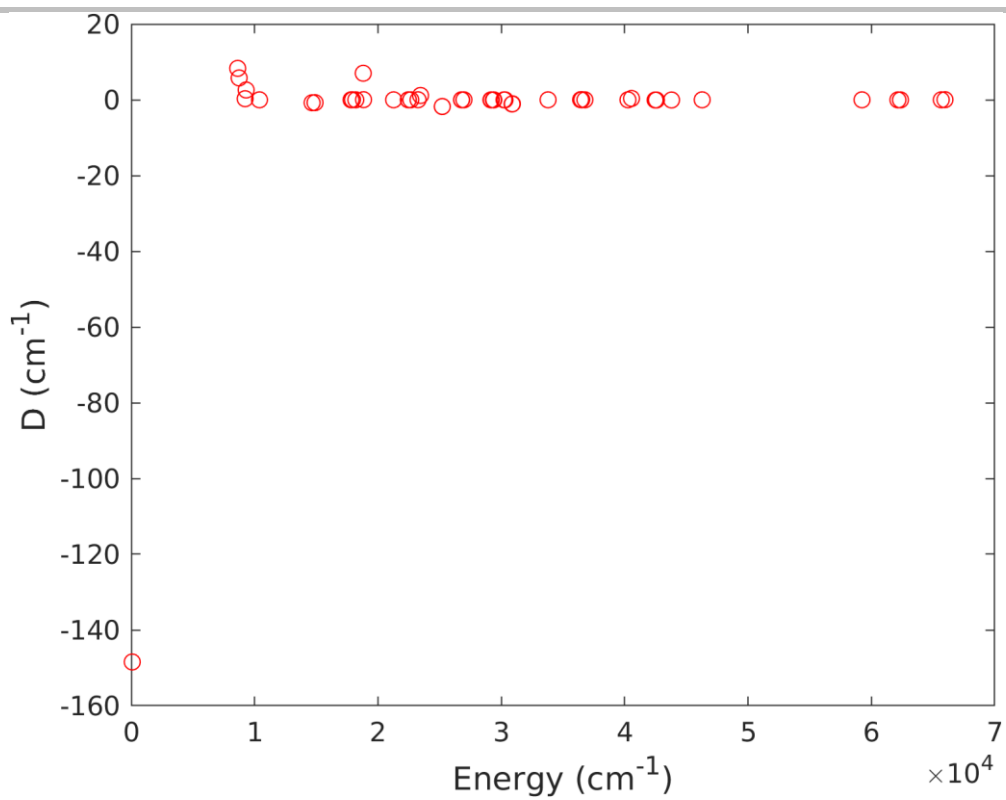
Figure S76. Contributions to *D* from various excited states for compound **1b**.

Figure S77. Contributions to *E* from various excited states for compound **1b**.

Figure S78. Contributions to *D* from various excited states for compound **1c**.

Figure S79. Contributions to *E* from various excited states for compound **1c**.

Figure S80. Contributions to *D* from various excited states for compound **1d**.
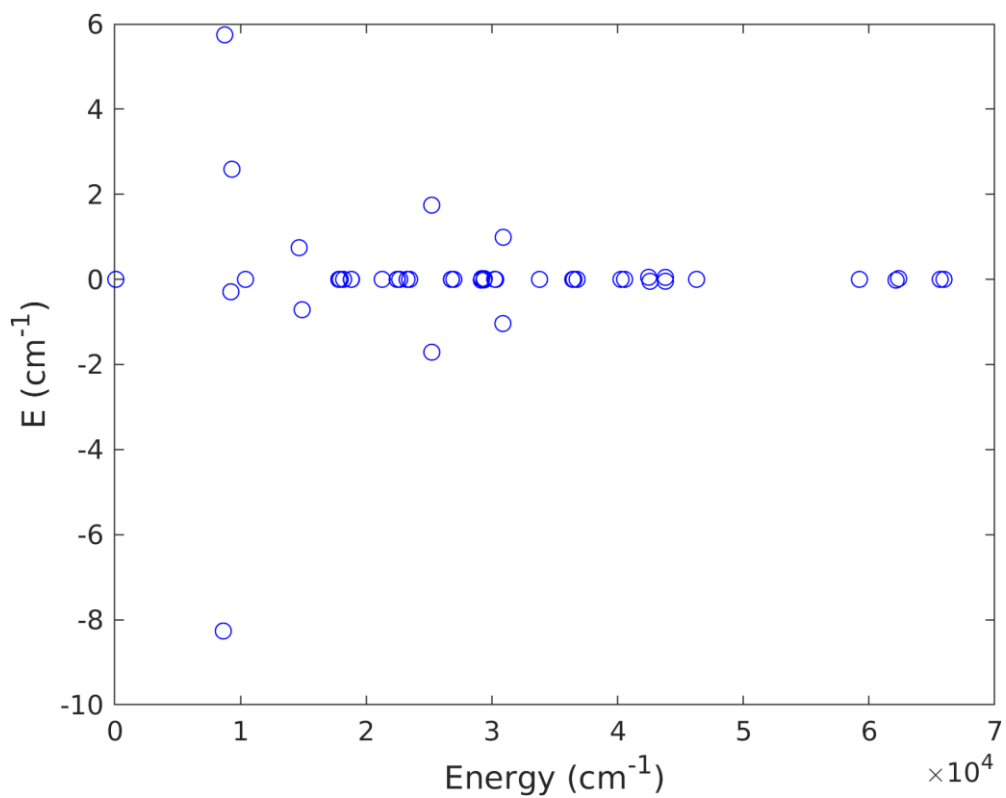

Figure S81. Contributions to *E* from various excited states for compound **1d**.

Figure S82. Contributions to *D* from various excited states for compound **2.**

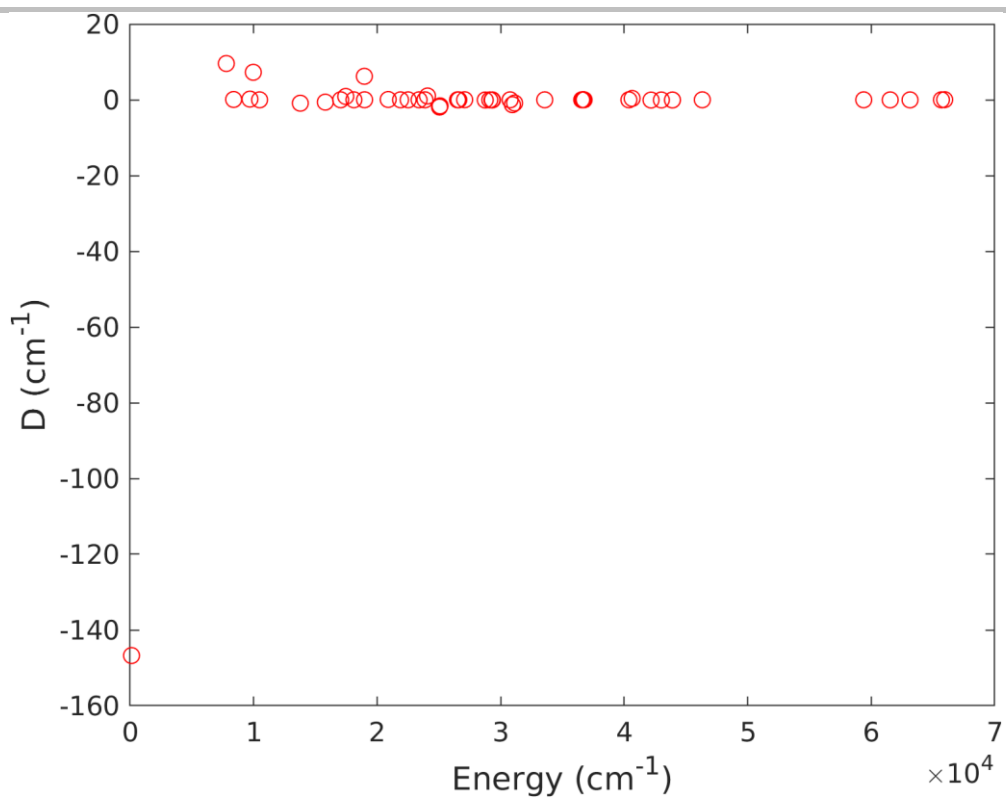**Figure S83**. Contributions to *E* from various excited states for compound **2.**

Figure S84. Contributions to *D* from various excited states for compound **3**.

Figure S85. Contributions to *E* from various excited states for compound **3**.
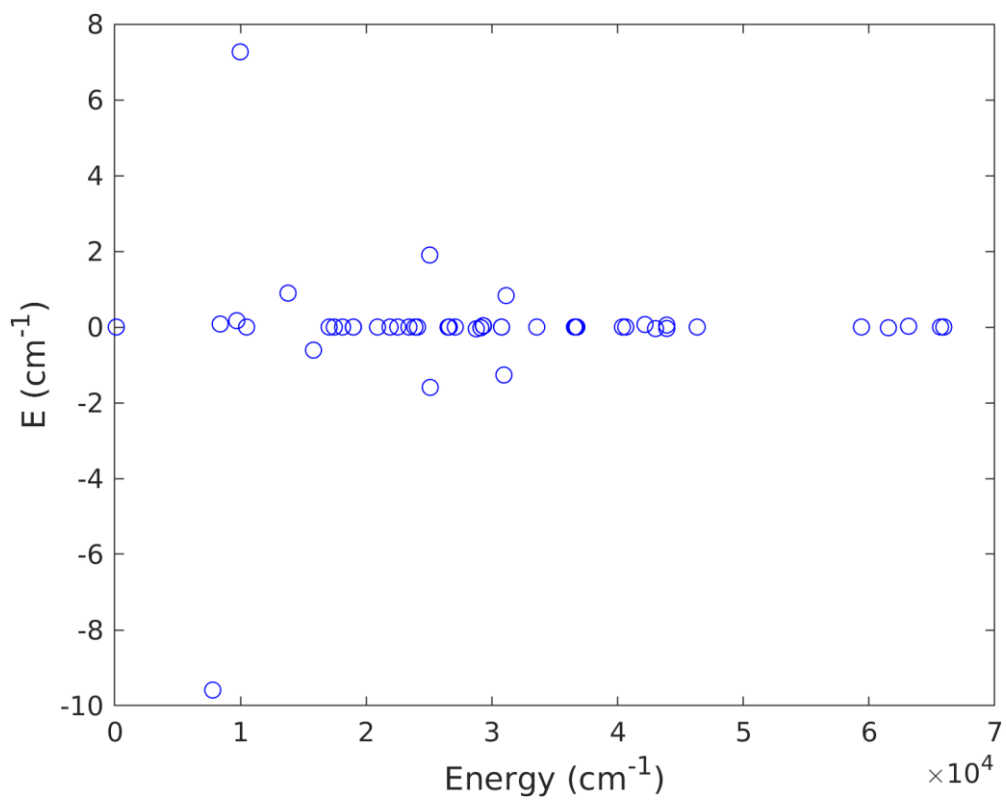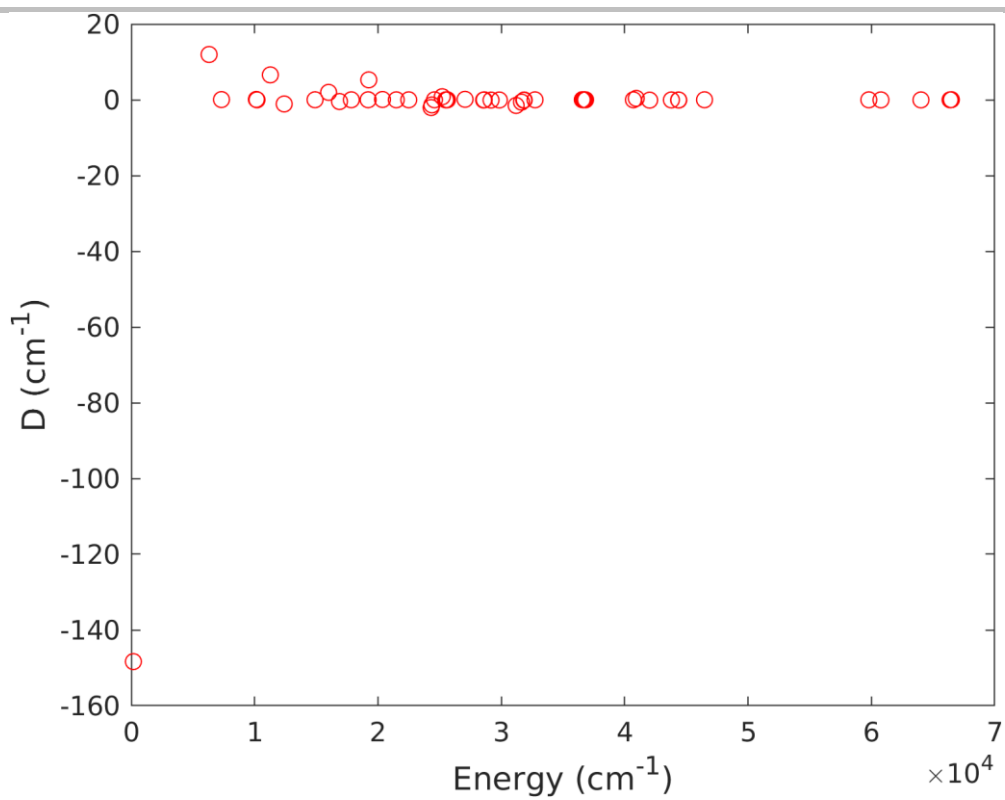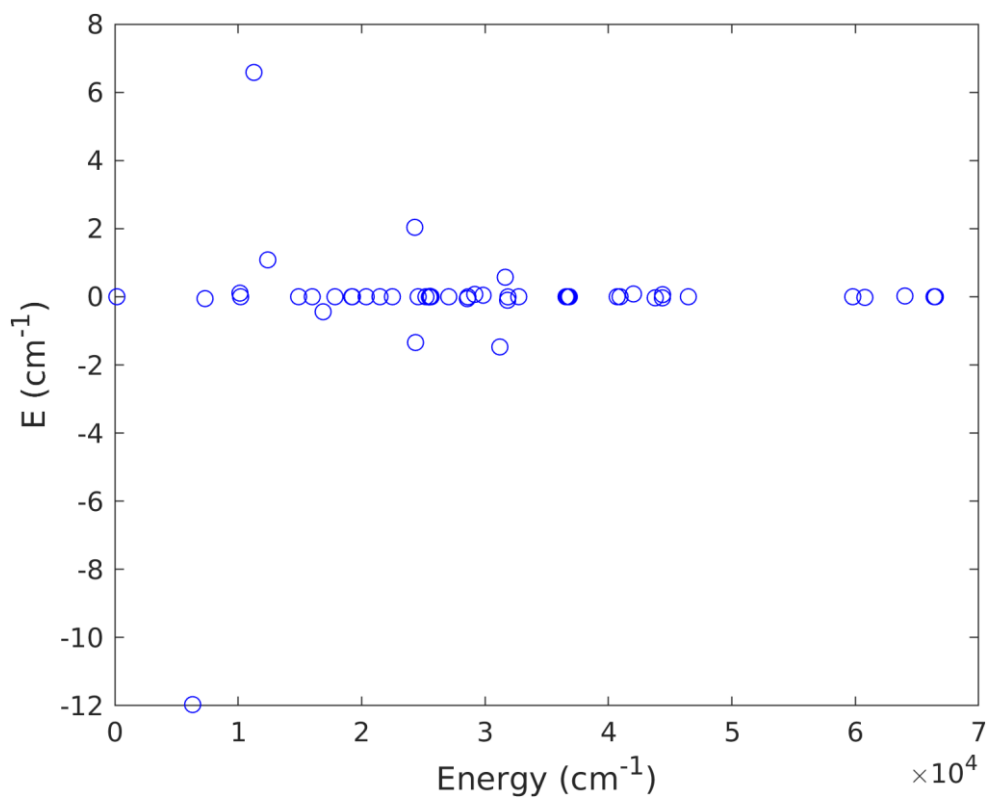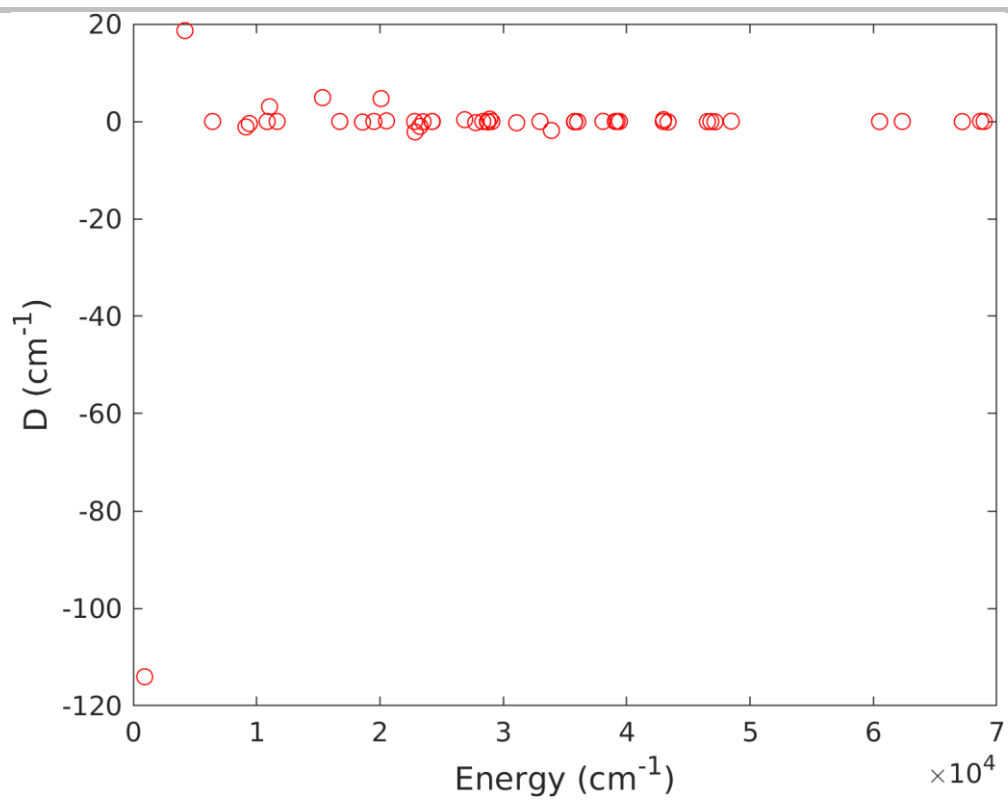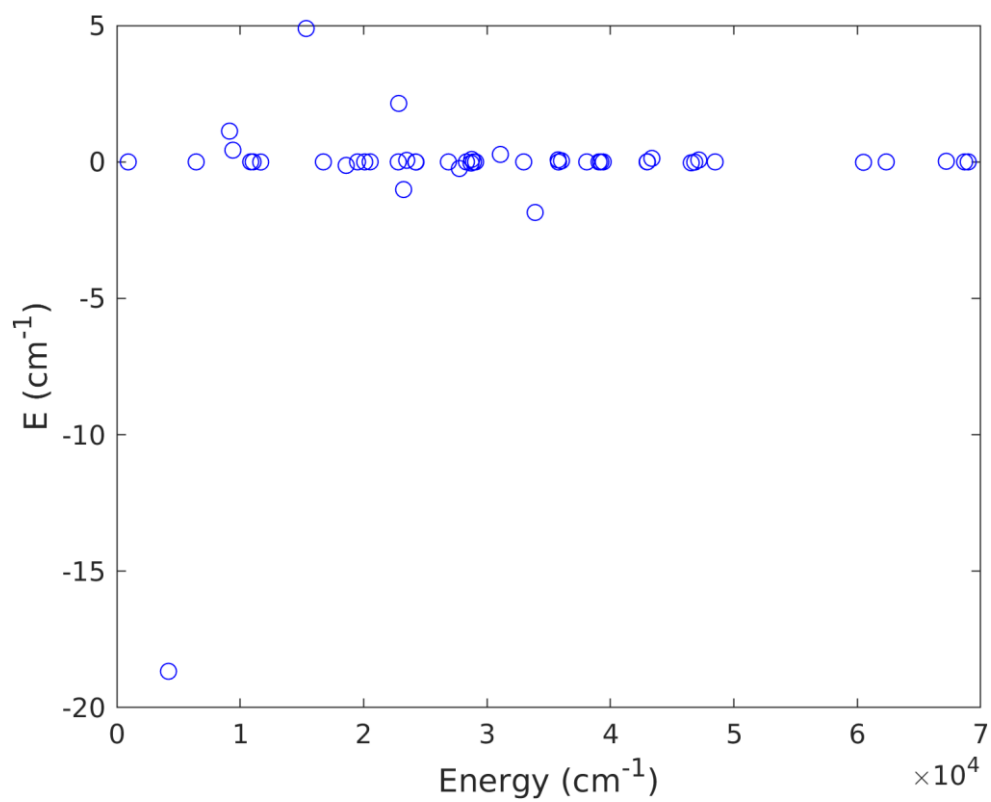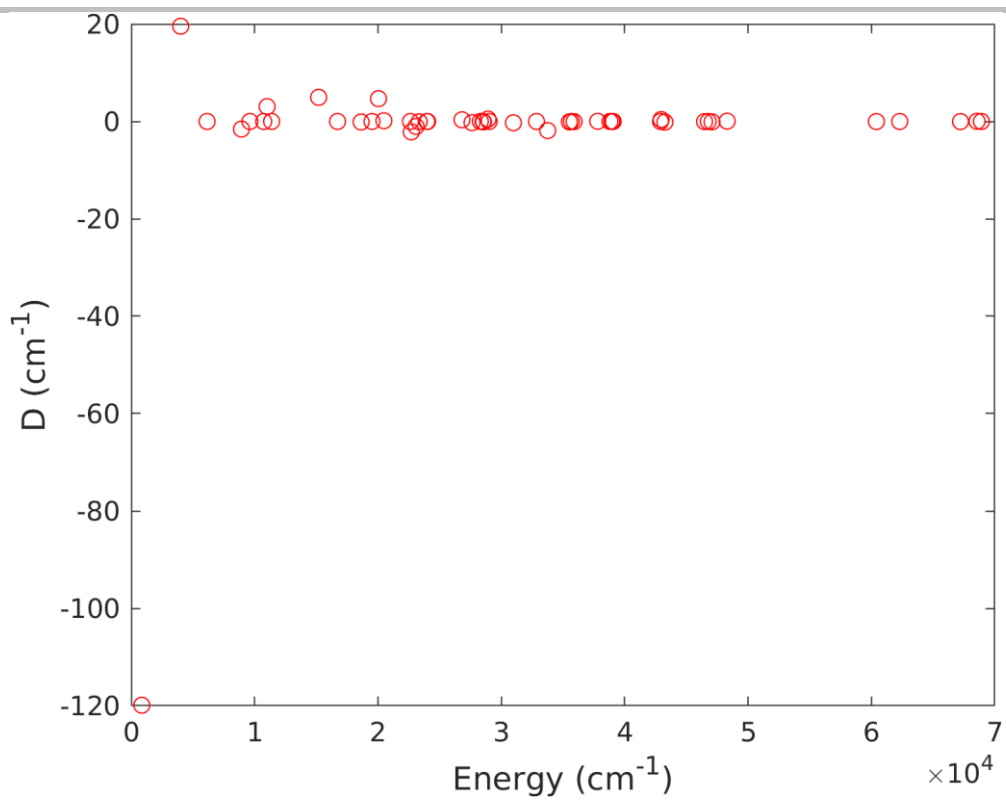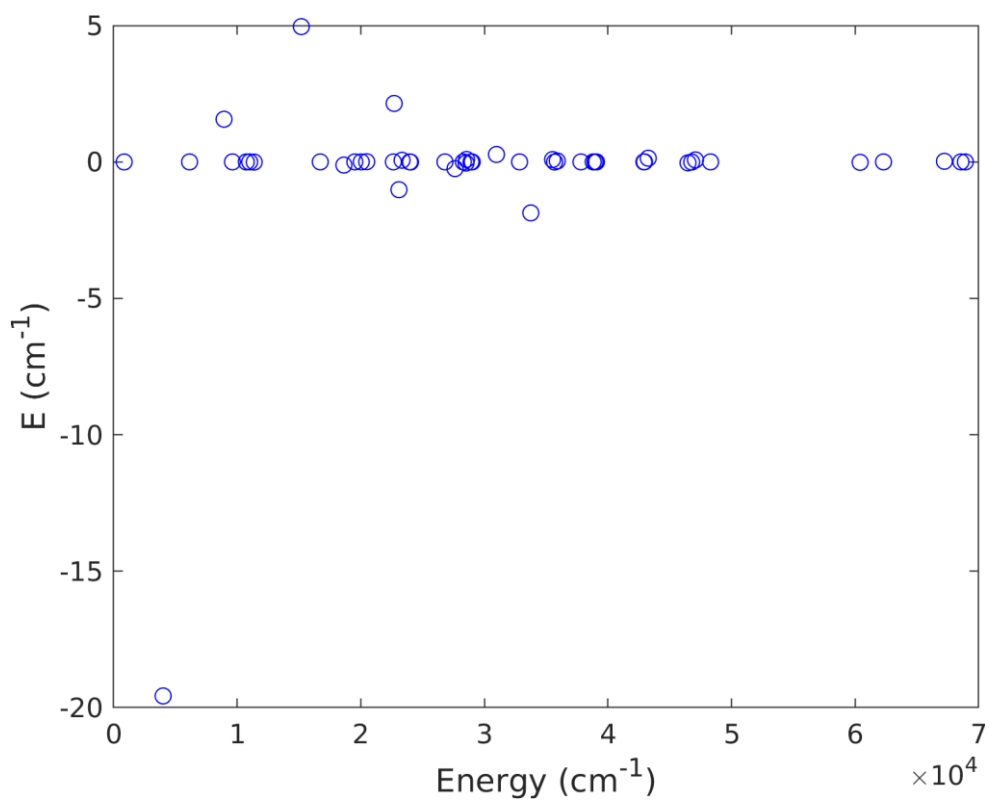
5.4 AOMX parametrization of the one-electron ligand-field Hamiltonian

$\langle d_{z^2}|V_{LF}|d_{z^2}\rangle = \left(\frac{1}{4}\right)e_\sigma\big(1 + (3\cos(2\theta))\big)^2$

$\langle d_{xz}|V_{LF}|d_{xz}\rangle = \left(-\frac{1}{2}\right)((\cos(\theta))^2)\Big((-4e_{\pi s}) - (6e_\sigma) + ((4e_{\pi s} - 6e_\sigma)\cos(\delta)) + (3e_\sigma\cos(\delta - (2\theta))) + (6e_\sigma\cos(2\theta)) + 3e_\sigma\cos(\delta + (2\theta))\Big)$

$\langle d_{yz}|V_{LF}|d_{yz}\rangle = \left(\frac{1}{2}\right)((\cos(\theta))^2)\Big((4e_{\pi s}) + (6e_\sigma) + ((4e_{\pi s} - 6e_\sigma)\cos(\delta)) + (3e_\sigma\cos(\delta - (2\theta))) - (6e_\sigma\cos(2\theta)) + 3e_\sigma\cos(\delta + (2\theta))\Big)$

$\langle d_{z^2}|V_{LF}|d_{x^2-y^2}\rangle = \left(\frac{\sqrt{3}}{2}\right)(e_\sigma)(\cos(\delta))\Big(1 + (3(\cos(2\theta)))\Big)((\sin(\theta))^2)$

$\langle d_{x^2-y^2}|V_{LF}|d_{x^2-y^2}\rangle = \left(-\frac{1}{8}\right)\Big((-16e_{\pi s}) + (-6e_\sigma) + (2(8e_{\pi s} - 3e_\sigma)\cos(2\delta)) + (3e_\sigma\cos(2(\delta - \theta))) + (6e_\sigma\cos(2\theta)) + (3e_\sigma\cos(2(\delta + \theta)))\Big)((\sin(\theta))^2)$

$\langle d_{xy}|V_{LF}|d_{xy}\rangle = \left(\frac{1}{8}\right)\Big((16e_{\pi s}) + (6e_\sigma) + (2(8e_{\pi s} - 3e_\sigma)\cos(2\delta)) + (3e_\sigma\cos(2(\delta - \theta))) + (-6e_\sigma\cos(2\theta)) + (3e_\sigma\cos(2(\delta + \theta)))\Big)((\sin(\theta))^2)$

**Table S8**: Ligand field 1-electron matrices used for extraction of AOM parameters for each complex.

| Complex	Orbital	d_{z^2}	d_{xz}	d_{yz}	$d_{x^2-y^2}$	d_{xy}
1a	d_{z^2}	-5.537384	-0.000052	0	-0.001739	0
	d_{xz}	-0.000052	-5.534939	0	0.00007	0
	d_{yz}	0	0	-5.504334	0	-0.000396
	$d_{x^2-y^2}$	-0.001739	0.00007	0	-5.539782	0
	d_{xy}	0	0	-0.000396	0	-5.506359
1b	d_{z^2}	-5.535687	-0.000089	0	-0.00068	0
	d_{xz}	-0.000089	-5.533645	0	-0.000046	0
	d_{yz}	0	0	-5.506125	0	-0.000084
	$d_{x^2-y^2}$	-0.00068	-0.000046	0	-5.536308	0
	d_{xy}	0	0	-0.000084	0	-5.50509
1c	d_{z^2}	-5.534399	0.000545	0	-0.001084	0
	d_{xz}	0.000545	-5.532092	0	0.000039	0
	d_{yz}	0	0	-5.508428	0	0.0013
	$d_{x^2-y^2}$	-0.001084	0.000039	0	-5.534537	0
	d_{xy}	0	0	0.0013	0	-5.499727
1d	d_{z^2}	-5.557921	0.000756	0	-0.001342	0
	d_{xz}	0.000756	-5.556528	0	-0.00001	0
	d_{yz}	0	0	-5.534772	0	0.004553
	$d_{x^2-y^2}$	-0.001342	-0.00001	0	-5.559284	0
	d_{xy}	0	0	0.004553	0	-5.517891
2a	d_{z^2}	-5.503361	-0.000495	0.009818	-0.019982	-0.013378
	d_{xz}	-0.000495	-5.54172	-0.003727	0.003708	-0.002542
	d_{yz}	0.009818	-0.003727	-5.532684	-0.011214	-0.002091
	$d_{x^2-y^2}$	-0.019982	0.003708	-0.011214	-5.525701	0.003211
	d_{xy}	-0.013378	-0.002542	-0.002091	0.003211	-5.533983
2b	d_{z^2}	-5.48251	0.000711	0.013714	-0.018841	-0.010364
	d_{xz}	0.000711	-5.527852	-0.001762	0.001233	-0.002304
	d_{yz}	0.013714	-0.001762	-5.514567	-0.011613	-0.000483
	$d_{x^2-y^2}$	-0.018841	0.001233	-0.011613	-5.514158	0.000461
	d_{xy}	-0.010364	-0.002304	-0.000483	0.000461	-5.518167
3	d_{z^2}	-5.549346	-0.008643	0	0.000028	0
	d_{xz}	-0.008643	-5.49333	0	0.0045	0
	d_{yz}	0	0	-5.546796	0	-0.000866
	$d_{x^2-y^2}$	0.000028	0.0045	0	-5.550629	0
	d_{xy}	0	0	-0.000866	0	-5.536528

5.5 Variation of D using Angular overlap parametrization
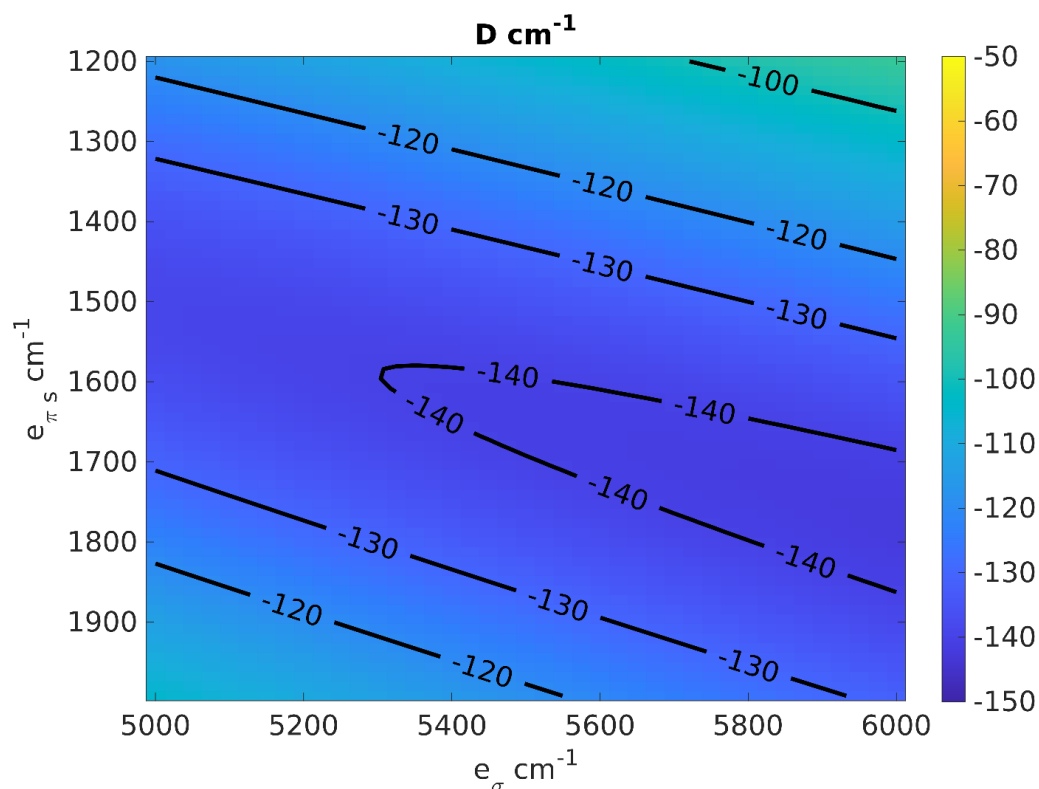
Figure S86. Variation of D as a function of e_σ and $e_{\pi s}$ for values of bite and dihedral angles at 82° and 90°.
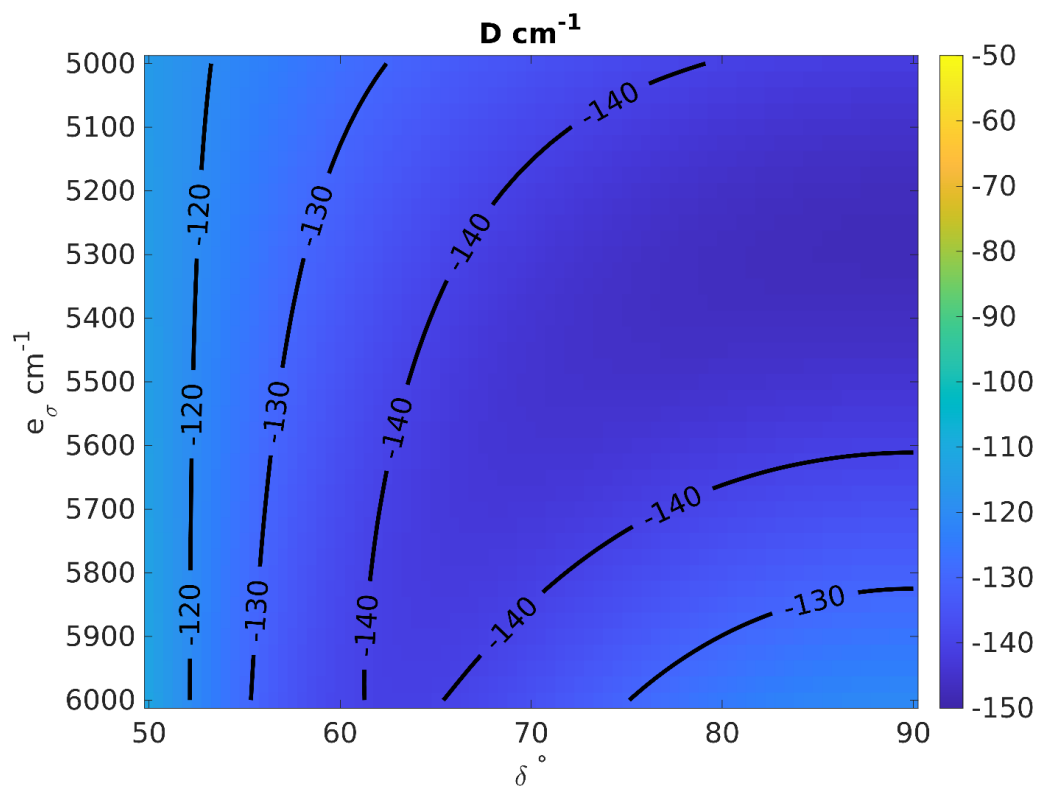

Figure S87. Variation of D as a function of e_σ and dihedral angle for values of bite angle of 82° and the average value of $e_{\pi s}$.

5.6 Orbital energy gaps
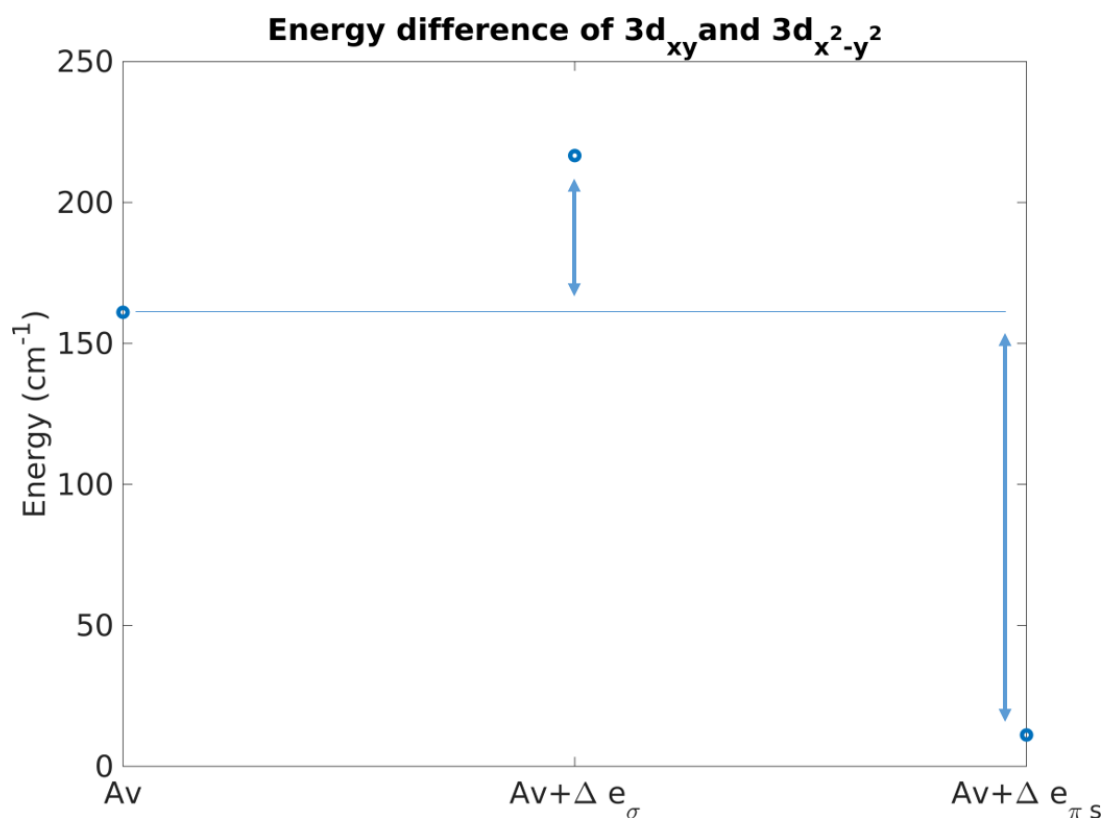
Figure S88. Energy gaps between the $3d_{xy}$ and $3d_{x2-y2}$ orbitals for different values of e_σ and $e_{\pi s}$ at values of bite and dihedral angles at 82° and 90°. Av= average $e_\sigma = 5556$ cm^{-1} and $e_{\pi s} = 1700$ cm^{-1}, $\Delta e_\sigma = 100$ cm^{-1}, $e_{\pi s} = 100$ cm^{-1}, (blue lines are a visual guide)
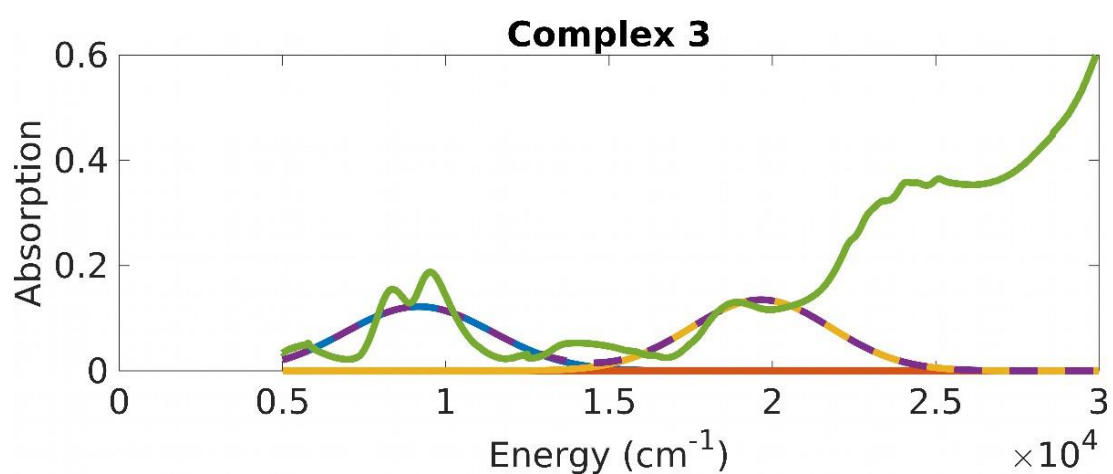
5.7 Gaussian deconvolution of the experimental absorption spectrum
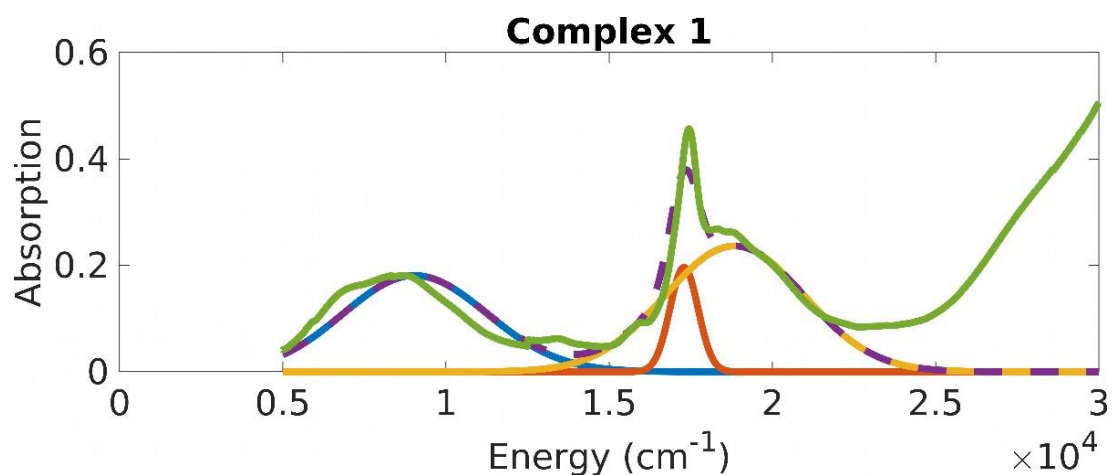
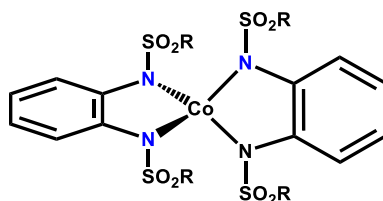**Figure S89**. Gaussian deconvolution of complex **1** according to Table 2.
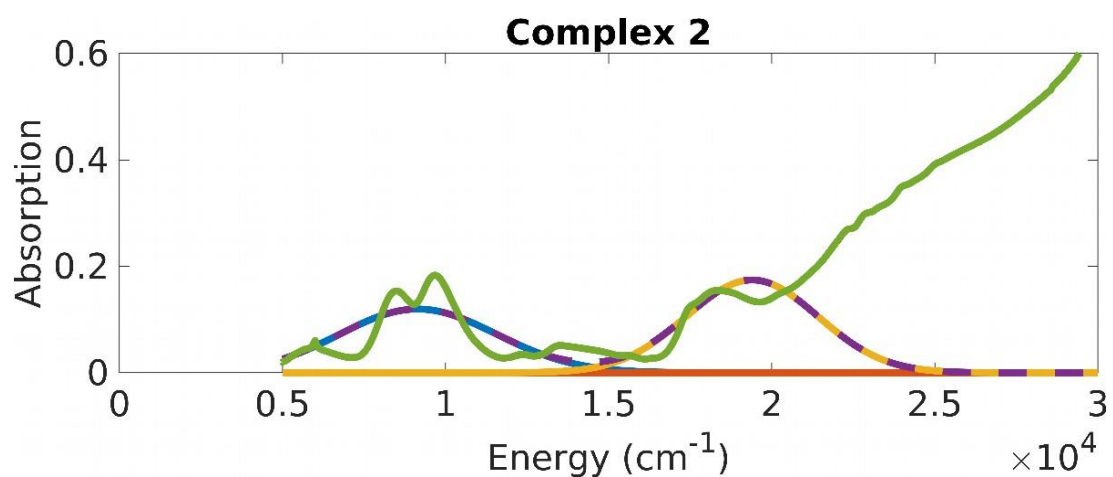
Figure S90. Gaussian deconvolution of complex **2** according to Table 2.

Figure S91. Gaussian deconvolution of complex **3** according to Table 2.

6. Viability of the Magneto-Structural Correlation

Table S9. Variation of D with the dihedral angle in Co(II) sulfonamido complexes


R = Me (bmsab); R = Tol (btsab)

Complex	δ (°)	N-Co-N bite angle (°)	D (cm^{-1})	E (cm^{-1})	Ref.
K$_2$[Co(bmsab)$_2$]	83.28	80.48, 80.96	−100	0	8
	87.30	80.35, 80.47			
(HNEt$_3$)$_2$[Co(btsab)$_2$]	84.03	80.19, 82.40	−110	0	8
(HNEt$_3$)$_2$[Co(bmsab)$_2$]	85.19	80.59, 80.70	−115	0	4a
(K-18-c-6)$_2$[Co(bmsab)$_2$]	86.62	80.74, 81.36	−130	0	8

δ = Dihedral angle between N-Co-N planes; bmsab = 1,2-bis(methanesulfonamido)benzene; btsab = 1,2-bis(toluenesulfonamido)benzene

Table S10. Variation of D with the dihedral angle in Co(II) sulfonamido complexes
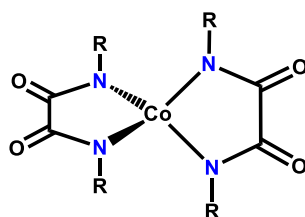
R = Ph (L^1); R = Tosyl (L^2); R = Mesyl (L^3)

Complex	δ (°)	N-Co-N bite angle (°)	D (cm^{-1})	E (cm^{-1})	Ref.
(Bu$_4$N)$_2$[Co(L^1)$_2$]·H$_2$O	87.49	83.36,84.78	-130.8 /-107.3	-0.07 / 4.01	9 / 10
(HNEt$_3$)$_2$[Co(L^2)$_2$]·H$_2$O	87.10	81.27,81.68	-144.1 /-125.2	0.02 / 0.62	9 / 10
(HNEt$_3$)$_2$[Co(L^3)$_2$]	89.32	81.08,81.65	-128.2	-0.65	10
	88.87	81.44,82.27			

δ = Dihedral angle between N-Co-N planes; H$_2$L^1 = N,N'-diphenyloxamide; H$_2$L^2 = N,N'-bis(p-toluenesulfonyl)oxamide; H$_2$L^3 = N,N'-bis(methanesulfonyl)oxamide

7. References

1. M. Llunell, D. Casanova, J. Cirera, J. Bofill, P. Alemany and S. Alvarez, *Universitat de Barcelona: Barcelona, Spain*, 2013.

2. E. Bill, *julX_2S*, Program for Simulation of Molecular Magnetic Data, Max-Planck Institute for Chemical Energy Conversion, Mülheim/Ruhr, Germany, **2014**.

3. D. Reta and N. F. Chilton, *PCCP*, 2019, **21**, 23567-23575.

4. a) Y. Rechkemmer, F. D. Breitgoff, M. van der Meer, M. Atanasov, M. Hakl, M. Orlita, P. Neugebauer, F. Neese, B. Sarkar and J. van Slageren, *Nat. Commun.*, 2016, **7**, 10467; b) S. K. Gupta, H. H. Nielsen, A. M. Thiel, E. A. Klahn, E. Feng, H. B. Cao, T. C. Hansen, E. Lelièvre-Berna, A. Gukasov, I. Kibalin, S. Dechert, S. Demeshko, J. Overgaard and F. Meyer, *JACS Au*, 2023, **3**, 429-440; c) V. V. Novikov, A. A. Pavlov, Y. V. Nelyubina, M.-E. Boulon, O. A. Varzatskii, Y. Z. Voloshin and R. E. P. Winpenny, *J. Am. Chem. Soc.*, 2015, **137**, 9792-9795; d) K. Chakarawet, P. C. Bunting and J. R. Long, *J. Am. Chem. Soc.*, 2018, **140**, 2058-2061.

5. a) G. Breit, *Phys. Rev.*, 1932, **39**, 616-624; b) G. Breit, *Phys. Rev.*, 1929, **34**, 553-573; c) G. Breit and L. A. Wills, *Phys. Rev.*, 1933, **44**, 470-490.

6. D. Ganyushin and F. Neese, *J. Chem. Phys.*, 2013, **138**, 104113.

7. M. Atanasov, D. Ganyushin, D. A. Pantazis, K. Sivalingam and F. Neese, *Inorg. Chem.*, 2011, **50**, 7460-7477.

8. H. Bamberger, U. Albold, J. Dubnická Midlíková, C.-Y. Su, N. Deibel, D. Hunger, P. P. Hallmen, P. Neugebauer, J. Beerhues, S. Demeshko, F. Meyer, B. Sarkar and J. van Slageren, *Inorg. Chem.*, 2021, **60**, 2953-2963.

9. H.-H. Cui, F. Lu, X.-T. Chen, Y.-Q. Zhang, W. Tong and Z.-L. Xue, *Inorg. Chem.*, 2019, **58**, 12555-12564.

10. M. Wang, H. J. Xu, T. M. Sun, H. H. Cui, Y.-Q. Zhang, L. Chen and Y. F. Tang, *J. Solid State Chem.*, 2021, **299**, 122209.